Palaeogeography, Palaeoclimatology, Palaeoecology 695 (2026) 113829

Contents lists available at ScienceDirect

Palaeogeography, Palaeoclimatology, Palaeoecology

journal homepage: www.elsevier.com/locate/palaeo

New insights into the paleoecology of brachiopod-arthropod-microbial assemblages from Upper Triassic cryptic submarine cavities☆

Iuliana Lazăr [a,b,*], Constantin Balica [c], Mihaela Grădinaru [a], Michael R. Sandy [d,e], Tea Kolar-Jurkovšek [f], Eugen Grădinaru [a,1], Mihai N. Ducea [a,b], Marie-Béatrice Forel [g]

[a] University of Bucharest, Department of Geology Mineralogy and Paleontology, Faculty of Geology and Geophysics, 1 N. Balcescu Ave., RO-010041 Bucharest, Romania
[b] Research Institute of the University of Bucharest, 90-92, Panduri Road, 5th District, Bucharest, Romania
[c] Babeș-Bolyai University, Faculty of Biology and Geology, Department of Geology, 1, M. Kogalniceanu Ave, Cluj-Napoca, Romania
[d] Department of Geology, University of Dayton, 300 College Park, Dayton, OH 45469-2364, USA
[e] Education and Research - Bulgaria, ul. Strandja 8, Rakovski 4150, Bulgaria
[f] Geological Survey of Slovenia, Dimičeva ulica 14, 1000 Ljubljana, Slovenia
[g] CR2P UMR7207, Muséum national d'Histoire naturelle, 8 rue Buffon, 75005 Paris, France

ARTICLE INFO

Editor: L Angiolini

Keywords:
Halorella
Frutexites
Neptunian dike and sill
Upper Triassic
Romania

ABSTRACT

A unique record of an Upper Triassic brachiopod (*Halorella*)-arthropod (*Halorina* microcoprolites)-microbial (*Frutexites*) assemblage is documented from iron-rich carbonates filling a neptunian dike and sill system developed in Carnian-lower Rhaetian limestone host rock from Leurdeasa Hill in the Apuseni Mountains, Romania. The host rock at Leurdeasa Hill through which the dike and sill cross-cut is dated as early Carnian by the conodont assemblage. The paleoecology of this brachiopod-arthropod-microbial assemblage along with the paleoenvironmental context and genesis of iron-rich carbonates filling the Upper Triassic neptunian dike and sill system is examined through integrated analyses including paleontology, taphonomy, microfacies, mineralogy and stable isotopes of carbon and oxygen, as well as patterns of rare-earth elements. *Frutexites* microstructures and their possible microbial origin are documented for the first time in an upper Norian-lower Rhaetian neptunian dike and sill. Given the broad paleogeographic distribution of the brachiopod *Halorella* during the Late Triassic and the scarcity of marine paleoenvironments from where this genus has been reported, we conclude that the proliferation of significant populations of *Halorella* alongside with arthropods and microbial consortia were restricted to submarine cryptic paleoenvironments characterized by peculiar conditions, namely, warm waters, temporarily rich in nutrients, in dark habitats. Geochemical data show that the red carbonate infills are predominantly seawater-derived with minor terrigenous input, later modified by Fe-Mn oxide formation, organic matter cycling, and diagenesis, and record short-term apparent cyclic shifts between oxic and suboxic conditions in a semi-restricted neptunian dike/sill system likely linked to episodic biotic blooms and variable water exchange.

1. Introduction

The Mesozoic fossil record of the sedimentary filling of submarine cavities or fissures such as neptunian dikes and sills that impact carbonate successions is well-documented, especially from the Alpine-Mediterranean region since the early 1880's (Walther, 1885; Fischer, 1964; Wendt, 2017; Flügel, 2010). The filling of these submarine fissures or fractures can occur in various depositional environments and may be influenced by different sedimentary processes occurring in shallow and deep marine settings (Flügel, 2010). Therefore, the associated fossil assemblages may include both allochthonous and autochthonous biota. The autochthonous biota of the submarine cavities such as neptunian

☆ This article is part of a Special issue entitled: 'Brachiopods' published in Palaeogeography, Palaeoclimatology, Palaeoecology.

* Corresponding author at: University of Bucharest, Department of Geology Mineralogy and Paleontology, Faculty of Geology and Geophysics, 1 N. Balcescu Ave., RO-010041 Bucharest, Romania.
E-mail addresses: iuliana.lazar@g.unibuc.ro (I. Lazăr), constantin.balica@ubbcluj.ro (C. Balica), mihaela.gradinaru@unibuc.ro (M. Grădinaru), msandy1@udayton.edu (M.R. Sandy), tea.kolar-jurkovsek@geo-zs.si (T. Kolar-Jurkovšek), mihai.ducea@g.unibuc.ro (M.N. Ducea), marie-beatrice.forel@mnhn.fr (M.-B. Forel).

[1] The author Eugen Grădinaru passed away on 16th of January 2025.

https://doi.org/10.1016/j.palaeo.2026.113829
Received 4 August 2025; Received in revised form 15 April 2026; Accepted 22 April 2026
Available online 28 April 2026

dikes and sills, included microbial consortia as well as benthic foraminifera, ostracods, serpulids and brachiopods, organisms that formerly lived at the edges of or within them (Gonzalez-Donoso et al., 1983; Playford et al., 1984). In contrast, the allochthonous biota are usually represented by ammonoids, pelagic bivalves; however, benthic organisms could also be gently swept by currents into the neptunian dikes and sills or could be deposited rapidly during storm events. To gain a better understanding of the paleoenvironmental context and paleoecology of such specific fossil assemblages as well as to date the infilling of neptunian dikes and sills, detailed sedimentological, geochemical, taxonomical and taphonomical analyses are essential. Wendt (2017) suggested that neptunian dikes are generally filled through single rapid sedimentary events, which rarely capture enough fossil remains for a precise dating of the infill. According to the same author, a more comprehensive biostratigraphic history can be revealed from neptunian sills, where shells accumulated in conditions devoid of currents and reworking, leading to a very good degree of preservation. Therefore, neptunian sills infill may represent a short time-span or in the case of condensed sedimentation and/or omission, they may contain a unique stratigraphic record that is missing in the normal sequence developed elsewhere.

Upper Triassic shallow-water carbonates are extensively distributed along the Neo-Tethys margins and are known from the Alps, Carpathians, Dinarids, Greece, Turkey, Oman, to the Indonesian Islands (Flügel and Senowbari-Daryan, 1996; Flügel et al., 1996; Krystyn et al., 2009; Kovács et al., 2011; Gawlick and Missoni, 2021). A conspicuous feature of these carbonates is the presence of an irregular network of cavities and fractures, typically filled with red sediments. In some cases, these are represented by neptunian dikes and sills filled with ferruginous carbonates; a few of these occurrences include Upper Triassic brachiopods, such as *Halorella* Bittner, 1884. Several such occurrences were first mentioned from the Alps (e.g., Walther, 1885; Fischer, 1964).

The origin of the neptunian dikes affecting these carbonates may be attributed to tectonic activity (fracturing) or erosional processes (karstic solution weathering in limestone country rock), or a combination of both. These newly opened sites provided a milieu that was conducive for brachiopod colonization of the walls of the neptunian dikes and sills, leading to subsequent washing and deposition of brachiopods into these cavities. Ager (1965) posited that the brachiopods *Halorella* and *Halorelloidea* Ager, 1960 in great abundance in neptunian dikes from the Upper Triassic of the Swiss Alps (described by Fischer, 1964) were washed into these fractures, having been transported from sublittoral non-depositional sea floors. Conversely, Kiel et al. (2021) interpreted the same occurrences of *Halorella* as parautochthonous assemblages primarily consisting of brachiopods that lived under normal-marine conditions in the neptunian dikes and fissures. Grădinaru, as referenced in Kovács et al. (2011), noted a widespread development of "*karstification*" into the upper Carnian-Norian reefal limestones in the vicinity of Vaşcău, Apuseni Mountains, Romania. Later, Lazăr et al. (2017) suggested that these "*karstified*" limestones were subsequently flooded by a marine transgression during which *Halorella* brachiopods likely were the early colonizers of the sea-floor including the dikes, sills and palaeokarst cavities. Müller et al. (2026) report mass occurrence of *Halorella amphitoma* (Bronn, 1832) from a peculiar habitat represented by a karstic cavity developed in the supratidal zone of the Dachstein platform (Bakony Mountains, Hungary) flooded by marine ingressions.

In-depth multidisciplinary analyses performed by the authors of the current study on the Leurdeasa Hill section containing *Halorella* from the Northern Apuseni Mountains have yielded new insights into the genesis, paleoecology and paleoenvironmental context of these rare brachiopod assemblages. Despite several studies highlighting the disjunct paleogeographic distribution of the brachiopod *Halorella* and mass-occurrences in fissures, neptunian dikes or palaeokarst cavities in the Upper Triassic carbonates of the Northern Calcareous Alps in Austria and Bakony Moutains in Hungary, the paleoecology of these occurrences remains largely elusive (Kiel et al., 2021).

This contribution aims to: (a) report a unique record of an Upper Triassic assemblage comprising brachiopod (*Halorella*)-arthropod (*Halorina* microcoprolites)-microbial (*Frutexites*) elements found in iron-rich carbonates that fill a neptunian dike/sill system developed in Carnian-Norian carbonates exposed on the NW slope of Leurdeasa Hill, near Vaşcău, Apuseni Mountains, Romania; the stratigraphy of the section is well documented, supported by detailed study of the conodont assemblage; (b) discuss in detail the paleoenvironmental context, the origin of iron-rich carbonates containing an assemblage of super-abundant brachiopods (*Halorella*), arthropods (crustacean decapod microcoprolites and ostracods) and microbial (*Frutexites*) elements in this neptunian dike/sill system and their paleoecology. The discussion will be informed by integrated analyses of microfacies, diagenesis, paleontology, taphonomy, geochemistry (oxygen and carbon stable isotopes and trace element patterns) and mineralogy. The paleogeographic distribution of notable mass-occurrence of *Halorella* during the Late Triassic is also discussed.

2. Geological setting and stratigraphy

The studied Upper Triassic succession is located on the NW slope of Leurdeasa Hill in the Vaşcău Plateau, part of the Codru Nappe System (Codru-Moma Mountains, Fig. 1A), within the Northern Apuseni domain (Bleahu, 1976a, 1976b; Bleahu et al., 1979, 1981; Patrulius et al., 1979; Panin et al., 1980). These units have been classified as the Inner Dacides by Săndulescu (1984). On a larger, regional scale, the Northern Apuseni domain belongs to the Tisza Megaunit, which was located at the northern Tethyan shelf margin, east of the dry lands of the Bohemian Massif and Vindelician High during the Triassic period (Bleahu et al., 1994; Kovács et al., 2011). The Vaşcău Plateau is considered one of the most representative areas within the Northern Apuseni Mountains due to the extensive and complete occurrences of Triassic carbonate successions (Patrulius and Bleahu, 1967; Bleahu et al., 1970, 1972; Panin and Tomescu, 1974; Patrulius, 1976a; Patrulius et al., 1971, 1979; Patrulius, 1976b in Ianovici et al. (1976). According to Bleahu et al. (1979) and Panin et al. (1980), three nappes have been identified and mapped in the Vaşcău Plateau (Fig. 1B-E): the Moma Nappe in the lowest position, the Vaşcău Nappe and the Coleşti Nappe, in the highest position. The carbonate succession from the Coleşti Nappe (Fig. 1E) consists of reefal and reef-slope facies typical for the Wetterstein-type limestone (lower Carnian) and Dachstein-type limestone (upper Carnian-Rhaetian), indicative of shallow-water carbonate platforms that developed during the Late Triassic in this area (Panin and Tomescu, 1974; Patrulius et al., 1979; Bleahu et al., 1979; Panin et al., 1980). Locally these limestones exhibit a dense irregular network of fractures and cavities filled with red carbonate sediments. One of the most representative sections (Figs. 2, 3) that also contains an abundant *Halorella* brachiopod assemblage is located on the western side of a forest road leading to the Leurdeasa Hill area (Fig. 1B, GPS N46°27′15.75″; E22°25′12.12″; 672 m altitude). The carbonates from the Vaşcău Plateau (Coleşti Nappe) were part of an extensive carbonate platform system located at the European margin of the Western Neo-Tethys (Haas et al., 1995; Kovács et al., 2011). The carbonate succession from the Coleşti Nappe displays a high abundance of corals, crinoids, gastropods, brachiopods, bivalves, and cephalopods which have been documented in numerous studies (e.g. Kutassy, 1928, 1937; Bleahu et al., 1970, 1972; Panin and Tomescu, 1974). The deepest water settings of this carbonate platform are represented by cherty black limestones of the Roşia Formation in the Coleşti and Vaşcău Nappe (Fig. 1D, E) and by crinoidal or halobiid-bearing grey-pink limestones of the Izbuc Formation in the Moma Nappe (Fig. 1C). The Dachstein-type limestones from the Coleşti Nappe are capped by upper Rhaetian lagoonal facies that contain loferitic cycles (Panin and Tomescu, 1974; Patrulius et al., 1979; Baltres, 1998; Bucur and Săsăran, 2001). Furthermore, the topmost part of these carbonates is unconformably overlain by red silty-limestones and clays containing belemnites and the foraminifera *Involutina liassica* (Jones *in*

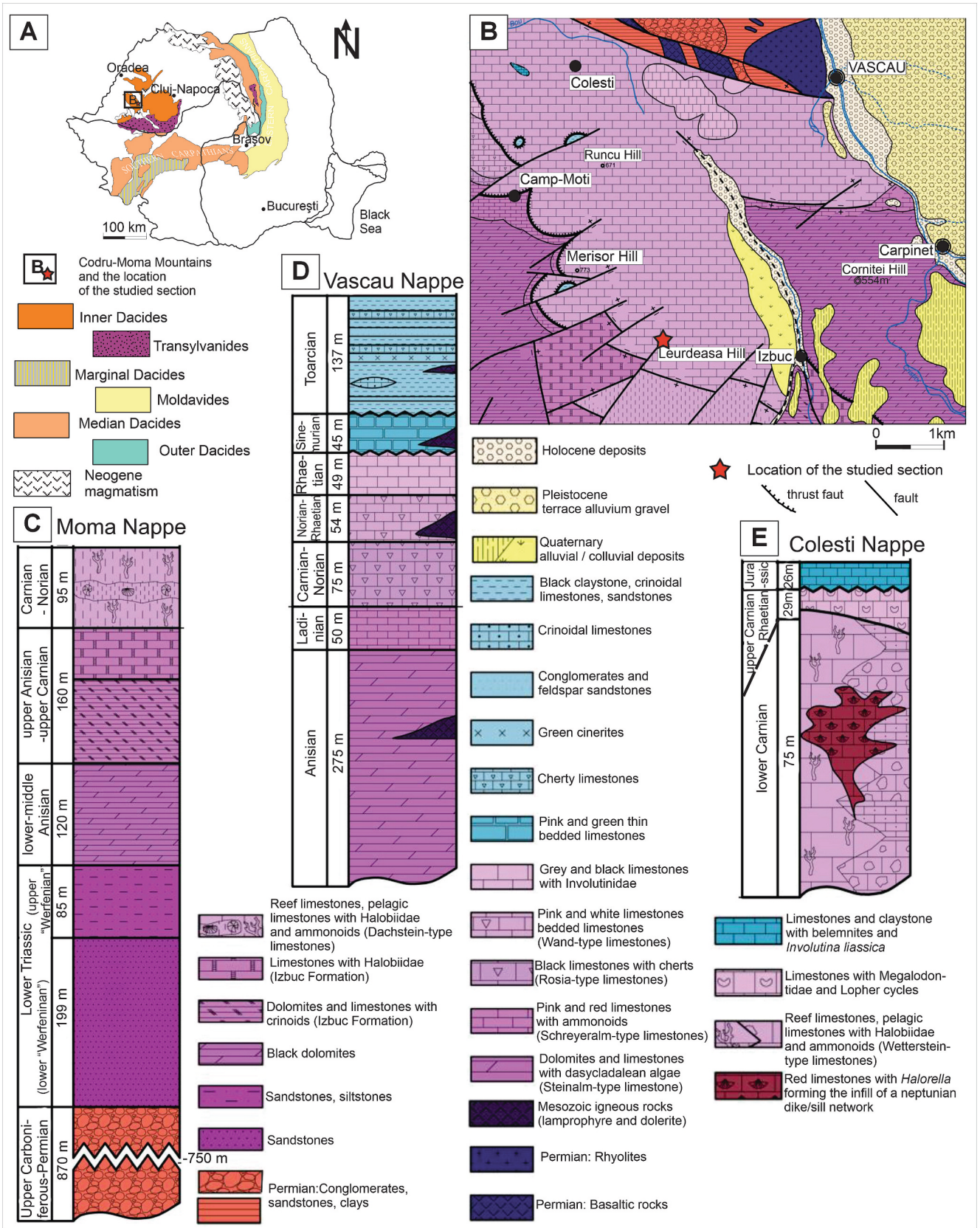

Fig. 1. (A) Location of the Codru-Moma Mountains within the Northern Apuseni Mountains, Romania (based on the geotectonic map of Romania, 1:1000000, Săndulescu, 1984). (B) Geological map showing the location of the studied section on the north-western slope of the Leurdeasa Hill (based on the geological outline map, 1:50000 of the Coleşti-Vaşcău area, Bleahu et al., 1979). The legend for the geological map corresponds to the legend of the lithostratigraphic columns. Lithostratigraphic columns: (C) Moma Nappe, (D) Vaşcău Nappe, (E) Coleşti Nappe.

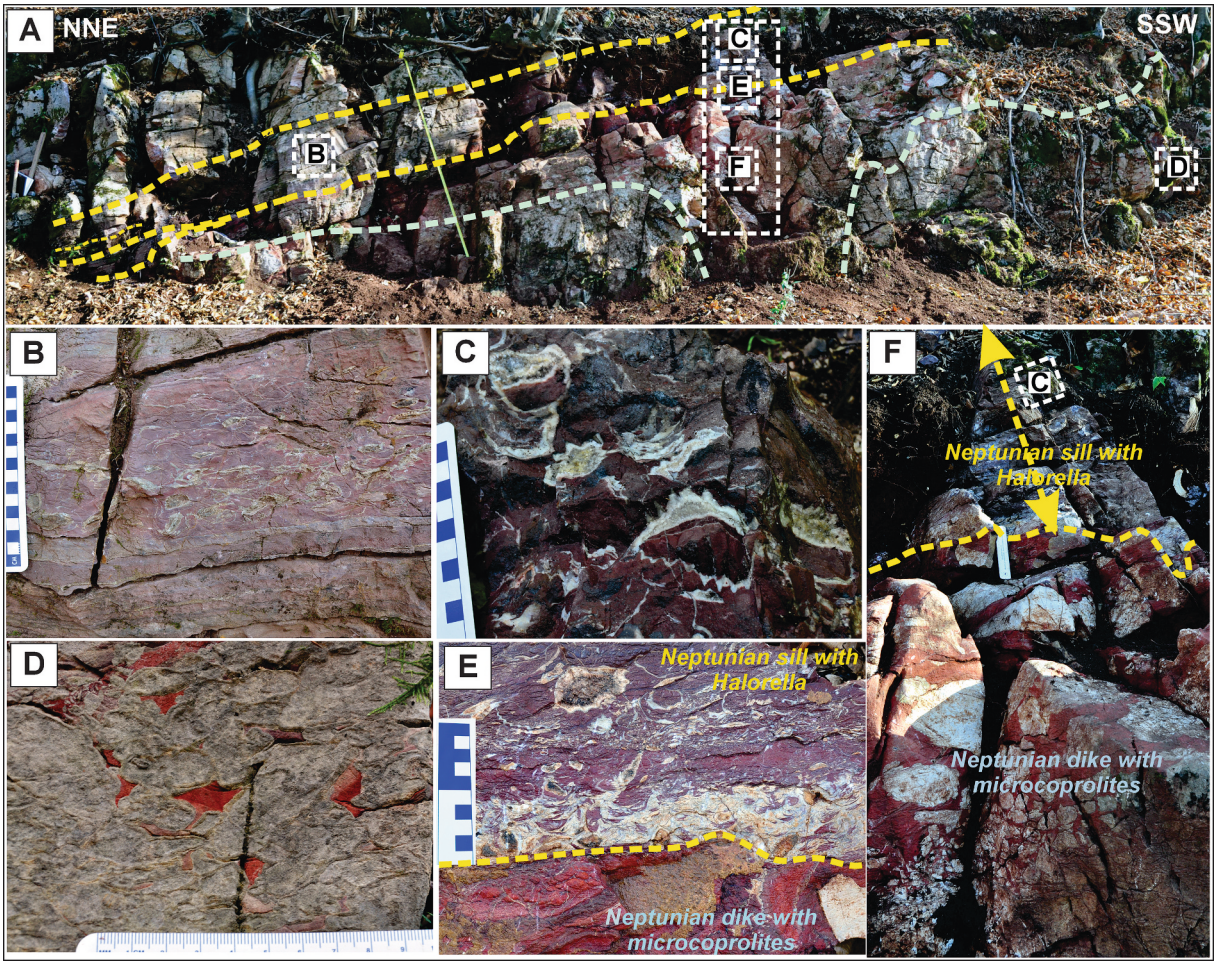

Fig. 2. (A) The outcrop of the Upper Triassic bedded limestones affected by a neptunian dike (grey dotted lines) and sill (yellow dotted lines) system. The neptunian sill is developed approximately parallel with the stratification of the host limestones. The yellow ruler disposed perpendicular to the stratification is 2 m long. (B, C) Details of the neptunian sill filled with dark red to mauve carbonates containing *Halorella* shells. (D) At the base of the section the host limestone contains cavities and fissures filled with red carbonates. (E, F) Details of the contact (yellow dotted line) between the carbonates infilling of a dike and sill. (For interpretation of the references to colour in this figure legend, the reader is referred to the web version of this article.)

Brodie, 1853) (Panin et al., 1974; Bleahu et al., 1979).

3. Materials and methods

3.1. Materials

3.1.1. Polished surfaces and thin sections

A total of 70 rock-samples were collected from the Leurdeasa Hill section, situated nearly six kilometres southeast of the village of Câmp-Moţi. From these, 30 rock samples were selected for thin sections (6 × 6 cm) and polished slabs that were further examined under petrographic and binocular microscopes. The thin sections are stored in the Laboratory of Paleontology of the University of Bucharest (Iuliana Lazăr collection). The classification of carbonate textures is based on the system established by Dunham (1962), with subsequent modifications introduced by Embry and Klovan (1971).

3.1.2. Brachiopods

Through careful specimen preparation, we obtained good representations of the external morphology of the brachiopods from Leurdeasa Hill. The sedimentary matrix was typically well-indurated, making the collection and preparation of isolated specimens quite challenging. However, over 35 brachiopod specimens (LPB IIIb 801–837) were prepared using an air scribe and small chisels, also enabling us to observe their internal morphological characters in transverse serial sections through several specimens. The brachiopod specimens are also stored within the Laboratory of Paleontology Collection, Geology Department of the University of Bucharest (LPB).

3.1.3. Conodonts

Seven samples for conodont study were provided by Eugen Grădinaru in 2018 and 2020 of which two are devoid of conodonts (Table 1). The processing of carbonate samples was carried out at the University of Bucharest utilizing a standard preparation technique with diluted acetic acid. The weight of the dissolved rock samples ranged between 2.0 and 0.8 kg, except for one sample (number 2310) which weighed 7.5 kg. The microfauna including conodonts was hand-picked from the residues at the Geological Survey of Slovenia where they are currently stored. The illustrated conodont elements were photographed using a JEOL JSM 6490LV Scanning Electron Microscope at the Geological Survey of Slovenia. The preservation of the examined conodonts is relatively good considering their geologic history. From two samples (2310 and 2559) abundant conodont material was recovered, however only few specimens enabled identification due to deformation or incomplete preservation; species of *Paragondolella* and *Quadralella* are abundant, whereas *Budurovignathus, Kraussodontus* and *Neocavitella* are rare, with determination of 1–2 specimens. Samples 2309, 2557 and 2560 contained only few identifiable conodont elements. The samples 2550 and 2552 were proven to be barren of conodonts. Moreover, the surface of the specimens is corroded, evident in certain specimens. According to Harris et al.

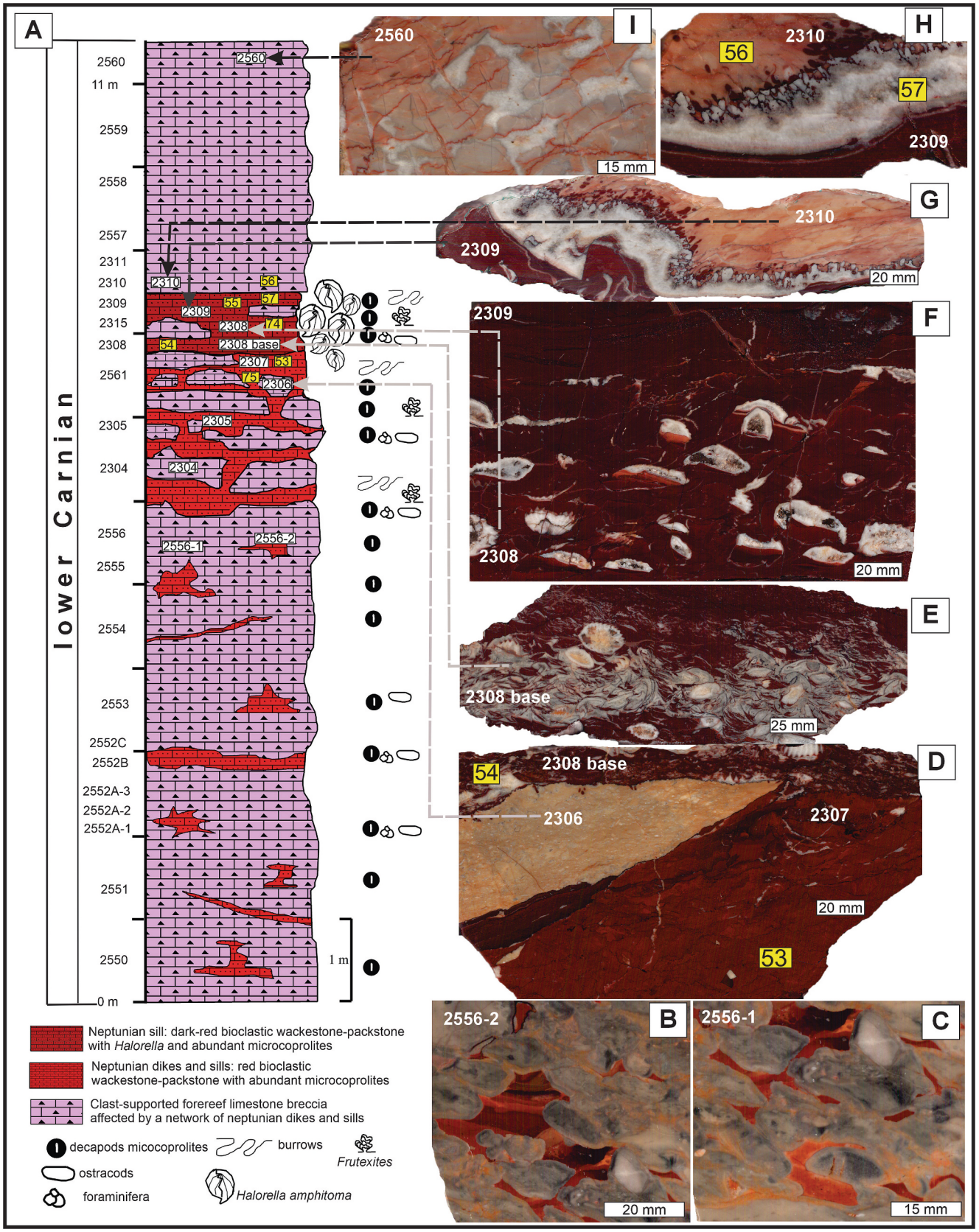

Fig. 3. (A) Lithostratigraphic column of the studied section. (B-I) polished surfaces: (B, C) The host limestones affected by fractures and cavities filled with successive influxes of red carbonates. (D) Contact between the red carbonates of the neptunian dike and the mauve carbonates of the neptunian sill and a large clast from the walls of the host limestone. (E, F) The neptunian sill contains bioclastic packstone (in the base) to floatstone (in the centre and upper part) along with abundant *Halorella* shells. (G, H) Contact between the mauve carbonates with *Halorella* and the host limestone. (I) Host limestones with cavities filled with carbonate cements. (For interpretation of the references to colour in this figure legend, the reader is referred to the web version of this article.)

Table 1
List of identified conodont microfossils.

Sample	Microfauna
2310	*Budurovignthus mungoensis* (Diebel)
Host limestone above the	*Budurovignathus* sp.
neptunian sill	*Kraussodontus* aff. *praeangustus* (Kozur, Mirăuță & Mock)
	Neocavitella tatrica (Zawidzka)
	Paragondolella praelindae Kozur
	Paragondolella sp.
	Quadralella polygnathiformis (Budurov & Stefanov)
	Quadralella cf. *acuminata* (Orchard)
	Quadralella sp.
2309	*Quadralella polygnathiformis* (Budurov &
neptunian sill with *Halorella*	Stefanov)
	Conodont fragments
	Ostracods
2550	No record
Host limestone	
2552	Ostracods
Host limestone	Crinoid ossicles
	Fish remains
2557	*Paragondolella inclinata* (Kovács)
Host limestone	*Paragondolella praelindae* Kozur
	Paragondolella sp. – juvenile
	Ramiform elements
2559	*Budurovignthus mungoensis* (Diebel)
Host limestone	*Budurovignathus* sp.
	Gladigondolella sp. – juvenile
	Neocavitella sp.
	Paragondolella inclinata (Kovács)
	Paragondolella praelindae Kozur
	Paragondolella ex. gr. *foliata* Budurov
	Paragondolella sp.
	Holothurian ossicles
	Fish remains
2560	*Budurovignathus* sp.
Host limestone	*Neocavitella tatrica* (Zawidzka)
	Ramiform elements

(1987), corrosion appears in conodonts from hydrothermally altered, contact metamorphic rocks and have high CAI (Conodont Alteration Index) values, and it may also be the result of processing. Different degrees of deformation were observed in both platform and ramiform elements being more noticeable in the latter. Similar deformations in conodonts are documented from Triassic rocks of Hungary and Serbia that have undergone regional metamorphism (Kovács and Arkai, 1987, 1989; Sudar and Kovács, 2006).

3.2. Methods

3.2.1. Cathodoluminescence (CL)

Cathodoluminescence (CL) microscopy was employed on polished rock slabs to investigate diagenetic features, cement stratigraphy, and mineral alteration. The technique was selected considering that CL imaging enhances the visibility of growth zonation, recrystallization textures, and compositional heterogeneities that are not discernible under conventional optical microscopy.

3.2.2. Scanning electron microscopy

Samples from the neptunian sill which exhibit *Frutexites*-like microstructures were examined under scanning electron microscope (SEM) with backscattered electron (BSE) imaging. The SEM samples were cut perpendicular to the bedding planes, mounted on specimen stubs and polished. The samples were then etched in 5% HCl for 15–25 s and washed with distilled water, dried and coated with a 10 nm thick gold layer to enhance sample conductivity. The post-polishing etching process was necessary to remove any potential surface contamination.

Additional BSE imaging and EDS elemental maps were performed on iron-rich samples to investigate the presence of *Frutexites*-like structures and assess the distribution of some elements, particularly Fe, Mn, and P. The analyses were carried out with a CAMECA SX-Five electron probe microanalyzer equipped with a Bruker EDS detector, housed in the Department of Geology, Babeş-Bolyai University, Cluj-Napoca. The instrument has a tungsten electron source and is configured with 4 WDS spectrometers, one BSE one SE and one CL detector. Before analysis, the samples that had been previously used for SEM imaging were further polished and coated with a carbon layer to enhance surface conductivity. The operational parameters were set at 20 kV and 60 n-amps. EDS elemental scans were executed with a step size of 1–0.5 mm and a dwell time of 5 ms.

3.2.3. Carbon and oxygen stable isotope analyses

Carbon and oxygen stable isotope analyses were conducted on 52 carbonate powder samples (from host limestone, red carbonate sediments infilling the neptunian dike, dark red to mauve carbonate sediments infilling the neptunian sill, from brachiopod shells, radiaxial cements, late diagenetic cements, see details in Table 4) at the stable isotope facilities of the Iso-Analytical Limited, United Kingdom. Prior to stable isotope analysis, the samples were assessed for potential diagenetic overprinting, using cathodoluminescence and petrographic microscopy. Powdered samples were extracted from the polished surfaces using a Bosch drill fitted with precision bits. The carbonate powders were treated with 100% phosphoric acid at a temperature of 75 °C and the resulting CO_2 was analyzed via Continuous Flow-Isotope Ratio Mass Spectrometry (CF-IRMS). The isotopic results are reported relative to the PDB (PeeDee Belemnite) with a standard deviation of less than 0.04%.

3.2.4. Analytical XR-diffractometry

Analytical XR-diffractometry was employed as an additional tool for screening mineralogical composition, on nine samples. This was performed on nine samples: six red carbonate rock samples (from the infill of the neptunian dike and sill), two host limestone samples, and one limestone fragment from the collapse breccia filled with reddish carbonate matrix (Fig. 3A, F). The diffraction patterns were collected with a Brucker D8-Advance instrument, housed in the Department of Geology, Babes-Bolyai University, Cluj-Napoca. Prior to analysis, about twenty grams from each carbonate rock sample was reduced to very fine powder, and subsequently quartered to ensure a representative average of the rock composition. The instrument was configured with a CuKa tube (l = 1.5418 Å). Operation conditions were set at 40 kV and 40 n-Amps. The instrument uses a Ni filter of 0.0125 mm thickness, and a proprietary LynxEye silicon strip detector. Diffraction spectra were acquired between 5^o and 64^o 2q range, with a counting time of 0.2 s per step. All spectra were fitted for mineral phase identification using DiffracEVA software package alongside the PDF2 reference patterns database from the International Center for Diffraction Data (ICDD). Additionally, all spectra were cross-checked using Match!-4 software package with reference patterns from the Crystallography Open Database (COD).

3.2.5. Elemental analyses

Thirteen samples have been analyzed for major and select trace elemental concentrations, including rare-earth elements and yttrium (REE + Y). The analyzed material was sampled from red and dark red infills of the neptunian dike and sill and also from the host limestone. These samples were dissolved in ultraclean acids at the University of Arizona TIMS laboratory (Otamendi et al., 2012) clean lab, dried out and redissolved in mild 1% nitric acid for chemical analysis. Elemental chemistry was performed on a Thermo XSeries 2 quadrupole ICP-MS using the procedures first described in Rossel et al. (2013) and reduced to a series of internal and external standards commonly used in the lab via Iolite (Paton et al., 2011). Precision is within 3–5% for the analyzed samples. Results are presented in elemental ppm. REE + Y concentrations are normalized to the Post Archaean Australian Shale average – PAAS (McLennan, 1989).

4. Results

4.1. Description of the Leurdeasa Hill section

4.1.1. Petrography and microfacies of the host rock and iron rich carbonates infilling the neptunian dike and sill

The Leurdeasa Hill section comprises lower Carnian well-bedded limestones (Figs. 2A, 3A, I) characterized by strongly cemented lithoclast rudstone (clast-supported forereef limestone breccias) (Fig. 4A-E). The lithoclast rudstone consists of poorly sorted angular to subangular clasts of reef-derived carbonates (Figs. 3D, 4A-D, H) intermixed with angular clasts of pelagic carbonates represented by wackestone containing halobiid bivalves, ostracods and ophiuroids (Fig. 4C-E, H). The clasts are cemented by submarine fibrous and radiaxial calcite cements (Fig. 4A, E, F). Both synsedimentary and diagenetic phases display notable characteristics: micrite precipitation, isopachous fibrous

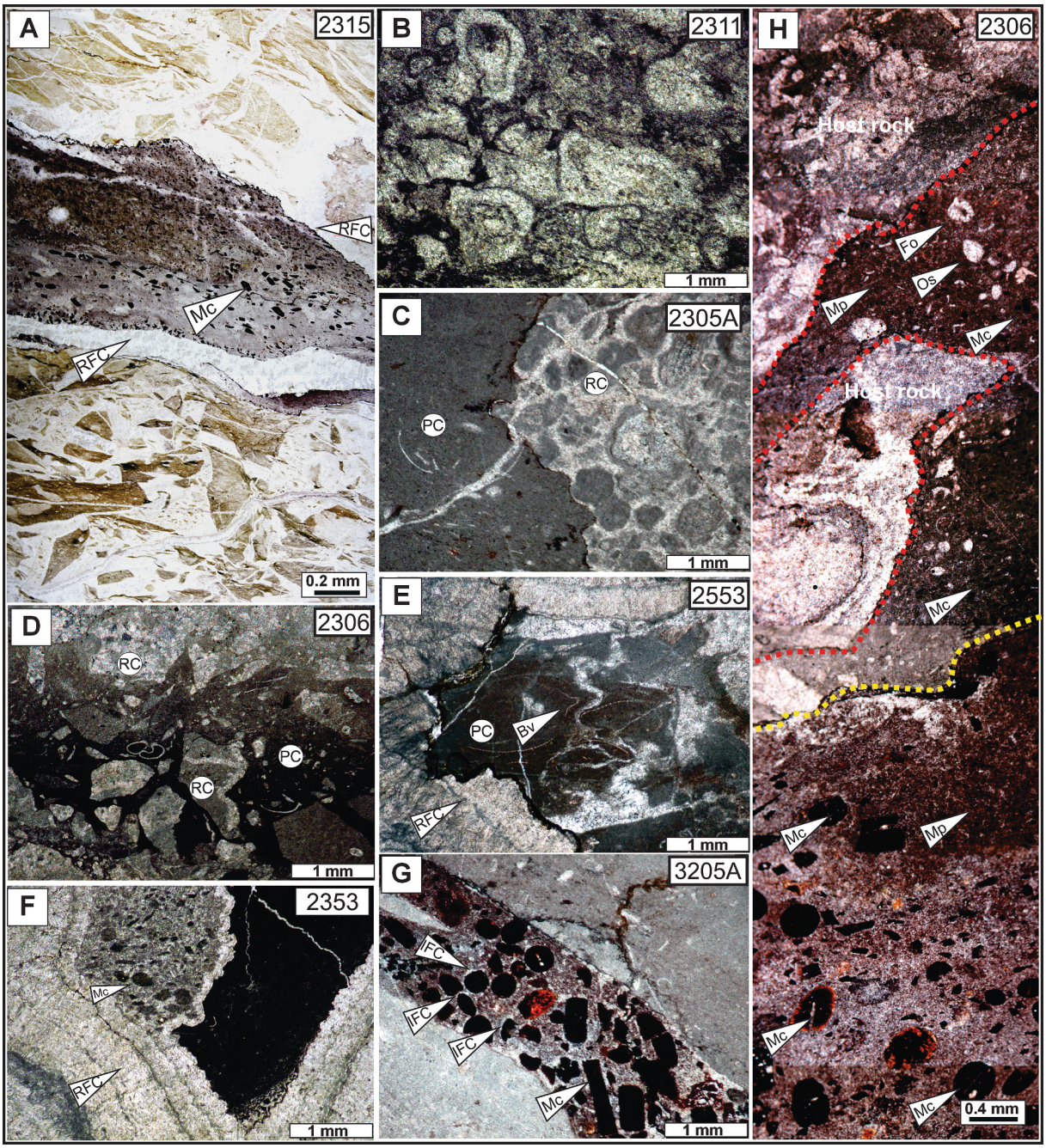

Fig. 4. (A) The contact between host limestone (clast-supported forereef limestone breccia) and the dark-red to mauve bioclastic wackestone-packstone infill of a neptunian sill, microcoprolites (Mc), radiaxial fibrous calcite cements (RFC). (B) Details of reef-derived carbonate clasts. (C, D) Lithoclast rudstone with poorly sorted angular to subangular clasts of reef-derived carbonates (RC) mixed with angular clasts of pelagic carbonates (PC). (E, F) Pelagic carbonates (PC) represented by wackestone with halobiid bivalves (Bv). The clasts are cemented by submarine radiaxial fibrous calcite cements (RFC). (G) Fracture infilled with micropeloidal bioclastic packstone–wackestone with abundant microcoprolites (Mc) with thin peripheral isopachous fibrous cements (IFC). (H) Fracture affecting the host limestones: the infilling of the fracture consists of micropeloidal packstone–wackestone with ostracods (Os), rare foraminiferas (Fo), microcoprolites (Mc) and micropeloidal matrix (Mp). The numbers in the upper right corner of the pictures represent the thin sections' identification numbers. (For interpretation of the references to colour in this figure legend, the reader is referred to the web version of this article.)

cement (IFC) developed around the grains (Fig. 4G) and the presence of radiaxial fibrous cement (RFC) that grows in fissures, fractures, voids and cavities (Fig. 4E, F).

The lithoclast rudstone of this carbonate succession is intersected by a complex network of fractures filled with red and mauve ferruginous carbonates. A first generation of fractures is oriented obliquely and/or parallel to the bedding, ranging from centimeter to meter width, and shows sharp boundaries between the fissure-filling and the host rock (Figs. 2A-F, 3A-I, 4A, G, H). A second generation of fractures which cuts through the first, is of millimeter to centimeter width and shows wavy and undulating boundaries, accompanied by thin peripheral calcite tapestry, consisting of IFC on the walls (Fig. 5A).

Toward the base of the studied section, the fracture system, small cavities and a large neptunian dike (1.2–1.8 m width) are filled by red micropeloidal bioclastic packstone–wackestone containing abundant microcoprolites (Fig. 4G, H, 5A-C) *Halorina cryptica* Lazăr et al., 2020 (Fig. 5B). This assemblage also includes ostracods, rare foraminiferas and ferruginous micrite with clotted microfabric (Figs. 5A, B). The matrix consists of very small micritic grains, ranging from 0.02 mm to approximately 0.15 mm in size. These grains lack internal structure and

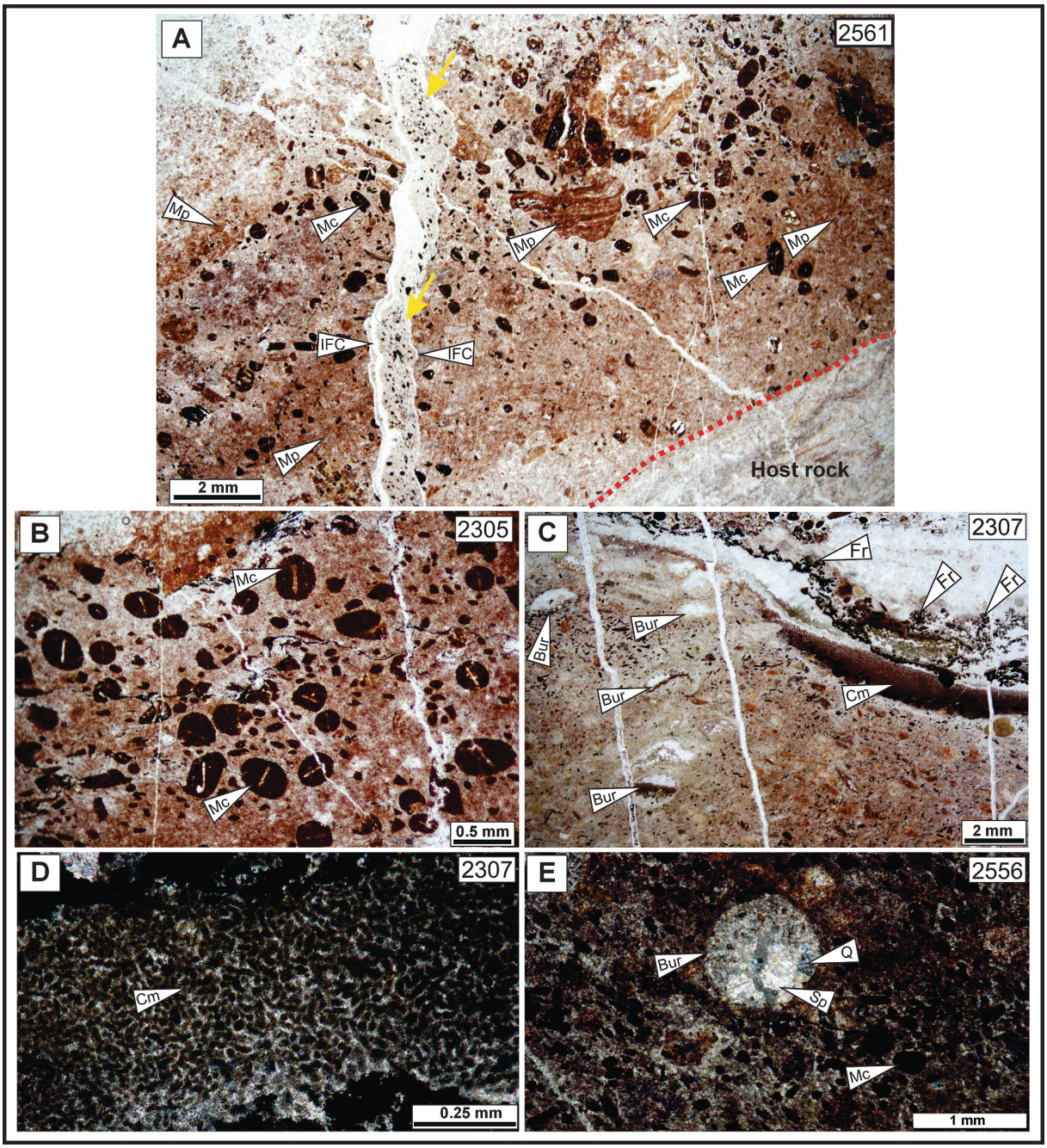

Fig. 5. (A) Fracture affecting the host limestone: the infillings of the fracture consist of micropeloidal packstone – wackestone with microcoprolites (Mc) and micropeloidal matrix (Mp); millimeter-size fractures (yellow arrows, cutting the previous generation of fractures) show wavy and undulating boundaries and thin peripheral isopachous fibrous cements (IFC) on the walls. (B-C) Red carbonate infilling the neptunian dike (micropeloidal bioclastic packstone–wackestone with abundant microcoprolites) shows intensive bioturbation, numerous burrows (Bur) and locally abundant *Frutexites*-like microstructures (Fr). (C, D) Sediment showing in place clotted microfabric (Cm). (E) Burrow completely filled with sparite cements (Sp), quartz (Q) and with micropeloidal bioclastic wackestone. (For interpretation of the references to colour in this figure legend, the reader is referred to the web version of this article.)

exhibit cloudy centres and ovoid, rounded, rod-like or irregular shape. In some places, pocket-like small cavities are filled with clotted or peloidal microfabrics and cements (Fig. 5C-D). The red carbonate sediment shows intensive bioturbation (Fig. 5A-C) and contains numerous burrows, 0.5–4.0 mm in diameter, completely filled either with sparite cements, or with micropeloidal bioclastic wackestone matrix (Fig. 5C, E).

The next infilling consists of dark-red to mauve carbonate,

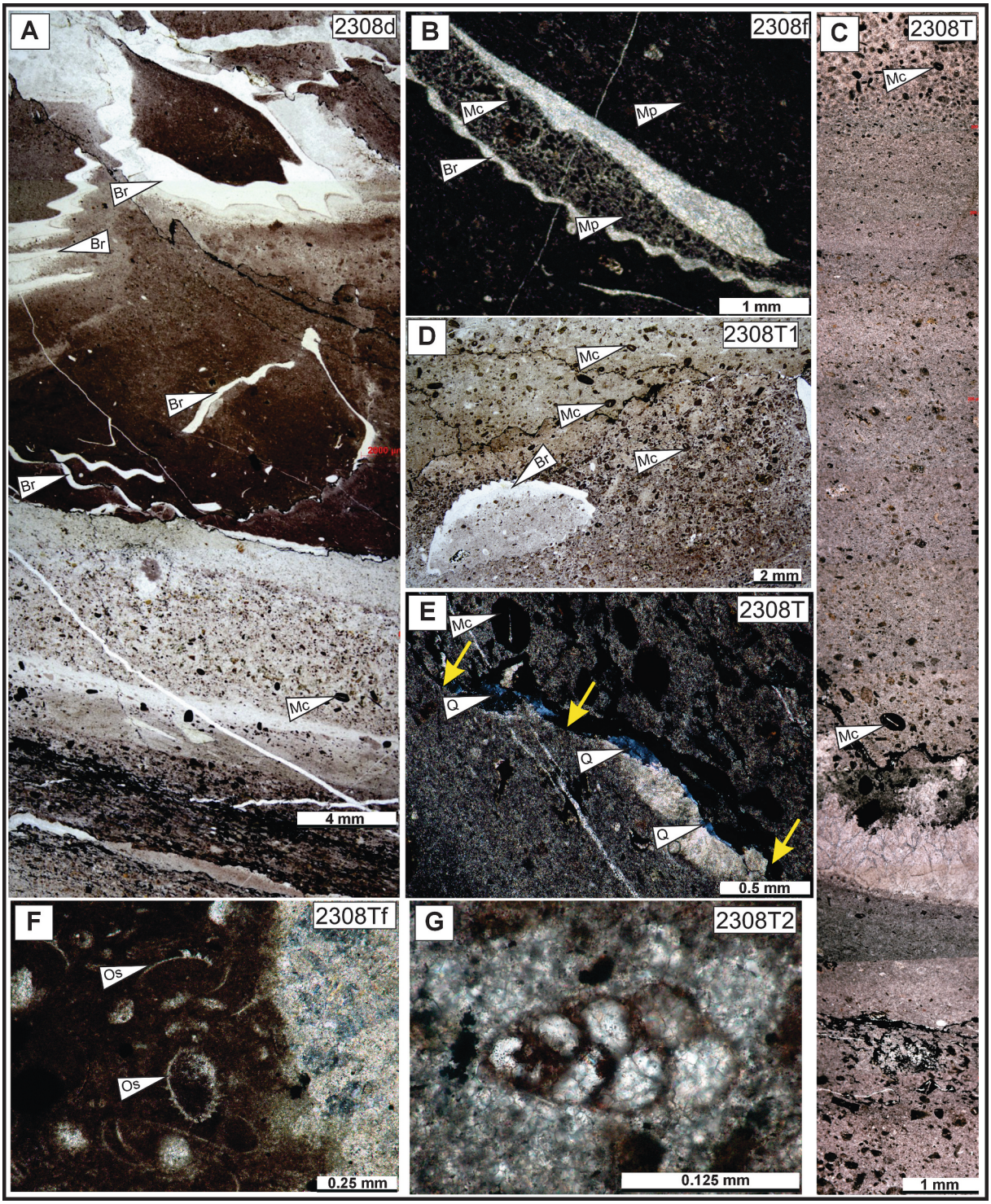

Fig. 6. Features of the dark-red to mauve carbonates infilling the neptunian sill: (A) Sharp transition from red bioclastic micropeloidal wackestone-packstone with recrystallized matrix with *Halorina cryptica* microcoprolites to dark red to mauve bioclastic packstone-wackestone to floatstone containing abundant *Halorella* shells (Br) and microcoprolites (Mc). (B-D) Bioclastic wackestone-packstone to floatstone with *Halorella* shells (Br) and microcoprolites (Mc) reveal a dens micropeloidal matrix (Mp). (C) Transition from wackestone-packstone with less microcoprolites to micropeloidal wackestone-packstone with recrystallized matrix, containing abundant microcoprolites. (E) Local quartz (Q) lens along the erosional contact (yellow arrows) of successive influxes of internal sediment inside the neptunian sill. (F) The associated microfauna is represented by abundant ostracods (Os). (G) Rare benthic foraminiferan, *Trochosiphonia josephi.* (For interpretation of the references to colour in this figure legend, the reader is referred to the web version of this article.)

representing the internal sediment of a large neptunian sill (0.30–0.60 m thick) located toward the topmost part of the Leurdeasa Hill section which runs nearly parallel with the bedding surfaces of the host limestone (Figs. 2A, 3A, E-H). There is a sharp transition from red bioclastic packstone-wackestone containing *Halorina cryptica* microcoprolites to dark red to mauve bioclastic packstone to floatstone containing abundant *Halorella* shells and microcoprolites (Figs. 3D, E, 6A). This bioclastic packstone to floatstone with *Halorella* shells and microcoprolites exhibits a dense micritic, micropeloidal matrix (Fig. 6B, E, F). The associated microfauna includes abundant ostracods (Fig. 6F) and rare benthic foraminifera (Fig. 6G). Both red and dark-red to mauve internal carbonate sediments show parallel, oblique to irregular, wavy lamination, successive erosion surfaces and alternation from packstone-wackestone with fewer microcoprolites to micropeloidal wackestone-packstone with recrystallized matrix, rich in microcoprolites (Figs. 5A-C, 6A, C). Rare quartz (Q) concentrations were observed inside the burrows (Fig. 5E) and along the contact between successive influxes of internal sediment of the neptunian sill (Fig. 6E).

Frutexites-like microstructures showing dendritic to complex multi-lobate morphology (Fig. 7A-H) have been observed within micropeloidal wackestone-packstone with recrystallized matrix, rich in microcoprolites which form the infill of the neptunian dike and sill. *Frutexites* appears as branching-diverging columns surrounded by sparite cement (Fig. 7A-D) or by microcrystalline cement (Fig. 7F, G) or by

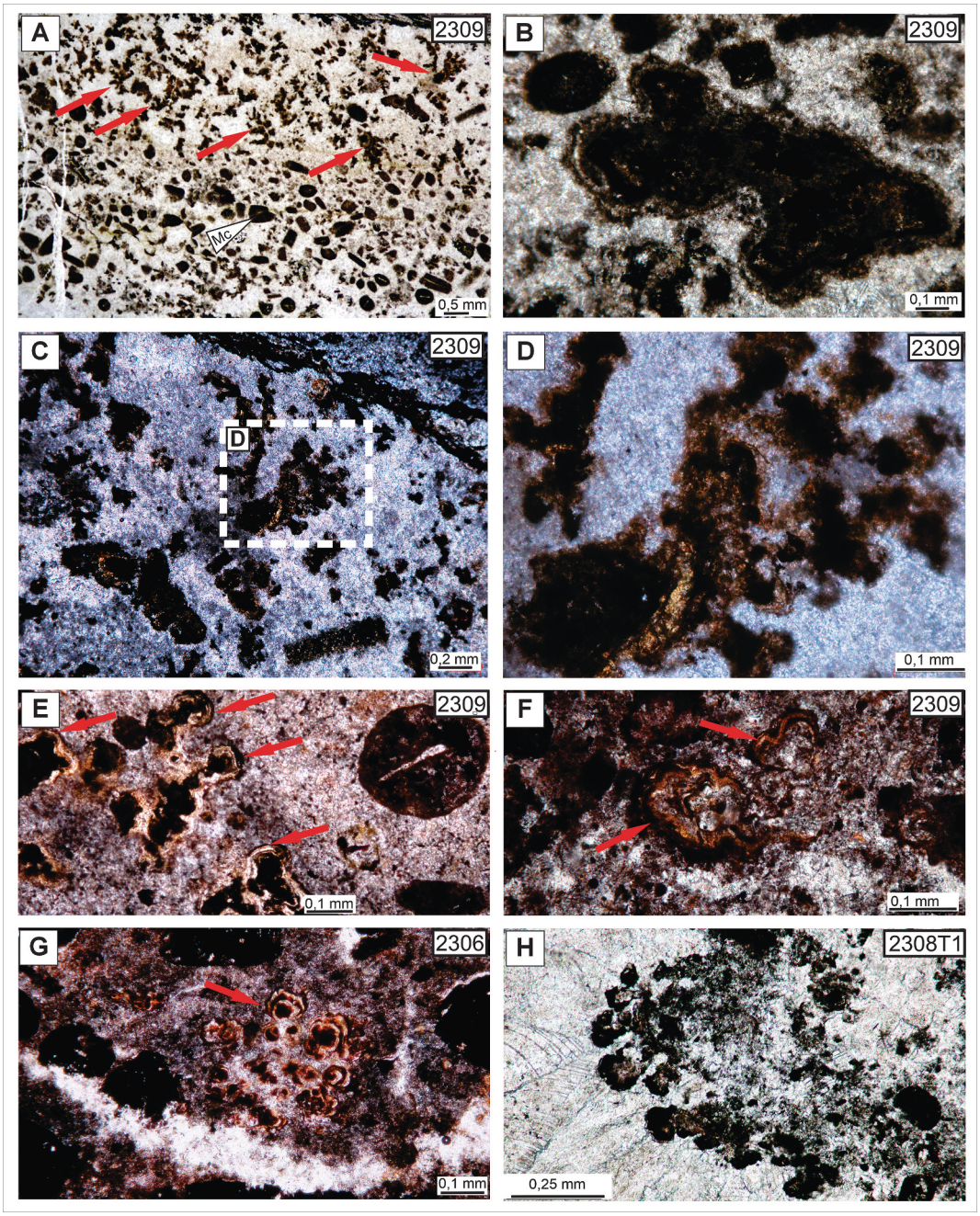

Fig. 7. *Frutexites*-like microstructures: (A–D) Micropeloidal wackestone-packstone with recrystallized matrix, with abundant microcoprolites (Mc) and dendritic microstructures (red arrows). (B) Microstructure with multi-lobate morphology and without distinct mesofabric but possessing micritic, clotted or peloidal microfabrics. (C, D) Dendritic microstructures showing spheroidal texture on the base and irregular laminated texture of the dendritic branches. (*E*-G) Multi-lobate morphology with thin convex-upward laminae (red arrows). (H) Microstructure with multi-lobate morphology surrounded by radiaxial fibrous cement (RFC). (For interpretation of the references to colour in this figure legend, the reader is referred to the web version of this article.)

radiaxial fibrous cement (RFC) (Fig. 7H). The *Frutexites*-like microstructures consist of iron rich micrite and/or a meshwork of iron rich micropeloids showing spheroidal to irregular laminated fabric, as indicated by colour and texture variations of ferruginous micrite and clusters of micropeloids (Fig. 7C-E). In cross- or oblique-section, the columns are topped by convex-upward laminae. These laminae are black opaque minerals (Mn rich), or dark reddish to brown semitranslucent minerals (Fe-rich) and yellow-white carbonate minerals (Fig. 7E-G). The walls of the branches may be thin, opaque, exhibiting dark reddish to brown hues with clear outline (Fig. 7F-G), or they may be reddish to brown in colour with a diffuse outline in thin section (Fig. 7B, D, H). The microstructures of *Frutexites*-like shrubs reveal the presence of different types of curved filaments less than 0.5–1.5 μm width and 5–20 μm maximum observed length, forming a dense network (Fig. 8A-C). Some filaments show dichotomous branching at apical nodes (Fig. 8A, B), while microfilaments with ribbon-like stalks (Fig. 8C) and rod-shaped bacilliform structures (Fig. 8D) associated with mineralized extracellular polymeric substance (EPS) remains incorporating calcite nanocrystals have been observed (Fig. 8A, B).

4.1.2. *Diagenetic features of the iron rich carbonates infilling the neptunian dike and sill*

The first stage of diagenesis is represented by radiaxial fibrous cement (RFC) developed around the voids and cavities and growing directly on the inner part and on the outer surface of the brachiopod shells (Fig. 9A-D). Furthermore, RFC grows around *Frutexites*-like microstructures (Fig. 9E, F) preserving delicate (possible) microbial fabrics (Fig. 7H). Under CL microscopy, the RFC cement appears as non-luminescent and is occasionally postdated by scalenohedral calcite displaying dull luminescence with bright luminescent outer rims (Fig. 9C). The interface between the RFC and scalenohedral cements (SC) is distinctly observable under CL. The RFC can sometimes undergo recrystallization to saddle dolomite and shows a patchy or zoned luminescence. The remaining inner pore space is closed by drusy and blocky calcite that shows bright luminescence.

4.2. *Conodonts from the host limestones*

The microfauna recovered from the examined samples consist of conodont elements along with ostracods, rare echinoderm ossicles (crinoids, holothurians), as well as fish remains. The preservation of the microfauna is moderate, and conodont elements have high Colour Alteration Index value (CAI = 7–7.5) (Rejebian et al., 1987). The conodont assemblages include two subfamilies, Paragondolellinae and Pseudofurnishinae. The following taxa have been determined: *Budurovignathus mungoensis* (Diebel, 1956), *Budurovignathus* sp., *Gladigondolella* sp., *Neocavitella tatrica* (Zawidzka, 1972), *Neocavitella* sp., *Paragondolella inclinata* (Kovács, 1983), *Paragondolella praelindae* Kozur, 2003, *Paragondolella* ex gr. *foliata* Budurov, 1975, *Paragondolella* sp., *Kraussodontus* aff. *Praeangustus* (Kozur, Mirăuţă and Mock *in* Kozur, 1980), *Quadralella polygnathiformis* (Budurov and Stefanov, 1965), *Quadralella* cf. *acuminata* (Orchard, 2007), *Quadralella* sp., and ramiform elements (Table 1, Fig. 10). Elements of *Budurovignathis mungoensis* (Fig. 10 specimens 6a-c) are marked by a platform that occupies at least 2/3 of the total unit length with a pointed posterior end. Well-developed nodes are present on both margins of the platform. The carina increases toward the anterior part, in correspondence with the free blade. A well-developed keel is widest at the pit and it may bifurcate behind it. The pit is small and elongate, located approximately at the centre of the unit. The species is well recognized in the Tethys realm, specifically in the strata that range from the upper Ladinian to the lower Carnian (Kozur, 1980; Kovács and Kozur, 1980; Krystyn, 1980; Kolar-Jurkovšek, 1991). Additionally, the material includes several smaller size specimens that likely represent a transitional form between *B. mungoensis* and

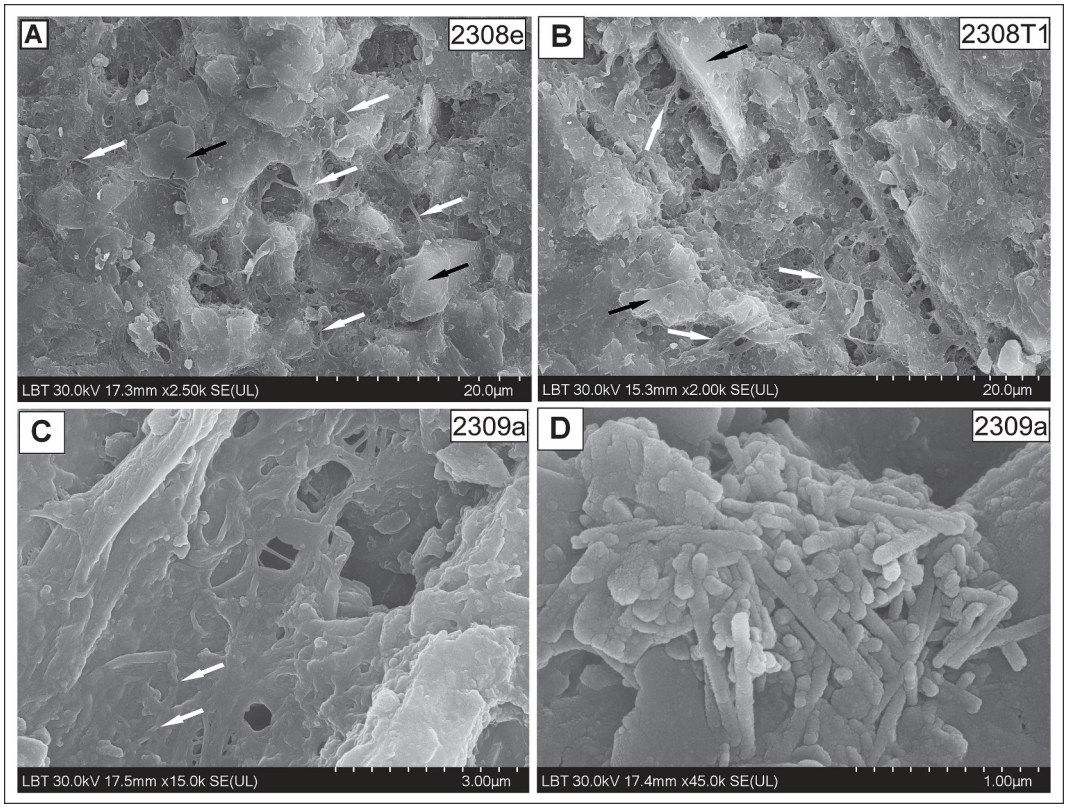

Fig. 8. *Frutexites* SEM images: (A–C) Different types of curved filaments forming a dense network of extracellular polymeric substances (EPS, white arrows) overlie finely crystalline calcite (black arrows). (C) Dense network of filaments, note the ribbon-like stalk, resembling *Mariprofundus ferrooxydans* (white arrow). (D) Rod-shaped bacilliform structures incorporating calcite nanocrystals.

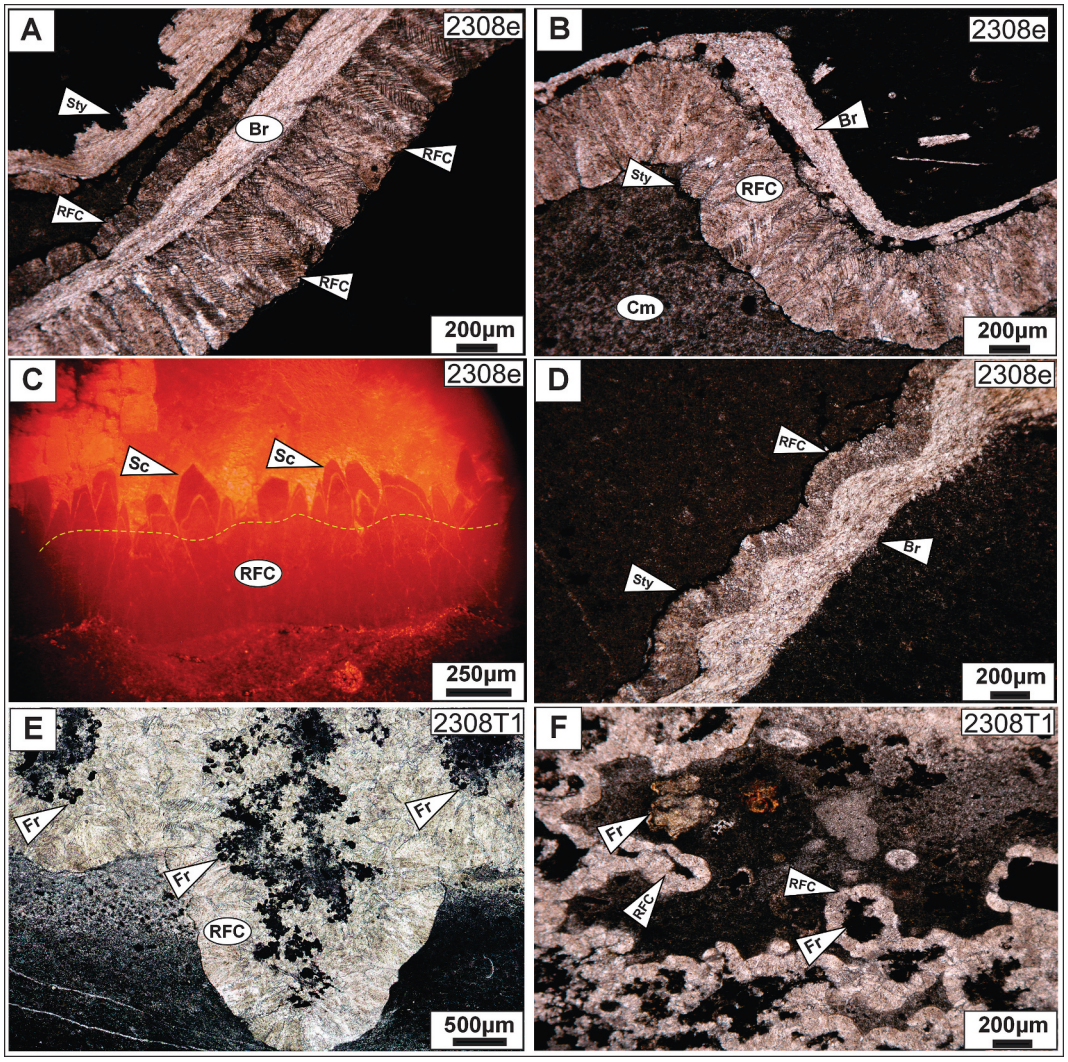

Fig. 9. Diagenetic features of the iron rich carbonates infilling the neptunian dike and sill system: (A) Radiaxial fibrous cement (RFC) growing on the inner part and on the outer surface of the brachiopod shell (Br). Dissolution-seams (Sty) at the contact between sediment and brachiopod shell. (B) On the inner surface of the brachiopod shells (Br) occurs radiaxial fibrous cement (RFC). Dissolution-seams (Sty) at the contact between sediment and RFC. The matrix shows a clotted microfabric (Cm). (C) Non-luminescent radiaxial-fibrous cements (RFC) form the first generation nucleating directly on cavity walls and is overlain by bright luminescent scalenohedral cement (Sc). (D) Radiaxial fibrous cement (RFC) growing on the outer surface of the brachiopod shell (Br). Dissolution-seams (Sty) at the contact between sediment and RFC. (E-F) Radiaxial fibrous cement (RFC) growing around iron-rich microstructures with dendritic-like or complex multi-lobate morphology and micritic, clotted or peloidal microfabrics (Fr).

Budurovignathus mostleri (Kozur *in* Kozur and Mock, 1972). A few specimens are referred to *Kraussodontus* aff. *praeangustus* (Fig. 10, specimens 5a-c). They bear a narrow platform with subparallel lateral margins and a low carina. The specimens differ from the holotype which reveals more upturned lateral margins. This species was first described from the deposits of Julian age from Dobrogea and according to Kovács and Kozur (1980) its stratigraphic range extends to the middle Tuvalian.

Specimens of *Neocavitella tatrica* (Fig. 10, specimens 1a-b) present a widely opened basal cavity with very prominent cusp that is more than twice as large than the other denticles and is strongly inclined posteriorly. The cusp is followed by 5–6 denticles of almost equal size. The lower margin of the unit is nearly straight. The species has been described from the Tatra Mountains, Poland (Zawidzka, 1972) and it ranges from the Longobardian to the Cordevolian (Kovács and Kozur, 1980), and in the Julian (Chen et al., 2015) respectively.

Paragondolella inclinata (Fig. 10, specimens 7a-c, 8a-c) is characterized by units with a long platform extending for most of its length, with a rounded posterior end. The carina is moderately high. A raised keel is posteriorly widened and blunted. The ovaloid basal pit is located terminally. This species is closely related to *P. foliata* (Kovács, 1983). The stratigraphic range of *P. inclinata* is from the Longobardian to Late Julian (Kovács, 1983; Chen et al., 2015).

Slightly arched units of medium size are characterized by posterior constriction of the platform are attributed to *Paragondolella praelindae* (Fig. 10, specimens 2a-c). The constricted part is asymmetric and rounded. The platform is widest in the middle part of the unit and it gently narrows anteriorly. The upturned lateral margins of the platform are devoid of ornamentation. The blade is constituted of up to 14 denticles with relatively high tips. The cusp is followed by a smaller denticle. Distinct narrow keel ends up in ovaloid loop with small but distinct pit. *P. praelindae* was first described from the Lower Tuvalian strata of Silicka Brezova (Kozur, 2003), but it extends upwards and ranges into the Julian (Rigo et al., 2018). Very few specimens determined as *Paragondolella* sp. (sample 2310) represent an immature stage with well-developed platform that tapers evenly to both ends, one posteriormost end is marked by constriction. The carina is composed of 9 denticles of nearly same height. Very rare specimens of *Quadralella polygnathiformis* (Fig. 10, specimens 4a-c) are characterized by an

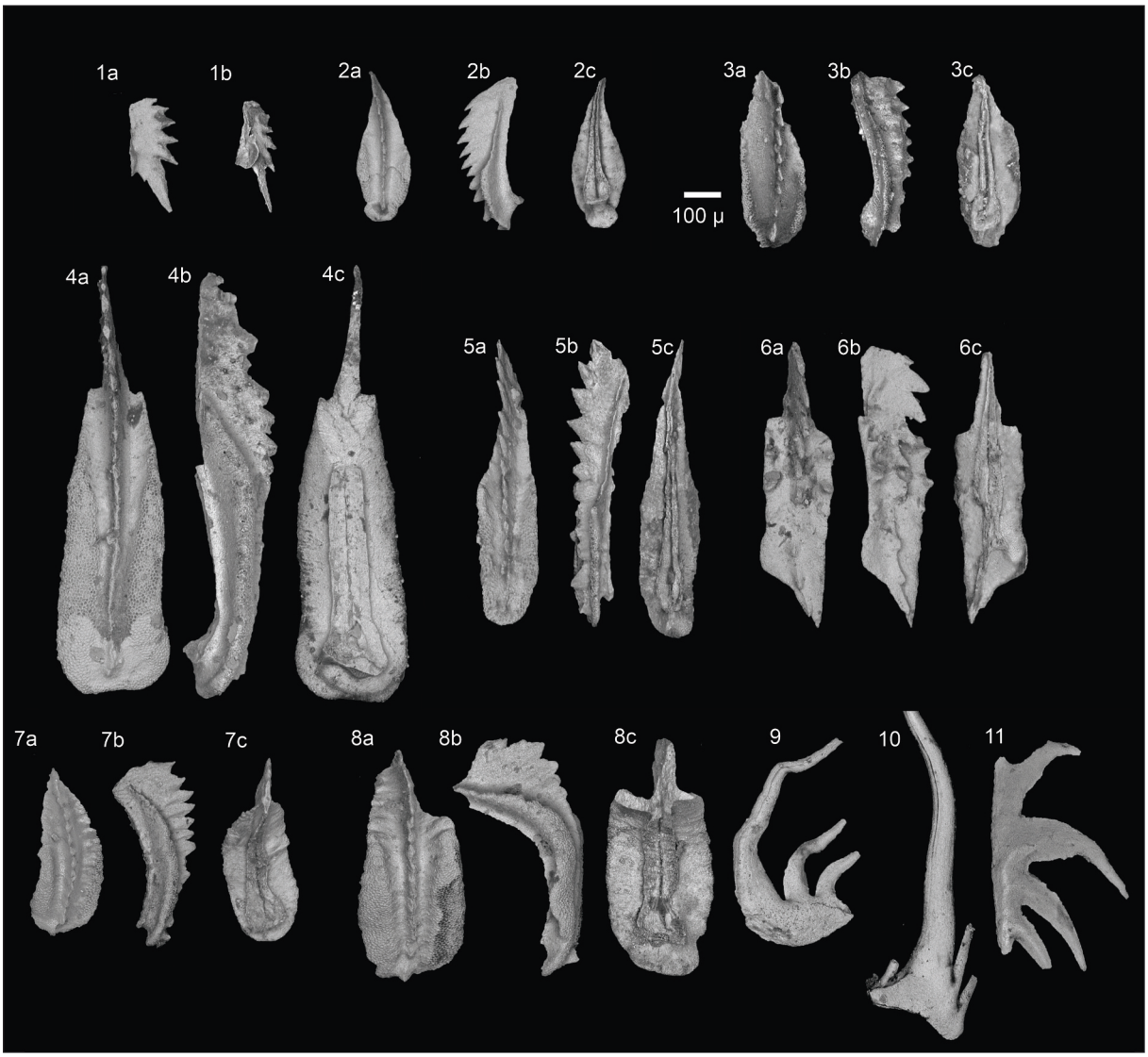

Fig. 10. Conodonts from Leurdeasa Hill, Lower Carnian:
1: *Neocavitella tatrica* (Zawidzka). Sample 2310.
2: *Paragondolella praelindae* Kozur. Sample 2310.
3: *Quadralella* cf. *acuminata* (Orchard). Sample 2310.
4: *Quadralella polygnathiformis* (Budurov & Stefanov). Samples: 2310.
5: *Kraussodontus* aff. *praeangustus* (Kozur, Mirăuţă & Mock). Sample 2310.
6: *Budurovignathus mungoensis* (Diebel). Sample 2310.
7–8: *Paragondolella inclinata* (Kovács) deformed. Samples 2559.
9–11: ramiform elements. Samples 2559 (specimens 9 and10), 2557 (specimen 11).

unornamented platform with sub-quadrate posterior. The carina is composed of posteriorly slightly inclined denticles that decrease toward the posterior margin, while the fixed blade is constituted of 4–6 denticles. A well-differentiated cusp is separated by a narrow brim from the posterior end. The keel is broad with a distinct median furrow and its posterior end reveals a tendency to bifurcation. The basal pit is small and ovaloid. Numerous studies have demonstrated that this species is very common in the Tethys realm. *Q. polygnathiformis* is a long ranging species and it appears throughout the entire Carnian, except for its uppermost part (Kolar-Jurkovšek and Jurkovšek, 2019).

The units of *Quadralella* cf. *acuminata* (Fig. 10, specimens 3a-c) are arched or at least the posterior-most part is bent downward and the axis in this part might be curved. A well-developed asymmetric platform is widest in its middle part and it abruptly tapers posteriorly. The blade-carina is constituted of denticles fused for most of their height leaving out only denticle tips free, the overall blade-carina is increasing slightly toward the anterior. The well-developed cusp is separated from the posterior end by a brim. The pit is surrounded by the loop that tends toward a more squared termination, which follows the tapering of the posterior platform. *Q. acuminata* has been reported from the Ladinian-Carnian boundary interval in British Columbia where it marks the *acuminatus* Zone and it also appears in the *intermedius* Zone (Orchard, 2007).

4.3. Fossil assemblage from the studied neptunian dike and sill

Taphonomy: At the base of the neptunian sill, brachiopods are found as densely packed clusters (0.1–0.15 m thick) of disarticulated and broken shells, alongside articulated specimens (Figs. 2E, 3E, 11E). Notably, these brachiopod shells exhibit generally good preservation of

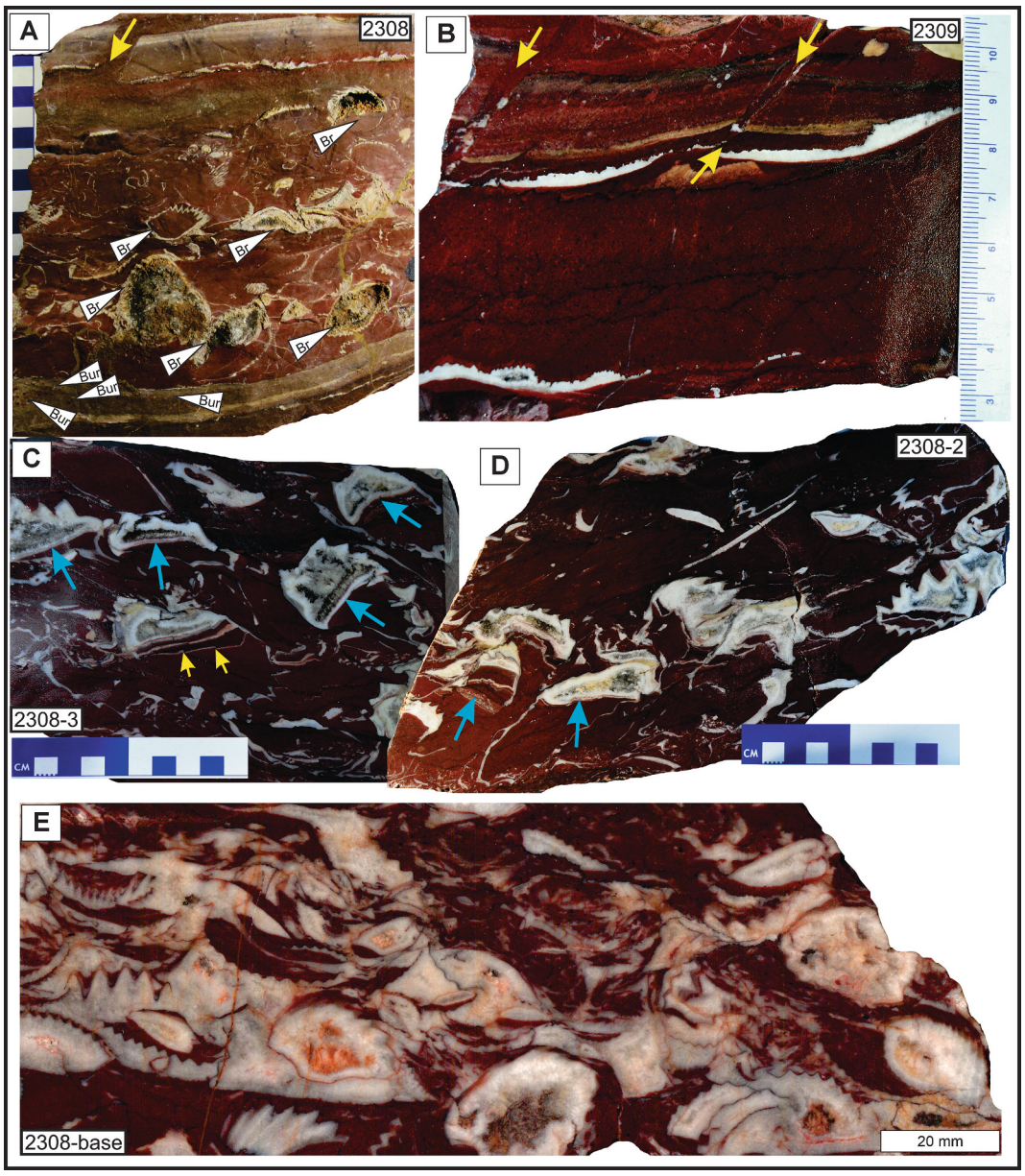

Fig. 11. Infill of the neptunian sill: (A-D) Polyphase infilling of the neptunian sill with iron-rich carbonates; the majority of the brachiopod shells (Br) are articulated and show varying degrees of geopetal infilling; (A, B) Note the fractures disrupting lamination of previously formed carbonates (yellow arrows); (C) Note disruptions of the isopachous-fibrous calcite (FC) seams (yellow arrows); (C, D) The alignments of the geopetal fabrics inside of the brachiopod shell show slightly different orientations (blue arrows); (E) At the base of the neptunian sill the brachiopods are tightly packed masses of disarticulated, broken and articulated shells. (For interpretation of the references to colour in this figure legend, the reader is referred to the web version of this article.)

both internal and external skeletal elements, displaying a bimodal sorting pattern that includes complete shells as well as shell debris. There are no apparent signs of abrasion, bioerosion or encrustation. Under microscopic magnification (Figs. 6A, B, D; 9A, B, D) encrusting organisms or typical macrobioerosion produced by endolithic sponges (e.g. *Entobia*) were not observed on the brachiopod shells. Toward the center and the upper part of the neptunian sill (0.25–0.35 m thick), the majority of the brachiopod shells become articulated and present varying degrees of geopetal infilling (Figs. 2C, 11A-D). This distribution pattern of the brachiopod shells can be observed across approximately 7 m width of the neptunian sill. Of the observed specimens, 90 % are partially filled with the same sediment characterizing the surrounding matrix (iron-rich micropeloidal carbonate) and exhibit sequential nucleation of early radiaxial fibrous calcite, followed by late blocky cements, resulting in geopetal structures. The alignment of the geopetal fabrics inside the brachiopod shells reveal slightly different orientations (Fig. 11C-D). Additionally, deformed articulated brachiopod shells were observed throughout the thickness of the neptunian sill (Fig. 11D). Particularly toward the upper section of the sill, the larger specimens exhibit substantial deformations, though the shells remained articulated.

Brachiopods specimens exhibit diagnostic features of *Halorella*.

External morphology: The *Halorella amphitoma* specimens from Leurdeasa Hill are large-sized with variable outline, typically transverse-oval but also can be subpentagonal, or sphaerical (Fig. 12 A-P). In terms of external dimensions, the width (W) is greater than the length (L), while the thickness (T) is the smallest of the three external dimensions. In some specimens, L and W may be nearly equal, particularly in some juvenile specimens and larger individuals with a subpentagonal outline. One such large specimen LPB IIIb 823 (Fig. 12M), is 41.52 mm length

and 43.20 mm width, although it has been taphonomically deformed. The juvenile specimens (Fig. 12A) display length between 8.44 and 12.37 mm and width between 10.5 and 13.43 mm. Maximum dimensions for *Halorella* have been obtained from individual fragmentary remains, rather than from a single complete specimen. A large fragmentary specimen measures 67 mm in length (specimen LPB IIIb 827), with the complete specimen estimated to reach at least 80 mm in length. Based on half a valve and umbo from another deformed specimen (LPB IIIb 828), its maximum width is estimated to range between 90 and 100 mm. The overall size distribution of adult subpentagonal specimens shows L values between 21.16 and 47.7 mm and W values between 24.28 and 39.02 mm. Transversal-oval specimens, display L values between 12.95 and 39.7 mm and W values between 29.2 and 59.46 mm. The $\log_2$ shell area (i.e. the product of width and length) for the adult transversal-oval specimens display values between 9.21 and 12.42 and for the subpentagonal specimens between 9.0 and 12.03. (Supplementary materials 1). Moreover, a transverse section through one specimen (LPB IIIb 837) suggests that its maximum thickness was approximately 41–42 mm. Costae are typically sharp and well-defined (Fig. 12I-P). The specimens display variable numbers of costae, ranging from less than 10 to approximately 24. Forms with fewer costae (Fig. 12P) could be regarded as a separate species, distinct from many of the more highly costate forms (Fig. 12A-O). However, considering these as two separate species, rather than recognizing these as variable or aberrant forms of *Halorella amphitoma* (Bronn, 1832) currently serves no practical purpose. Moreover, Dagys (1963) was followed by Siblík (1988) in synonymizing *Halorella pedata* (Bronn, 1832) (a form with fewer costae) with *Halorella amphitoma*. Siblík and Bryda (2005) recorded *Halorella amphitoma* from Hochschwab, Austria as having an ornament of coarse ribs numbering between 8 and 26. The majority of the adult specimens of *Halorella* from Leurdeasa Hill are characterized by transverse-oval, subpentagonal and sphaerical outlines and display a distinct geniculation of the shell (at an angle of 100° – 110°), just a few millimetres before the anterior margin.

Internal morphology: The most effective approach to explore the internal structures of the brachiopods from Leurdeasa Hill has been to examine on serially ground polished surfaces of rock hand specimens containing brachiopods, as well as examining sections from specimens embedded in matrix within rock slabs. In these instances, obtaining duplicate casts or maintaining accurate spacing between sections was not possible (cf. Sandy, 1989), yet details of some internal structures were nonetheless observed (Supplementary materials 2). A small dorsal median septum has been observed in one specimen (Supplementary materials 2H) and in addition details observed in longitudinal sections through the dorsal and ventral umbos (Supplementary materials 2C-G). In this series of sections and peels it is possible to observe a robust socket ridge on one side of the brachiopod (Supplementary materials 2D) which supports a ventrally convex crura (Supplementary materials 2F). An attempt to prepare a more complete series of serial sections through another specimen was unsuccessful, as the crura were absent, despite the specimen having a red micritic infilling matrix (micrite is often an ideal matrix for the preservation of the internal structures of brachiopods). The specimen, as with many others from Leurdeasa Hill, was distorted. However, it is evident that internal structures are preserved in certain specimens (Supplementary materials 2H, I). Manceñido and Motchurova-Dekova (2010) identified *Halorella* as having ciliform ("chisel-shaped") crura, contained within their ensimergal "crural" group that characterize the Superfamily Dimerelloidea. Ager (1968) in comparing serial sections from a specimen of *H. amphitoma* from Austria (Ager, 1968, Fig. 1) with those of a specimen from Tadjikistan (Dagys, 1963, fig. 63), concluded that the dorsal median septum exhibits variable development.

Ostracods are numerous, as seen in thin sections, yet extracting them from the limestone matrix through chemical processing (hot acetolysis) proved challenging. Disarticulated valves are visible, but only complete carapaces have been successfully extracted, suggesting that the assemblage might have undergone only limited transport. All ostracods are small and poorly preserved, with their external surfaces seemingly dissolved. Nonetheless, several taxa can be differentiated, including the genus *Polycope* Sars, 1866, along with members of the Bairdioidea, Cytheroidea and Cypridoidea.

Crustacean decapod microcoprolites are highly abundant within the internal sediments of the studied neptunian dike and sill. Lazăr et al. (2020) reported a mass-occurrence of *Halorina cryptica* from the same location, describing in detail the burrows observed within the internal sediment, most likely produced by the same crustacean decapods that generated the microcoprolites. While the microcoprolites are generally well-preserved in cross- and longitudinal-sections, some broken and abraded fecal pellets can also be found.

Foraminifera: Benthic foraminifera are rare in the studied thin sections from the infilling of the neptunian dike and sill. Several specimens associated with *Halorella* and *Halorina* assemblages show a non-twisted triserial test in the first stage and a wall showing the typical hue of originally aragonite foraminifers. These features point to the robertinid species *Trochosiphonia josephi* Rigaud et al., 2015 (Fig. 6G), and a possible Norian marker (S. Rigaud, 2020 pers. written comm.).

4.4. Mineralogy and geochemistry

4.4.1. Mineralogy of the red carbonate sediment infilling the sill and dike

X-ray diffraction analysis (XRD) of the carbonate internal sediment, which constitutes the carbonate infill of the neptunian dike and sill system, reveals that hematite is the predominant ferriferous component in nearly all of the investigated samples (Fig. 13A). The mineralogical profile is largely characterized by the presence of calcite phase. Nevertheless, traces of silica in the form of quartz, as well as traces of iron oxide in the form of hematite, are commonly observed in all red carbonate sediment samples. Additionally, quartz traces are also identified in the host limestone samples and in the limestone fragments from the red matrix breccia, which notably lack iron oxides. This simple mineralogy corroborates the presence of iron oxides, which appear microscopically as seams or fine grains dispersed throughout the carbonate matrix and sparce quartz grains spotted in some samples (Fig. 6E). This simple mineralogy is further validated by BSE imaging and EDS elemental scans, which also indicate the presence of phosphate minerals – likely in the form of apatite – located at the margins of burrows and microcoprolites. Additionally, the presence of dispersed clusters of Fe oxides-phosphates is noted within the dark-red sediment.

4.4.2. Major and rare-earth elements and yttrium (REE + Y)

Thirteen samples have been analyzed to determine their composition of major and trace elements as well as rare-earth elements and yttrium (REE + Y). The samples were obtained from the red and dark red infills of the neptunian dike and sill, as well as from the host limestone. The data are presented as weight percentages for major elements (Table 2) and in parts per million (ppm) for trace elements and REE + Y (Table 3).

Major elements: All but one of the samples exhibit a calcium (Ca) content ranging from 30.4 to 44 wt% (Table 2). The exception is one sample that has a Ca content as low as 19%. The magnesium (Mg) content across all samples remains relatively constant, falling between 0.2 and 0.4 wt%. Additionally, all samples contain moderate to high concentrations of iron (Fe) which varies between 0.14 and 5.99 wt%, as well as variable concentrations of manganese (Mn) that range from low to high, specifically from 0.03 to 5.7 wt%. Notably, the samples exhibiting higher density of microcoprolites and *Frutexites*-like microstructures (samples 2305, 2308, 2309 and 2315, Figs. 5–7) show the highest recorded concentration of Fe and a strong correlation with vanadium (V). While this correlation with high abundance of microcoprolites and *Frutexites*-like microstructures holds true for Mn as well, it is important to note that not all samples containing microcoprolites display elevated Mn concentrations. This observation is confirmed by EDS elemental scan, which shows that some coprolite micro-pellets (as well as burrows)

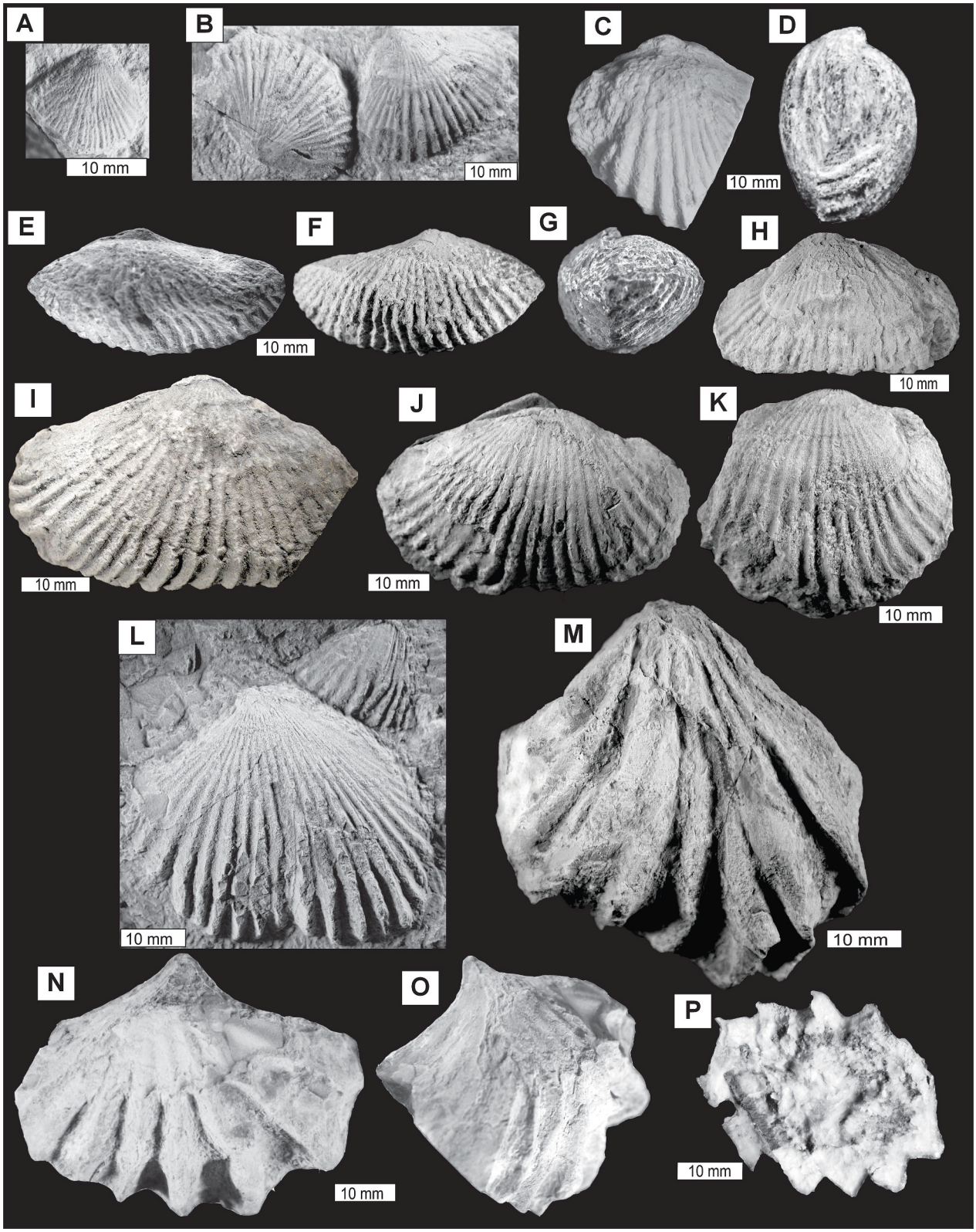

Fig. 12. *Halorella* specimens from the neptunian sill: (A) LPB IIIb 832, juvenile, ventral view; (B) LPB IIIb 816 a, b: 816a on right; 816b on left; (C) LPB IIIb 802, dorsal view; (D) LPB IIIb 801, lateral view; (E, F, G) LPB IIIb 806, compressed specimen, (E) dorsal view, (F) ventral view, (G) lateral view; (H) LPB IIIb 814 dorsal valve, (I) LPB IIIb 807?ventral valve; (J) LPB IIIb 829, dorsal view, (K) LPB IIIb 808?dorsal valve, a large specimen preserving sharp costae, gently geniculated toward anterior margin; (L) LPB IIIb 817 ventral valve; (M) LPB IIIb 823 ventral valve; (N, O) LPB IIIb 822, (N) dorsal view, (O) lateral view of the ventral valve; (P) LPB IIIb 836 approximate transversal cross-section through a medium size specimen with sharp costae.

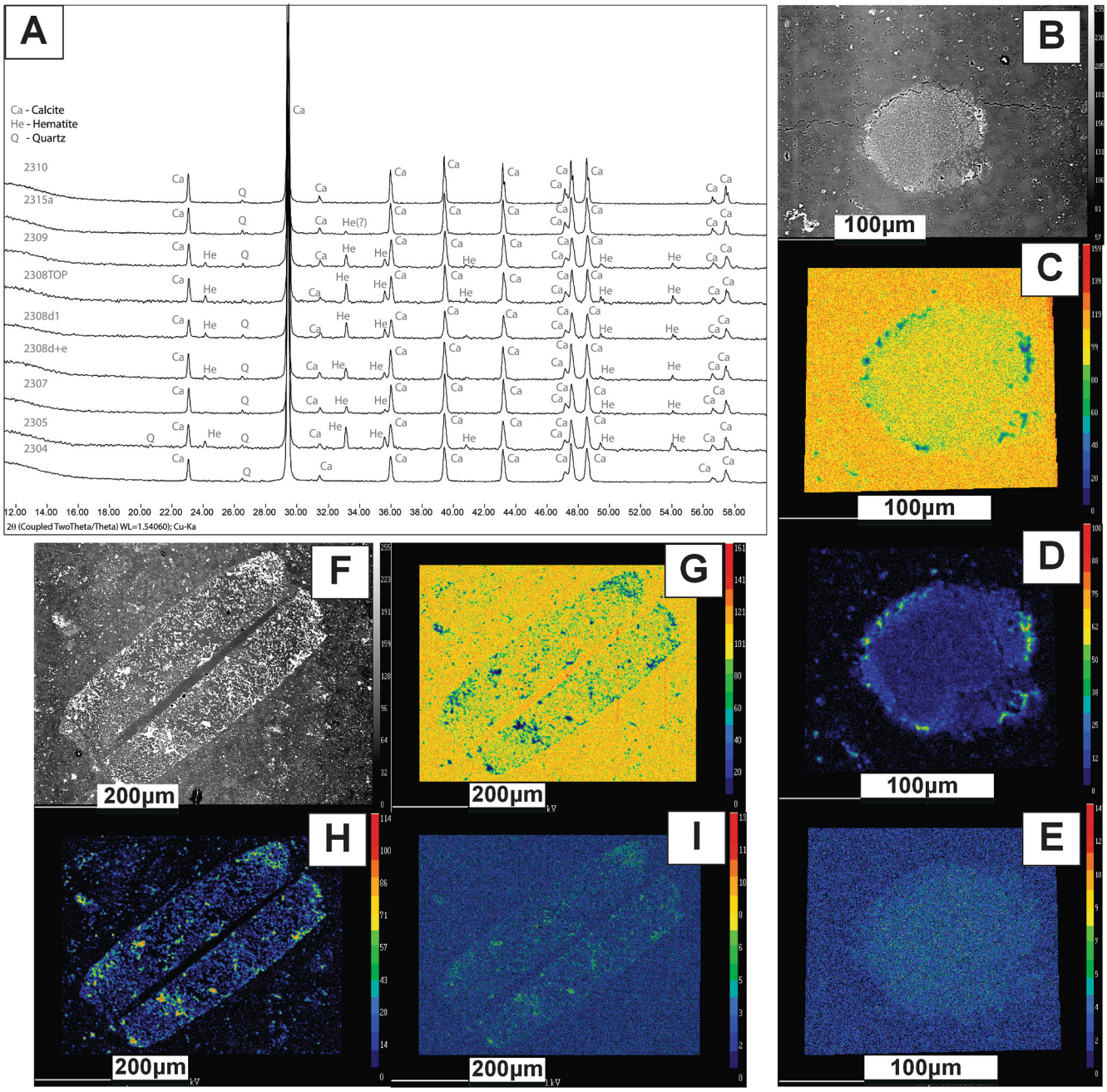

Fig. 13. (A) Stacked RX spectra for selected samples. All samples have a poor mineralogy, dominated by a calcite phase. (B) BSE image and EDS distribution maps for Ca (C), Fe (D) and Mn (E) in a burrow section. (F) BSE image and EDS distribution maps for Ca (G), Fe (H) and Mn (I) in a microcoprolite, here in a longitudinal section.

have elevated Mn concentrations while others are completely lacking (Fig. 13B-I). Silicon (Si) measurements were not conducted, however it is expected that all samples contain variable amounts of Si, as indicated by XRD analysis (Fig. 13A) and microscope screenings (Fig. 6E), which reveal the presence of quartz in nearly all samples.

Rare-earth elements and yttrium: The depletion/enrichment of light rare-earth elements (LREE) relative to heavy rare-earth elements (HREE) was calculated as $[Nd]_N/[Yb]_N$, due to the positive lanthanum (La) anomaly and highly variable negative cerium (Ce) spikes observed in shallow marine waters. The gadolinium (Gd) anomaly was calculated as $[Gd]_N/Gd^*$ where $Gd^* = 0.33[Sm]_N + 0.67[Tb]_N$ (e.g. Nothdruft et al., 2004). The anomalies for La and Ce were calculated using the method proposed by Bau and Dulski (1996), which was further modified by Webb and Kamber (2000). This method allows the assessment of La anomaly by comparing Ce anomaly ($[Ce]_N/Ce^*$ where $Ce^* = 0.5[La]_N + 0.5[Pr]_N$) and Pr anomaly ($[Pr]_N/Pr^*$ where $Pr^* = 0.5[Ce]_N + 0.5[Nd]_N$) through a bivariate plot of $[Pr]_N/Pr^*$ vs $[Ce]_N/Ce^*$ (Fig. 14A).

All samples align within the region characterized by negative Ce anomaly and positive La anomaly on the graph, illustrating a continuous diminishing trend from strong seawater-like Ce and La anomalies to a seawater-like absence of La anomaly (Fig. 14). The La anomaly typically exhibits negative values alongside Ce anomaly values ranging from 0.1 to 0.99, while the Pr anomaly remains exclusively on the positive side, with values ranging from 1.07 to 1.62. The Y/Ho ratio, which serves as a proxy for seawater chemistry, and can therefore be utilized to trace terrigenous input into carbonate sediments (e.g. Bau, 1996; Nozaki et al., 1997), varies from subchondritic to superchondritic values, displaying negative to positive spikes (Table 3, Fig. 14B, Fig. 15).

Table 2
Major element composition (in wt%) of samples from the Leurdeasa Hill section.

Sample code	Na_2O	MgO	Al_2O_3	P_2O_5	K_2O	CaO	TiO_2	MnO	Fe_2O_3
2304	0.0131	0.4873	0.1436	0.0135	0.1643	59.4342	0.0126	0.3174	0.5517
2305	0.0438	0.2938	0.0674	0.0279	0.0582	26.1299	0.0001	0.3056	6.0984
2307	0.0074	0.3128	0.0232	0.0135	0.0046	41.0624	−0.0016	0.4094	1.8008
2308d	0.0189	0.4151	0.0581	0.0420	0.0931	48.2620	0.0001	1.3271	4.0484
2308d1	0.0232	0.4662	0.0340	0.0569	0.0430	49.1407	−0.0008	3.9733	8.0775
2308d2	0.0116	0.4396	0.0526	0.0034	0.0535	48.3889	0.0010	3.4649	2.0521
2308E	0.0073	0.3872	0.0551	0.0506	0.0320	42.3059	0.0030	1.9225	4.5330
2308top	0.0504	0.5704	0.0441	0.0395	0.0728	52.7873	−0.0008	1.3880	6.0672
2309	0.0104	0.4661	0.0643	0.0232	0.0371	49.6109	−0.0008	5.7034	6.2602
2310	0.0330	0.5474	0.8827	0.0345	0.6419	53.5156	0.0370	0.3040	0.6968
2311	0.0241	0.2711	0.0052	−0.0016	0.0540	46.7173	−0.0010	0.0457	0.1838
2315a	0.0146	0.4767	0.4320	0.0002	0.2951	54.9592	0.0175	0.5025	0.5532
2315b	0.0099	0.4227	0.0416	0.0430	0.1074	54.2930	0.0045	7.6789	3.7398

Table 3
Trace elements compositions (ppm) of Upper Triassic carbonate samples from the Leurdeasa Hill section.

Sample code / Element	2304	2305	2307	2308d	2308d1	2308d2	2308E	2308top	2309	2310	2311	2315a	2315b
Sc	7.54	0.62	0.57	2.85	1.69	2.29	2.99	1.11	1.56	2.11	0.23	3.34	2.06
V	30.39	264.92	68.21	153.76	393.09	83.19	158.62	266.62	149.42	36.4	1.86	57.7	85.21
Cr	11.53	1.93	3.41	12.46	6.17	3.78	14.17	5.59	6	4.64	1.12	5.51	4.38
Co	1.63	3.49	2.35	3.21	22.48	35.84	3.9	3.84	31.88	3.58	0.56	14.88	34.19
Ni	25.97	22.36	17.34	24.76	24.88	25.37	22.98	29.8	44.15	59.48	17.56	33.51	25.86
Cu	4.74	6.01	6.05	5.34	2.16	5.19	6.55	4.56	3.75	5.93	1.57	12.12	4.5
Zn	158.09	131.71	21.61	68.38	35.83	21.13	567.84	82.54	58.54	48.78	32.5	35.55	29.41
Ga	0.19	0.27	0.12	0.12	0.16	0.22	0.14	0.12	0.15	0.54	0.02	0.37	0.17
Ge	0.09	1.99	0.29	0.56	1.01	0.34	0.56	0.71	0.75	0.09	0.03	0.1	0.49
Rb	16.94	8.39	3.81	5.84	2.32	7.3	4.42	3.06	3.62	379.25	0.89	60.15	4.51
Sr	299.86	214.19	273	336.4	297.08	363.11	302.54	324.73	285.59	206.89	246.25	300.88	308.07
Y	17.95	1.36	0.67	1.78	10.14	5.77	2.9	4.66	6.74	2.07	0.98	6.19	5.53
Zr	0.65	0.71	4.46	10.63	4.54	2.94	7.56	7.15	9.92	2.03	0.35	4.05	11.07
Nb	0.59	0.21	0.04	0.46	0.29	0.25	0.54	0.3	0.37	0.35	0.01	0.29	0.3
Mo	−0.02	0.47	0.06	0.04	0.19	0.08	0.11	0.21	0.13	−0.08	0.02	−0.05	0.06
Ag	0.02	0	0.01	0.01	0.01	0.03	0.04	0.04	0.09	0.26	0.04	0.01	0.31
Cd	0.11	0.09	0.09	0.08	0.07	0.09	0.09	0.09	0.11	0.19	0.06	0.11	0.21
Sn	0.22	0.14	0.01	0.01	0.04	0.04	1521.85	0.02	0.02	0.49	0.41	0.24	0.03
Sb	0.18	1	0.3	0.35	0.92	0.36	0.76	1.19	0.33	0.26	0.02	0.28	0.44
Cs	2.13	1.27	0.54	0.89	0.44	1.08	0.79	0.71	0.64	11.91	0.22	6.12	0.62
Ba	4.61	3.12	2.68	4.66	10.84	19.62	6.71	4.45	8.35	14.95	1.58	9.01	18.5
La	55.27	4.29	2.35	4.06	5.71	6.3	5.3	3.53	5.77	7.02	1.26	9.5	8.26
Ce	13.52	5.78	2.51	4.93	5.31	6.47	5.72	5.17	10.12	11.71	1.13	10.89	15.86
Pr	3.28	0.77	0.4	0.8	1.18	1.21	1.04	0.66	1.15	1.51	0.19	1.87	1.61
Nd	9.7	2.3	1.16	2.37	3.55	3.59	3.12	2.01	3.46	4.42	0.56	5.47	4.72
Sm	1.82	0.39	0.2	0.43	0.66	0.66	0.57	0.36	0.63	0.74	0.09	0.94	0.85
Eu	0.41	0.1	0.05	0.11	0.17	0.18	0.14	0.09	0.16	0.16	0.02	0.21	0.22
Gd	1.99	0.49	0.23	0.51	0.82	0.82	0.7	0.44	0.77	0.78	0.12	1.07	1.01
Tb	0.32	0.08	0.04	0.09	0.14	0.15	0.13	0.08	0.13	0.12	0.02	0.18	0.18
Dy	1.9	0.49	0.23	0.6	0.93	1	0.86	0.52	0.87	0.7	0.15	1.1	1.13
Ho	0.39	0.1	0.05	0.13	0.2	0.23	0.2	0.12	0.19	0.15	0.04	0.24	0.25
Er	1.05	0.28	0.15	0.4	0.59	0.68	0.61	0.35	0.56	0.4	0.12	0.67	0.7
Tm	0.14	0.04	0.02	0.07	0.09	0.1	0.1	0.05	0.08	0.06	0.02	0.1	0.11
Yb	0.92	0.24	0.14	0.47	0.59	0.68	0.67	0.36	0.53	0.36	0.11	0.62	0.7
Lu	0.13	0.03	0.02	0.07	0.09	0.1	0.11	0.05	0.08	0.05	0.02	0.09	0.1
Hf	0.07	0.02	0.07	0.22	0.07	0.07	0.26	0.12	0.17	0.18	0.03	0.14	0.21
Ta	0.09	0.05	0.01	0.01	0.01	0.01	0.02	0.01	0.02	0.09	0.08	0.06	0.02
W	0.18	1.64	0.59	0.46	0.62	0.31	0.62	0.84	0.89	0.24	0.09	0.14	0.45
Pb	0.89	1.19	1.17	2.49	4.46	10.67	323.42	3.03	2.09	0.96	0.27	1.57	2.28
Th	2.75	0.03	0.04	0.31	0.17	0.26	0.47	0.08	0.15	2.01	0.04	1.39	0.59
U	0.1	0.22	0.11	0.26	0.32	0.16	0.34	0.31	0.39	0.16	0.08	0.16	0.27
SREE	90.84	15.38	7.55	15.04	20.03	22.17	19.27	13.79	24.5	28.18	3.85	32.95	35.7
Ce/Ce*	0.185	0.725	0.588	0.626	0.469	0.536	0.558	0.774	0.900	0.826	0.518	0.592	0.996
Pr/Pr*	1.561	1.201	1.329	1.325	1.495	1.408	1.383	1.164	1.101	1.193	1.350	1.369	1.046

Among the 27 analyzed trace elements (Table 3), vanadium (V) and zinc (Zn) are present in concentrations that exceed average values. Nickel (Ni) shows only slight enrichment compared to marine carbonates (Veizer, 1983), while zirconium (Zr), titanium (Ti), and barium (Ba) display relatively low concentrations (Fig. 15A). The concentrations of V and Zn vary significantly among samples, ranging from low to very high, whereas Ni remains relatively constant, within the range observed in the continental crust (Fig. 15A).

Strontium (Sr) concentrations are limited between 206 ppm and 363 ppm across all samples, appearing moderately low compared to 601 ppm average composition of carbonates (Veizer, 1983; Veizer et al., 1999), although they fall within the range typical of Triassic carbonates (Steuber and Veizer, 2002).

Total REE content among samples varies significantly, with the

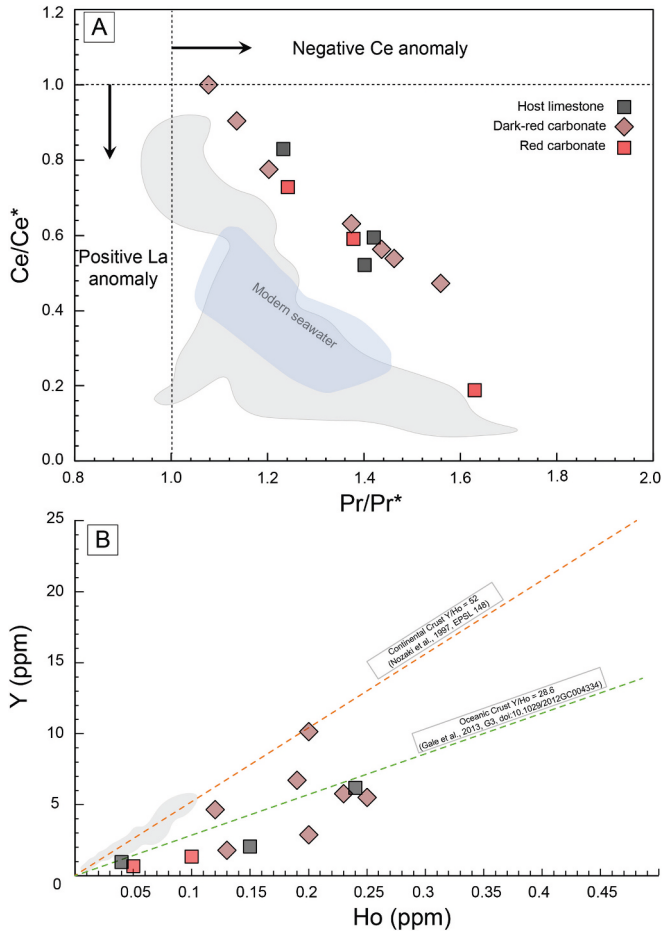

Fig. 14. (A) La - Ce Anomaly: La vs Ce anomalies evaluated trough $(Pr/Pr^*)_N$ vs $(Ce/Ce^*)_N$ plot, using procedure of Bau and Dulski (1996) modified by Webb and Kamber (2000) and Kamber and Webb (2001). Shaded field of modern seawater is from Nothdruft et al., 2004. All samples plot as a continuous trend, within negative Ce anomaly/positive La anomaly field, above the modern sweater range. (B) Plot of Y vs Ho content in host limestone and red and dark red carbonates. Lines of constant Y/Ho ratios corresponding to Continental Crust values (Y/Ho = 52) and to Oceanic crust values (Y/Ho = 28.6) respectively, are from Nozaki et al., 1997 (continental crust) and Gale et al., 2013 (Oceanic Crust). The grey – shaded fields represent the data distribution from Upper Triassic–Lower Jurassic carbonate sediments of the Northern Calcareous Alps (Kiel et al., 2021). Note the more pronounced and broader distribution of Ce and La anomalies (A) as well as the consistent alignment of Y/Ho ratios (B) along the continental crust reference line. (For interpretation of the references to colour in this figure legend, the reader is referred to the web version of this article.)

lowest values recorded at 3.85 ppm for sample 2311 (host limestone, Table 3, Fig. 15B) and reaching 7.55 ppm for sample 2307 (red carbonate infill), peaking at 90.8 ppm for sample 2304 (also red carbonate infill) (Fig. 15). Nevertheless, the majority of the samples show relatively modest values between 15 ppm and 35 ppm. Red and dark red carbonates exhibit LREE depletion, relative to HREE, with $[Nd]_N/[Yb]_N$ ratio of 0.39 to 0.88, averaging 0.57, while the host limestone presents an average ratio of 0.73 ppm. The REE + Y patterns, generally reflect seawater distribution (e.g. Kawabe et al., 1991; Webb and Kamber, 2000), with the exception of sample 2310 (host limestone, $[Nd]_N/[Yb]_N$ = 1.02), which demonstrates modest LREE enrichment, and samples 2304 and 2305 (red carbonate infill, with $[Nd]_N/[Yb]_N$ ratios of 0.88 and 0.80 respectively) that show mild LREE depletion. Eu anomalies are calculated using $Eu/Eu^* = Eu_{SN}/(0.66Sm_{SN} + 0.33Tb_{SN})$ and displayed positive values varying from 1.03 to 1.15, having an average of 1.10 ppm.

4.4.3. Carbon and oxygen stable isotopes

Analyses of stable carbon and oxygen isotopes composition were conducted on 52 diverse carbonate samples including host limestone, red carbonates, dark red carbonates, cements, along with three samples of brachiopod shells (Table 4). The values of $\delta^{13}C_{VPDB}$ and $\delta^{18}O_{VPDB}$ from the host limestone (17 samples) were plotted as a continuous trendline (Fig. 16), alongside the lithological log, serving as a reference for the evolution of the studied sequence. Samples from the red and dark red carbonates were plotted as individual points within the same graph. The $\delta^{18}O_{VPDB}$ values were further utilized for temperature calculations, employing the classic paleotemperature equation of Epstein et al. (1953), modified for the delta values of calcite and water relative to PDB and SMOW scales respectively (Sharp, 2017). Temperature estimates were calculated assuming a $\delta^{18}O_{SMOW}$ value of 0‰ for seawater, with envelopes of ±1‰ and ± 1.5‰, and subsequently plotted following the same procedure as for $\delta^{13}C_{VPDB}$ and $\delta^{18}O_{VPDB}$ values (Fig. 16).

The carbon isotopic composition of the host limestone exhibits positive $\delta^{13}C_{VPDB}$ values, between +2.86‰ and + 4.40‰. The red carbonates (7 samples) display positive $\delta^{13}C_{VPDB}$ values between +2.94‰ and + 4.00‰, while the dark red carbonates (14 samples) present a narrower range of +3.07‰ to +3.69‰. The $\delta^{13}C_{VPDB}$ values for carbonate cements (11 samples) range from +2.99‰ to +3.76‰. Radiaxial fibrous cements exhibit $\delta^{13}C$ values from +2.99 to +3.43‰, whereas late diagenetic cements have $\delta^{13}C$ values between +3.17 and + 3.61‰. Brachiopod shell samples record $\delta\ ^{13}C_{VPDB}$ values of +2.47‰, +3.37‰ and + 3.12‰ (Fig. 17).

The host limestone exhibits negative $\delta^{18}O_{VPDB}$ values, ranging from −2.13‰ to −0.64‰. Comparable values are observed in red carbonates (−2.53‰ to −0.78‰), dark red carbonates (−2.04‰ to −0.80‰) and cements (−2.64‰ to −0.72‰); however, both red carbonate and cement samples appear to be shifted to lower $\delta^{18}O$ values. Brachiopod samples record $\delta^{18}O$ values of −0.80‰, −0.83‰ and − 0.94‰ (Fig. 17).

5. Discussion and interpretation

5.1. Biostratigraphy of the studied section

5.1.1. The host limestone

The conodont assemblage extracted from the host limestone indicates early Carnian age. The species *Budurovignathis mungoensis* is well documented in the Tethys realm in strata spanning the upper Ladinian to the lower Carnian (Kozur, 1980; Kovács and Kozur, 1980; Krystyn, 1980; Kolar-Jurkovšek, 1991). The species *Neocavitela tatrica* has been described from the Tatra Mountains, Poland (Zawidzka, 1972) and it ranges from the Longobardian to the Cordevolian (Kovács and Kozur, 1980), and also into the Julian (Chen et al., 2015), respectively. Numerous studies have shown that the species *Quadralella polygnathiformis* is very common in the Tethys realm. This long-ranging species appears throughout the entire Carnian, except for its uppermost part (Kolar-Jurkovšek and Jurkovšek, 2019). *Quadralella* cf. *acuminata* has been reported from the Ladinian-Carnian boundary interval in British Columbia where it marks the *acuminatus* Zone and it also occurs in the *intermedius* Zone (Orchard, 2007). The *Quadralella* sp. A specimens share certain common features with *Q. lobata* Orchard, 2013, *Paragondolella willistonensis* Orchard, 2007 as well as to the younger *P. praelindae*. Notably, species of *Q. lobata* and *P. willistonensis* have been reported from the Ladinian-Carnian boundary interval in British Columbia, where they are associated with *B. mungoensis* (Orchard, 2007). The species *P. praelindae* was first described from the lower Tuvalian strata of Silicka Brezova (Kozur, 2003). An early Carnian age of the sample 2310 is inferred based on the co-occurrence of *B. mungoensis* and *Q. polygnathiformis*. The latter species has also been documented from Romania, particularly in the Muchea Verde and Cilic Valley sections of North Dobrogea, as investigated by Mirăuţă and Gheorghian (1975). It is noteworthy here that Paragondolellinae from sample 2310 shares certain similarities with specimens from North Dobrogea. All

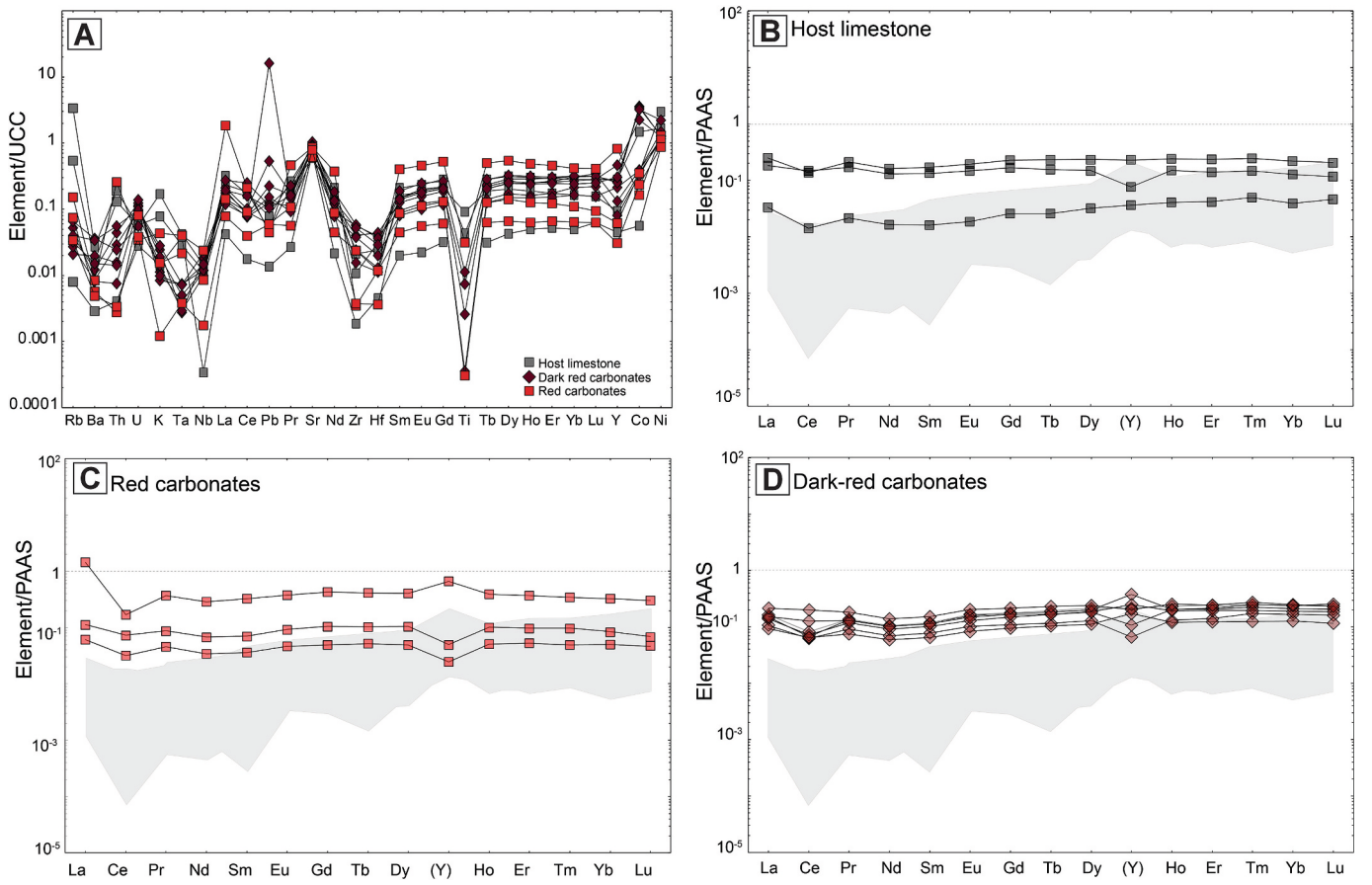

Fig. 15. (A) Spidergram of trace element distributions for samples analyzed. Element concentrations are normalized to Upper Continental Crust (Taylor and McLennan, 1985). Shale (PAAS) normalized REE + Y distribution patterns for the host limestone (B), red carbonates (C) and dark red carbonates (D). Note that the host limestone samples lack the positive Y anomaly and have a rather flat or negative anomaly. REE and Y concentrations are normalized to Post Archaean Australian Shale (PAAS), McLennan, 1989. The grey – shaded fields represent the REE(Y) distribution from Upper Triassic–Lower Jurassic carbonate sediments of the Northern Calcareous Alps (Kiel et al., 2021). (For interpretation of the references to colour in this figure legend, the reader is referred to the web version of this article.)

illustrated specimens from the Carnian strata in the North Dobrogea region are identified as *Q. polygnathiformis*, although they display different morphology. The specimens from the Cilic Valley appear to match the description of *Q. polygnathiformis* (Mirăuţă and Gheorghian, 1975; Pl. 6, Figs. 3–4; Pl. 7, Fig. 4), whereas the other illustrated specimens show pronounced constriction of the platform, indicating that the faunas warrant further revision.

Considering that the host limestone of the studied section consists of lithoclast rudstone with poorly sorted angular to subangular clasts of reef-derived carbonates intermixed with angular clasts of pelagic carbonates and the conodont assemblage extracted from these limestones indicates an early Carnian age, the studied section can be attributed to Wetterstein-type limestone (cf. Lein et al., 2012; Gawlick and Missoni, 2021; Mrdak et al., 2023).

5.1.2. *The infilling of the neptunian dike and sill*

Considering the general range of the brachiopod *Halorella* (Fischer, 1964; Ager, 1965; Ager et al., 1972; Pearson, 1967; Siblík and Bryda, 2005; Siblík, 1988; Sandy, 2010; Peckmann et al., 2011), we infer that the studied neptunian dike and sill network along with their iron-rich carbonate infilling, dates to the late Norian-early Rhaetian. Moreover, the benthic foraminifera *Trochosiphonia josephi* identified alongside the *Halorella* assemblage within the neptunian sill, serves as a potential Norian marker. *Trochosiphonia josephi* is recognized as a Norian marker and has been found in the Norian of Austria, North America, and far-east Russia (Rigaud et al., 2015).

5.2. *The origin of the neptunian dike and sill and their iron-rich carbonate sedimentary infilling*

The formation of the neptunian dike and sill is likely related to the *syn*-sedimentary extensional tectonic events that affected the rim of the Wetterstein Carbonate Platforms, transitional into the proximal basin areas. By the end of the Triassic period, these events caused the drowning of the carbonate platforms along the northern margin of the Neo-Tethys (Lein, 1987; Haas et al., 1995; Gawlick, 2000; Krystyn et al., 2009; Gawlick, in Kovács et al., 2011; Richoz and Krystyn, 2015). The first generation of fractures is associated with the formation of the neptunian dike and sill. These fractures, characterized by sharp boundaries, are preserved between the fissure-filling material and the host rock and contain angular to subangular limestone clasts that have collapsed from the walls of the neptunian dike, indicating a tectonic origin. The second generation of fractures, ranging from millimeters to centimeters in width, intersects the first generation, and exhibits wavy and undulating boundaries along with thin peripheral calcite tapestry (e.g. isopachous fibrous cements on the walls). These features were very likely caused by submarine dissolution and erosion, suggesting a temporal gap between the opening of the fissure and their infilling (Flügel, 2010).

Evidence of successive pulses of polyphase syn-sedimentary movements during the infilling of the neptunian dike and sill with iron-rich carbonates is documented by: thin fractures that disrupt the lamination of previously formed carbonates (Fig. 11A, B); disruptions of the isopachous fibrous calcite (IFC) seams (Fig. 11C); and different

Table 4
Carbon and oxygen isotopic composition of Triassic carbonate samples from the Leurdeasa Hill section.

Analysis# (Sample ID)	$\delta^{13}C_{V\text{-}PDB}$ (‰)	$\delta^{18}O_{V\text{-}PDB}$ (‰)	Sampling detail	Rock type
1 (2554)	+3.70	−1.11	Host rock: limestone with small cavities filled with red sediment; beneath *Halorella* sill	Host limestone
2 (2551)	+4.06	−0.85	Host rock (base of the profile): limestone with small cavities filled with red sediment; beneath	Host limestone
3 (2550)	+3.77	−1.02	*Halorella* sill	Host limestone
4 (2562)	+3.92	−0.74	Host rock: limestone clast with crinoid remnants from red sedimentary breccia	Host limestone
5 (2557)	+3.27	−1.05	Host rock: limestone above the *Halorella* sill	Host limestone
6 (2311)	+3.85	−0.64	Host rock: limestone above the `*Halorella* sill	Host limestone
7 (2560)	+3.29	−1.04		Host limestone
8 (2558)	+2.92	−1.57		Host limestone
9 (2559)	+3.19	−0.98		Host limestone
10 (2555)	+3.62	−1.70	Host rock: limestone with small cavities filled with red sediment; beneath *Halorella* sill	Host limestone
11 (2304–1)	+3.51	−2.04	Host rock: limestone clast from the red sedimentary infill of the neptunian dike	Host limestone
12 (2304–2)	+3.40	−2.15	Red sediment filled fissures cross-cutting the host rock	Red carbonates
13 (2556–1)	+3.54	−1.36	Host rock: limestone at the base of the neptunian dike	Host limestone
14 (2556–2)	+2.94	−2.52	Red carbonate sediment at neptunian dike base	Red carbonates
15 (2553–1)	+4.04	−0.87	Host rock (base of the profile): limestone with small cavities filled with red sediment	Host limestone
16 (2553–2)	+3.45	−2.53	Red sediment filled fissures cross-cutting the host rock	Red carbonates
17 (2553–3)	+3.17	−2.64	Yellowish cement from cavity walls in the host rock	Radiaxial cement
18 (2553–4)	+3.24	−2.42		Radiaxial cement
19 (1/10 Ma)	+4.40	−0.77	Host rock: limestone	Host limestone
20 (1/10 Mb)	+4.00	−0.78	Red sediment filled fissure cross-cutting the host rock in the previous sample	Red carbonates
21 (2305–1)	+3.76	−0.91	Radiaxial cement developed in the dike's red sediment	Radiaxial cement
22 (2305–2)	+3.69	−1.52	neptunian dike's red sediment	Red carbonates
23 (2305-A)	+2.86	−2.13	Host rock: limestone clast embedded in the dike red sediment	Host limestone
24 (2308 T2)	+2.99	−0.72	Cement developed within dark-red sediment with *Halorella*; in thin section the cement is grown around microcoprolites	Radiaxial cements
25 (2308 T2)	+2.96	−1.06	From sample 25 to 29 sampling was done on successive laminae from dark-red sediment of *Halorella* sill	Dark red to mauve carbonates in neptunian sill
26 (2308 T2)	+3.18	−0.73		Dark red to mauve carbonates in neptunian sill
27 (2308 T2)	+3.12	−0.80		Dark red to mauve carbonates in neptunian sill
28 (2308 T2)	+3.21	−0.80		Dark red to mauve carbonates in neptunian sill
29 (2308 T2)	+3.29	−1.09		Dark red to mauve carbonates in neptunian sill
30 (2309(a))	+3.35	−0.83	Dark-red sediment from neptunian sill top (with *Frutexites*)	Dark red to mauve carbonates in neptunian sill
31 (2309(a))	+3.43	−0.73	Cement at the base of previous sample: Dark red sediment from sill top (with *Frutexites*)	Radiaxial cements
32 (2308 base −1)	+3.08	−1.11	Dark-red sediment at the base of *Halorella* sill	Dark red to mauve carbonates in neptunian sill
33 (2308–2)	+3.07	−2.04	Dark-red sediment	Dark red to mauve carbonates in neptunian sill
34 (2308–3)	+3.53	−0.94	Dark-red fine sediment toward the top of the *Halorella* sill	Dark red to mauve carbonates in neptunian sill
35 (2308–3)	+3.54	−0.80	Dark-red carbonates with microcoprolites, toward the top of the sill	Dark red to mauve carbonates in neptunian sill
36 (2308 base −1)	+3.12	−0.94	*Halorella* shell at the base of the sill	*Halorella* shell
37 (2308–2)	+3.37	−0.80	*Halorella* shell and cement (?)	*Halorella* shell
38 (2308–3)	+2.47	−0.83	*Halorella* shell at the top of the sill	*Halorella* shell
39 (2308–3)	+3.15	−1.05	Cement of *Halorella* dark-red sediment, toward the top of the sill	Radiaxial cement
40 (2308–3)	+3.36	−0.81		Radiaxial cement
41 (2308–3)	+3.40	−1.67	Cement of *Halorella* dark-red sediment, toward the top of the sill	Late diagenetic cements
42 (2308–3)	+3.61	−1.17		Late diagenetic cements
43 (2308–3	+3.69	−1.31	Dark red sediment from the top of the sill	Dark red to mauve carbonates in neptunian sill
44 (2308–3)	+3.18	−1.21	Pinkish carbonate fill toward the top of the sill	
53 (2307)	+3.97	−1.10	Red wackestone-packstone with microcoprolites and bioturbation (on the top of the neptunian dike)	Carbonate matrix with medium iron content
54 (base of 2308)	+3.31	−1.20	Dark-red limestone with brachiopods (*Halorella*)	
55 (2309)	+3.03	−1.15	Sampled from 2309 with *Halorella* (From a 5–7 mm thick sindepositional cement fringe	Carbonate cement
55 (doubled)	+3.08	−1.13	toward the top of the sample)	Carbonate cement
56 (2310)	+3.14	−1.43	Host rock above the *Halorella* sill	Host limestone
57 (2309)	+3.49	−1.20	Cement from sample 2309 top	Carbonate cement
74 (2308d)	+3.08	−0.99	Dark red *Halorella* limestone sampled from 2308d (median part of sample 2308)	Carbonate matrix with medium iron content
75 (2306)	+3.96	−1.08	Red limestone rich in microcoprolites that fill the neptunian dike, beneath *Halorella* sill (near 2306 host limestone clast)	Red carbonate with micro-coprolites and burrows

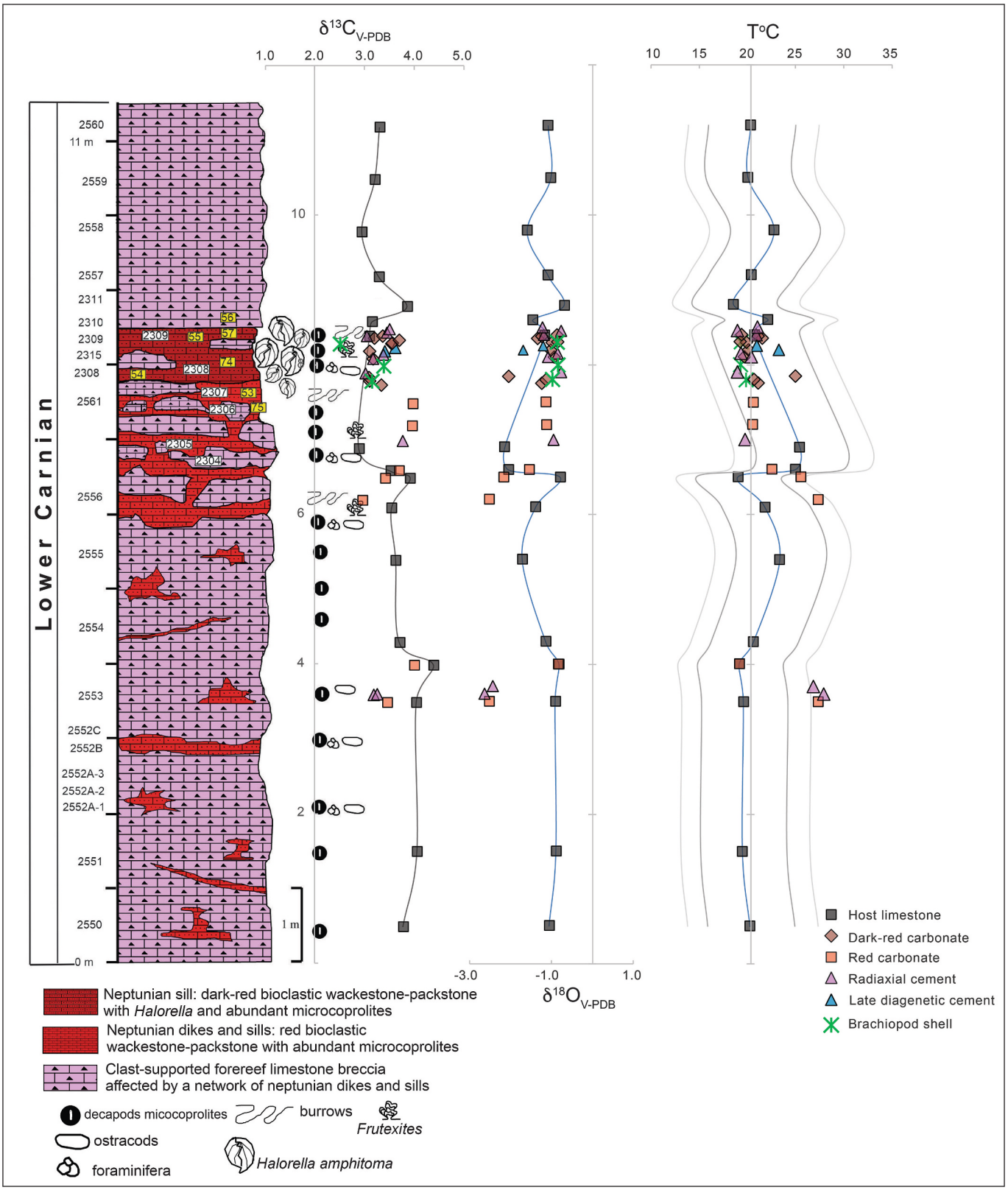

Fig. 16. Lithostratigraphic column of the studied section. $\delta^{13}C$, $\delta^{18}O$, and estimated paleotemperature trends for the host limestone represented to the right respectively. Both $\delta^{13}C$ and $\delta^{18}O$ curves shows several episodic shifts to higher values, most likely in response to tectonic forcing. $\delta^{13}C$ and $\delta^{18}O$ values of samples from infill material are represented as individual points along the respective trends of the host rock. Grey curves accompanying paleotemperature trend represent temperature envelopes for $\delta^{18}O_{SMOW}$ values of seawater of ±1 and ± 1.5. See text for details. (For interpretation of the references to color in this figure legend, the reader is referred to the web version of this article.)

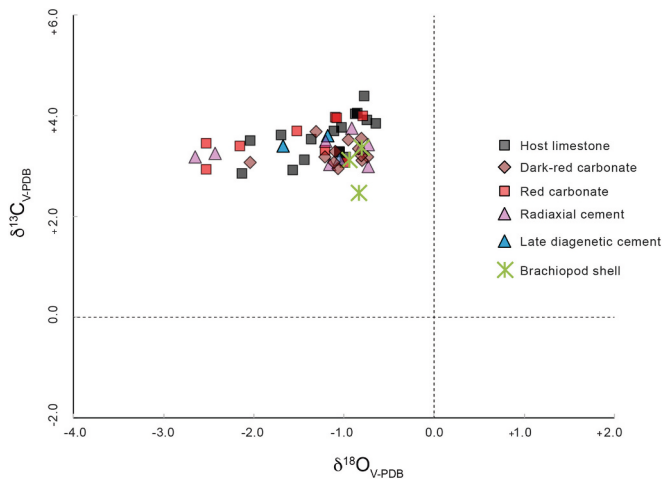

Fig. 17. Oxygen carbon-crossplot: $\delta^{18}O$ vs $\delta^{13}C$ crossplot of all samples, including brachiopod shell. A visible continuous trend toward more negative $\delta^{18}O$ values can be observed, very likely due to diagenetic alteration at low water/rock ratios.

orientation of the geopetal fabrics inside brachiopod shells and within the shelter cavities formed in the surrounding sediment (Fig. 11D). Alternations of thin rims of calcite cements and sediment infill (Fig. 11A-D) also indicate repeated rupture and polyphase filling of the sill (Wiedenmayer, 1963).

The non-luminescent RFC that developed around the voids and cavities, growing directly on the inner parts and outer surfaces of the brachiopod shells represents typical marine cement, standing in contrast with non-marine cements, which exhibit compositional zoning due to variations in Mn and Fe content (Hemming et al., 1989). The presence of saddle dolomite (SD) inclusions within RFC suggests that these RFC originally formed as high-magnesian calcite (HMC, Lohmann and Meyers, 1977; Kendall, 1985) subsequently stabilized into low-Mg calcite (LMC) during diagenesis. SD is therefore an indicator of shallow marine burial diagenesis (Searl, 1989). The RFC indicates that the marine cementation occurred in intertidal settings extending down to upper bathyal paleo-water depths (Kendall, 1985). However, the RFC analyzed in the studied sections is interpreted as indicative of a shallow marine phreatic environment, based on petrographic and CL observations.

Scalenohedral calcite generally postdates the RFC and is characterized by sharp crystals that point to different growth directions and is recognized in a wide variety of depositional environments, from the meteoric to shallow burial to marine or hydrothermal settings (Flügel, 2010). In our samples, the zoned luminescence and the association with blocky calcite and saddle dolomites suggest that the precipitation occurred in a shallow burial environment.

The presence of scalenohedral calcite, blocky calcite, and saddle dolomites, along with minor mechanical compaction and chemical compaction, including dissolution seams or stylolitization, indicates that the studied samples have undergone late-stage diagenesis. In many instances, we noted that dissolution seams frequently occur at the interface between sediment and brachiopod shells or with the cement that developed on the brachiopod shells (Fig. 9 A, B, D). These seams are recognized by undulating lines highlighted by a concentration of insoluble residue amid partly dissolved or truncated shells. Such dissolution processes arise because of increased pressure and temperature during early compaction and burial of sediments. Dissolution seams commonly occur in sedimentary rocks either due to high clay mineral concentrations (Bathurst, 1991) or to the presence of dolomite crystals along the contact between the fine sediment and coarser grains. Dolomitization is frequently associated with the dissolution processes (Wanless, 1979).

Carbonate sediment contamination: Terrigenous input into carbonate sediments can be traced in several ways, such as through elevated concentrations of specific diagnostic trace elements (e.g. Sc, Zr, Hf, Th, as discussed by Webb and Kamber, 2000), or Al concentration (e.g. Nothdruft et al., 2004) and its correlation with other diagnostic trace elements. Furthermore, "*clean*" marine carbonate sediment typically exhibits seawater-like REE + Y patterns, which are directly inherited from their seawater environment through constant partition coefficients. These patterns are characterized by relatively uniform LREE depletion, negative Ce anomaly and mild La positive anomaly (e.g. De Baar et al., 1991; Bau and Dulski, 1996), along with elevated superchondritic seawater Y/Ho ratios (Bau, 1996; Nozaki et al., 1997).

Trace element compositions reported from comparable settings in the Upper Triassic–Lower Jurassic deposits of the Northern Calcareous Alps (e.g., Kiel et al., 2021) show, however, some differences. In their case, the REE(Y) patterns appear more fractionated (Fig. 15B-D), the Ce anomaly is more pronounced and variable (Fig. 14A), and the Y anomaly is consistently positive (Fig. 14B) with mostly superchondritic Y/Ho ratio, that indicate an open-marine environment.

The europium anomaly (Eu/Eu*), calculated as $[Eu]_N/0.5*([Sm]_N+[Gd]_N)$, is barely present although variable between a slightly negative value of 0.88 and a slightly positive value of 1.1. These values preclude any massive volcanic input, and are potentially likely results from diagenetic alteration of carbonate material (Brand and Veizer, 1980).

Furthermore, the superchondritic Y/Ho ratios point to a possible influence from detrital inputs, particularly siliciclastic components. While the negative Y anomalies are rather uncommon, the presence of positive Y anomalies related to Y/Ho ratios is common in marine seawaters with higher Y anomalies (~40–80), typically associated with open-marine environments and lower Y anomalies (~33–40) found in nearshore or restricted settings. In the studied samples, the Y/Ho ratio aligns closer to those of restricted environments, whereas terrigenous materials consistently show Y/Ho ratios around 28 (Bau et al., 1997; Tostevin et al., 2016).

The studied carbonate samples sourced from host limestone and the red and dark red carbonate sediment infilling the neptunian dike and sill exhibit the following characteristics: (1) low concentration of Sc, Zr, Hf, and Th, (2) elevated concentration of Fe, Mn, Co, Zn and V (relative to background levels), particularly in red and dark-red carbonates and especially in samples containing numerous microcoprolites and *Frutexites*-like microstructures, (3) low concentration of Al and P, (4) predominantly seawater like REE + Y patterns (see Fig. 15), characterized by LREE depletion in all but one sample along with negative Ce anomaly and positive La anomaly (Fig. 14A), and a Gd anomaly, (5) variable Y/Ho ratios, ranging from subchondritic to superchondritic, yet remaining under continental crust value of 52 (Nozaki et al., 1997) (Fig. 14B).

While the low concentrations of Sc, Zr, Hf, and Th, along with the absence of correlation between Zr and Y/Ho, typically suggest the absence of terrigenous input, this does not entirely rule out any terrigenous input. However, the presence of silica, as evidenced by microscopic observations in conjunction with XRD analysis (Fig. 13A), can be attributed to other potential sources (i.e. radiolarian, sponges, etc), other than terrigenous contribution.

REE patterns predominantly reflect seawater-like distribution, and exhibits varying degrees of enrichment, observable also within each group of samples. Notably, the host limestone sample demonstrates the highest variability, with sample 2315a being the most LREE enriched. It was shown (Nothdruft et al., 2004), that mixing with as low as 1–2% terrigenous material can significantly alter REE + Y patterns. Due to relatively high REE content, even a minor terrigenous contribution can attenuate the La and Ce anomaly while reducing LREE to HREE fractionation. Additionally, one important effect is the marked attenuation of the Y spike. In this context, the host limestone samples mark the extremes, illustrating both the least and most affected REE patterns (Fig. 15B).

The red and dark red carbonates composing the infill of the neptunian dike and sill still retain their seawater-like pattern, with the red carbonates showing greater variability (Fig. 15C, D). In addition to terrigenous contribution to the carbonate sediments, the presence of Fe-Mn oxides which incorporate disproportionate and often unpredictable amounts of REE + Y (Bau et al., 1996), may introduce further complication to REE + Y distribution. It is likely that in our case, the Fe-Mn hydrogenetic fluxes might have impacted to some extent on lowering Y/Ho ratios. Fe and Mn (+V) are indeed present in all samples at various concentrations, with higher values noted in samples containing microcoprolites and *Frutexites* microstructures. In fact, all the original microcoprolite material was replaced with carbonates and Fe-Mn (+V) oxides (and scarcely Ca phosphates, Fig. 13B-I). Although hydrogenetic fluxes may account for the elevated concentrations of Fe and Mn (+V) in all samples, they do not solely explain for subchondritic Y/Ho ratios (i.e. negative Y anomaly) evident in certain REE + Y distributions. Furthermore, Y/Ho ratios seem to exhibit apparently cyclic variations, fluctuating between subchondritic and superchondritic values within each sample group, a trend that is particularly pronounced in dark-red carbonates, where we have the highest sample count over a relatively short distance (Fig. 15D). Previous research has suggested that the redox cycling can significantly influence the Y anomaly while having minimal to no impact on the sizes of La and Gd anomalies (Bau et al., 1997). Consequently, it is very likely that the variations in Y/Ho ratios, especially noted in dark-red carbonates, reflect variations in redox conditions. These episodic transitions from oxic to suboxic conditions may have occurred in a setting with intermittent access to oxygenated waters, or that has been temporarily locked out of oxygenated waters. Episodic biotic blooms in such an environment, could lead to substantial oxygen depletion, inducing temporary suboxic conditions until the next recharge with marine oxic water.

The carbon isotopic composition of the host limestone aligns closely to that of modern marine carbonates (e.g. Hudson, 1977; Moore, 2001; Sharp, 2017), exhibiting positive $\delta^{13}C_{VPDB}$ values, between +2.86‰ and + 4.40‰. The host limestone expresses a relatively uniform carbon isotope composition (Fig. 16), with a slight decrease in $\delta^{13}C$ values observed in the lower part of the section. However, several spikes – apparently cyclic – are present, marked by shifts of $\delta^{13}C$ values toward higher values, which disrupt this uniform trend, likely due to tectonic forcing. This cyclic nature of $\delta^{13}C$ distribution is mirrored by the curve defined by $\delta^{18}O$ values, which shows shifts toward higher values, as well as by the paleotemperature evolution line. Notably, these $\delta^{18}O$ spikes are not synchronous with $\delta^{13}C$ shifts, but are deflected slightly upward. Each carbon and oxygen isotopic shift interestingly delineate segments (or domains) characterized by a gradual decrease in carbonate production, coupled with a gradual increase followed by a slow decrease in water paleotemperature.

The most significant increase in temperature (as high as ~26 °C, Fig. 16) aligns with the section corresponding to the highest volume of material infill of the neptunian dike and sill. The carbonate components of the infill sediments of the neptunian dike and sill – comprising red and dark red carbonates, early and late diagenetic cements – does not seem to correlate with the host rock at the infilling level. The $\delta^{13}C$ and $\delta^{18}O$ values consistently fall below the isotopic trend of the host rock in the lower half of the section (between 0 and 6 m) while remaining consistently higher than the host rock isotopic trend in the upper half (meter 6 up to meter 12) of the section (Fig. 16). While $\delta^{13}C$ values show moderate shifts toward lower values in the lower half of the section, the $\delta^{18}O$ isotope composition seems to be significantly affected (Fig. 16), possibly due to burial (Nelson and Smith, 1996), or meteoric alteration at low water/rock ratio (e.g. Lohmann, 1988; Sharp, 2017), both of which primarily result in lowering the $\delta^{18}O$ values. Generally, carbon isotopes are less affected by diagenesis compared to oxygen isotopes (e.g. Lohmann, 1988; Frank et al., 1999; Fisher et al., 2005), since oxygen isotopes are more susceptible to diagenesis due to their temperature-dependent fractionation, particularly at low water/rock ratios. In a bivariate plot of $\delta^{13}C$ vs $\delta^{18}O$, our samples fall within the overlapping regions of warm water carbonate sediments, marine cements, and warm water skeletons fields as defined by Nelson and Smith (1996) (Supplementary materials 3).

The estimated water paleotemperature for the host limestone is around 20 °C, with cyclic increases reaching up to 25 °C at most, particularly in the interval between meter 6 and 9 of the Leurdeasa Hill section (Fig. 16). However, these paleotemperatures estimates for the infill material sharply contrast with those of the host rock. The highest values appear to be associated with red carbonate material and radiaxial cements from the neptunian dike, reaching paleotemperatures as high as 28 °C; notably these samples also show significant evidence of diagenesis. The dark-red carbonates from the neptunian sill indicate paleotemperatures around 20 °C. The red/dark red material is obviously diachronous (i.e. younger), since it exhibits C and O isotopic marine signatures distinct from the host rock at the accommodation level, while correlating more closely with the limestone host signatures at higher levels of the section. Tectonic activity likely played a significant part in the evolution of this carbonate sequence. The abrupt, short lived cyclic shifts of $\delta^{13}C$ and $\delta^{18}O$ values (Fig. 16) can be interpreted as episodic bursts of biologic activity and temperature drops during brief episodes of deepening, which were under tectonic control. It is plausible that these tectonic episodes lead to cracking of insufficiently consolidated sediment, thus creating the pathways for subsequent red infills.

5.3. *The paleoecology and paleoenvironmental context of the brachiopod-arthropod-microbial assemblage in the neptunian sill filled with iron-rich carbonates*

5.3.1. *Halorella mass-occurrence within the neptunian sill*

A notable feature of the studied section is the mass-occurrence of *Halorella* brachiopod shells, together with microcoprolites and ostracods, exclusively found in the neptunian sill above the neptunian dike. The divergent orientation of brachiopod shells of various sizes, ranging from juveniles to adults, combined with different orientations of multiple geopetal fabrics and multiple phases of cementation of large shelter cavities, suggest event deposition of a large brachiopod population within the neptunian sill. Good preservation of internal and external skeletal elements, bimodal sorting (i.e. complete shells and shell debris), and the absence of signs of abrasion, bioerosion or encrustation indicate a rapid deposition of the shells within a robust flow of warm water inside of the neptunian sill (Fürsich and Oschmann, 1993; Hornung, 2005). Ninety percent of the *Halorella* shells are partially filled with the same sediment that characterizes the surrounding matrix (iron-rich micropeloidal carbonate) and exhibit sequential nucleation of early radiaxial fibrous calcite, followed by late blocky cements, resulting in geopetal structures. Cement-filled shells with preserved internal structures also indicate rapid burial. Fast sediment infilling of shells prevents disarticulation, brachidium fragmentation and colonization by coelobites (Tomašových et al. (2022). Furthermore, the observed features and the wide range of brachiopod shell sizes in the assemblage indicate short-range transport of, most probably, a neighborhood assemblage.

Numerous *Halorella* shells are articulated and filled with the same internal sediment (iron-rich carbonate mud), and some adult specimens display deformation without breakage (Fig. 12C, D), suggesting aberrant shell forms resulting from shell crowding and limited space. The presence of articulated micrite-filled shells with preserved brachidium support structures (crura) and reduced burrowing could also suggest intervals of reduced taphonomic-activity within the sill, when bioturbation was probably limited (cf. Tomašových et al., 2022).

The studied *Halorella* brachiopod shells show variable outlines, typically transverse-oval but can also appear subpentagonal, or sphaerical. Their external dimensions suggest the presence of a population that includes both juvenile and adult specimens. Considering all these observations, we presume that a large population of *Halorella* brachiopods lived attached to the walls of the neptunian sill and were

subsequently washed inside the sill during the successive flows of warm marine waters from which iron-rich carbonates precipitated. Several large, fragmentary specimens are estimated to measure at least 80 mm in maximum length and 90 to 100 mm in maximum width, suggesting that these brachiopods could reach very large sizes. The significant shell size of several Paleozoic and Mesozoic dimerelloid brachiopods has been interpreted as being associated with cold seeps and chemosynthetic environments [e.g. *Dzieduszyckia* Siemiradzki, 1909, Devonian, Peckmann et al. (2007); *Ibergirhynchia* Gischler et al. (2003), Early Carboniferous; *Halorella*, Late Triassic, Peckmann et al. (2011) and *Sulcirostra* Cooper and Muir-Wood, 1951, Early Jurassic, Peckmann et al. (2013)]. However, recent studies of brachiopod assemblages in cryptic habitats, such as submarine caves in the Mediterranean Sea (Bitner and Gerovasileiou, 2021), are represented by micromorphic species. Recent marine caves (devoid of any influence of hydrocarbon-rich fluids or hydrothermal fluids) represent true hot-spots for brachiopod diversity. Brachiopod abundance either tends to increase toward the internal, dark zones of the submarine caves (living attached especially on ceilings), or their density is variable in close dependance to the depth and topography of the wall caves (Bitner and Gerovasileiou, 2021). The presence of large populations of normal-sized articulated brachiopods (e.g., terebratulids) has also been documented in modern cryptic environments such as rock wall habitats (Witman and Cooper, 1983) and crevice or cavity systems (Noble et al., 1976; Tomašových, 2008). The concentration of brachiopod communities in such "refuges" in modern hard bottom habitats is a consequence of the absence either of strong predation pressure (Harper and Wharton, 2000; Aberhan et al., 2006), or of intense competition for space and food with molluscs and other organisms (Bush et al., 2007; Novack-Gottshall, 2007). By comparing Jurassic, Cretaceous, and Recent (Mediterranean) hardground communities, Noble et al. (1976) suggested a relative constancy in composition, in terms of higher taxonomic groups, since the Mesozoic, with crevice or cavity sub-communities dominated (in varying proportions) by chitons, annelids, brachiopods, and bryozoans. Tomašových (2008) demonstrated that grazing negatively affects both micromorphic and large-sized brachiopods (in shallow and deep subtidal habitats) and suggested that the preference of brachiopod larvae for cryptic habitats may be related to grazing pressure on juveniles during the Mesozoic. A similar situation may have characterized cryptic submarine habitats since the Late Triassic. Harper and Peck (2024) showed that large-sized brachiopods were excluded from habitats with intense predation (e.g., tropical shallow areas), and that this pattern was probably established during the early part of the Mesozoic Marine Revolution and has persisted to the present day. The Recent brachiopod assemblages from submarine cryptic cavities are often found in association with other benthic invertebrates such as serpulid polychaetes, bryozoans, rare sponges, and predators like gastropods and crabs (Bitner and Gerovasileiou, 2021). Additionally, Guido et al. (2016, 2017) described Recent cryptic serpulid-microbialite assemblages containing brachiopods and *Frutexites*-like structures from submarine caves in the Mediterranean.

Halorella belongs to a group of large-sized costate dimerelloid rhynchonellide brachiopods that includes Paleozoic-Mesozoic associations affiliated to cold-seep environments (Sandy, 2010). Examples include *Dzieduszyckia* from the Devonian of Morocco (Peckmann et al., 2007), and *Anarhynchia* Ager, 1968 from the Jurassic of California and Alaska (Sandy, 2010; Sandy in Peckmann et al., 2011; Pálfy et al., 2017). It has been suggested that mass occurrences of dimerelloid rhynchonellides could help identify ancient hydrocarbon seeps (Sandy, 2010). Such occurrences of *Halorella* have been documented in Upper Triassic (Norian) limestones from Oregon, U.S.A. (Peckmann et al., 2011), as well as from Turkey (Kiel et al., 2017). However, petrographic analyses, stable carbon isotope measurements ($\delta^{13}C$: +3.1 to +3.4‰, $n = 6$), and rare earth elements (REE) contents and distribution patterns of samples from Leurdeasa Hill do not support the association of this Romanian occurrence of *Halorella* with methane seepage or hydrothermal fluids. Similarly, Kiel et al. (2021) reported the lack of evidence for the influence of hydrocarbon-rich fluids or hydrothermal fluids for the mass occurrences of *Halorella amphitoma* found in Upper Triassic dikes and fissures in the Dachstein Limestone from the Northern Calcareous Alps. They concluded that *Halorella* was capable of rapidly adapting to dark habitats, relying on small-sized food particles washed into the dikes. The distinctive long, ventrally curving (ensiform or ciliform) crura of *Halorella* (Manceñido et al., 2002; Sulser and Furrer, 2008; Sandy, 2010) have been interpreted as an adaptation of the crura (that hold the lophophore, their feeding apparatus) to their feeding strategy (Kiel et al., 2021) in these probably nutrient-poor cryptic habitats (such as submarine cryptic cavities, neptunian dikes and sills).

However, it is reasonable to infer that successive influxes of water and sediment into the neptunian sill could have produced subsurface productivity maxima where internal waves intercepted the walls of the sill, allowing the development of large populations of brachiopods in such dark, cryptic environments. Nevertheless, according to Zezina (2008), there are Recent rhynchonelliform brachiopods that feed on the products of decomposition of dead plankton. These brachiopods live in the aphotic zone, on the edges of deep shelves, and on the upper parts of the slopes. The same author commented that the main food source of Recent brachiopods consists of suspended organic material, determined by the bacteria present on the suspended particles. McCammon (1969) showed that Recent terebratulidae and rhynchonellide brachiopods can feed on "marine snow", aggregates formed by the adsorption of dissolved organic carbon on their surface.

5.3.2. *Crustacean arthropods likely represented the autochthonous biota*

The abundance of microcoprolites and the numerous burrows of varying dimensions suggest that crustacean arthropods likely formed the primary autochthonous biota in the studied neptunian dike and sill, accompanied by rare benthic foraminifera, ostracods, and microbial mats. The intense burrowing indicates an oxygenated environment. Typically, oxygenated seafloor settings support a benthic infaunal community that includes various burrowing organisms (e.g., arthropods) whose activities are known to significantly affect sediment biogeochemistry (e.g., Rosenberg et al., 2001; Weissberger et al., 2009). Intense burrowing may lead to sediment oxidation, which suppresses microbial growth. Conversely, intervals with low sedimentation and suboxic conditions can result in the decline or even demise of benthic fauna (Wignall and Twitchett, 2002) and promote seabed microbe blooms, commonly expressed as microbial mats (Pruss et al., 2004; Li et al., 2021).

5.3.3. *Frutexites-like microstructures*

Intervals characterized by low or reduced sedimentation rates within the neptunian dike and sill likely experienced suboxic conditions, as suggested by the presence of ferruginous micritic fabric and locally clotted or peloidal microfabrics within the internal sediment. Intervals with limited burrowing and reduced sedimentation favored the local development of *Frutexites*-like microstructures within the sediment. *Frutexites* likely grew in microenvironments within the sediment where redox oscillations are considered common at some depth below the sediment – water interface. Although cryptic microbialites typically lack distinct mesofabrics, they usually display micritic, clotted, or peloidal microfabrics (Riding, 1991). The described microstructures, which exhibit columnar and dendritic to complex multilobate morphologies, may be interpreted as endostromatolites (sensu Monty, 1984) and/or crenulated microstromatolites (sensu Boulvain et al., 2001; Mamet and Préat, 2006), given their thin internal crenulated – convex lamination

and clotted or peloidal microfabrics (Fig. 7B–E), or as *Frutexites*-like microstructures (Type I and Type II sensu Champenois et al., 2024, and references therein). *Frutexites* is a problematic microstructure first described by Maslov (1960) as arborescent, consisting of finely laminated to opaque structures composed of iron and/or manganese oxides and calcite. The processes underlying the formation of *Frutexites* remain under debate, with various proposals invoking abiotic, biotic, or coupled abiotic–biotic processes. *Frutexites*-like microstructures have been reported from marine environments ranging from Proterozoic through Paleozoic to Mesozoic deposits (Champenois et al., 2024, and references therein). Such microstructures have been observed in a variety of ancient marine cavities (Gischler, 1996; Reolid and Molina, 2010; Jakubowicz et al., 2014), within sheet cracks and veins (Cavalazzi et al., 2007), and in the filling of fissures, fractures, and neptunian dikes (Gischler, 1996; Lazăr et al., 2013).

Lower Triassic *Frutexites*-bearing microbialites have been documented by Woods and Baud (2008) and Baud and Richoz (2015) within a pelagic limestone succession (Alwa Formation) deposited on an isolated, drowned carbonate platform in the Oman Mountains. Rodríguez-Martínez et al. (2011) described vertical structures of *Tolypammina gregaria* – *Frutexites* associated with ferromanganese crusts and surfaces in the condensed Carnian Hallstatt Limestone of the Northern Calcareous Alps. *Frutexites* typically develops in aphotic microenvironments, during intervals of very slow sedimentation under dysoxic (Böhm and Brachert, 1993) or dysoxic–anoxic conditions (Mamet and Préat, 2006; Woods and Baud, 2008; Lazăr et al., 2013; Grădinaru et al., 2020). These dark microenvironments are characterized by low water circulation and reduced oxygen levels, conditions that are conducive to *Frutexites* nucleation in submarine cave settings (Guido et al., 2016). Nitrate-reducing microbes can oxidize iron under anoxic conditions (Straub et al., 1996; Benz et al., 1998). In sediments rich in organic matter and characterized by low bottom water oxygen concentration, nitrate reduction can play a dominant role in organic matter decomposition in many marine environments (Canfield et al., 1993). Given that microcoprolites are rich in organic matter at their production (Pryor, 1978), it is reasonable to infer intensive bacterial activity both within the fecal pellets (Rindsberg and Kopaska-Merkel, 2013) and in the adjacent sediment.

In the studied samples containing *Frutexites*-like microstructures, SEM analysis revealed different types of curved filaments, dichotomously branching filaments, as well as microfilaments with ribbon-like stalks and rod-shaped bacilliform structures. These features appear to form a dense network that may represent mineralized remains of extracellular polymeric substances (EPS) (Fig. 8).

5.4. The paleoenvironmental context

The interval between the opening of the neptunian dike and sill and their subsequent sedimentary infill likely occurred shortly after fracture formation, with carbonate sediment infill deposited from successive flows. Initially, the neptunian dike was filled with red carbonate mud. The parallel and irregular laminations of the internal carbonates, together with the orientations of microcoprolites, suggest that these sediments were precipitated from flows characterized by temporarily elevated rates within the fracture system. The flow was not continuous; instead, it was marked by successive influxes of water and sediment, including very fine carbonate grains and dispersed silt-sized siliciclastic grains and clay minerals. This is documented by the presence of successive erosional surfaces and localized dense accumulations of microcoprolites (Fig. 6A, E, C).

The apparent cyclic variation between oxic and suboxic conditions can also account for elevated concentrations of Fe-Mn (+V) and possibly Zn, as well as for the impact on REE + Y fractionation, given that, in addition to terrigenous particulates, organic matter significantly influences the cycling and fractionation of trace elements (e.g. Sholkovitz et al., 1992, 1994; Smrzska et al., 2019). Consequently, microcoprolites could have acted first as cargos and later as repositories for these elements, exhibiting variable behavior linked to fluctuating oxic to suboxic conditions. The presence of moderately negative Ce anomalies together with variation in the Y anomaly suggests an alternation between oxidized phases and poorly oxygenated conditions within the cavity and fracture system - such as neptunian dike and sill environments – over relatively short time intervals.

Geochemical and mineralogical analyses of the red carbonate infill of the neptunian dike and of the neptunian sill containing *Halorella* from the Romanian Carpathians reveal significant quantities of iron oxides associated with elements such as Sr, Zn, Ni, and V. This suggests that these red carbonates formed in a marine environment, over relatively short time intervals and under variable oxic/suboxic conditions, with minor detrital input and hydrogenetic fluxes. Variations of the Y/Ho ratio and the moderately negative Ce anomalies recorded by the dark-red carbonates forming the infill of the neptunian sill indicate recurrent changes in redox conditions. Furthermore, the iron-rich carbonate mud flows were probably periodically enriched in nutrients and oxygen, creating favorable conditions for the development of active populations of crustacean arthropods (the producers of microcoprolites and burrows) and ostracods feeding on organic matter remains, alongside large populations of suspension feeders, including *Halorella* brachiopods which lived attached to the walls of the neptunian sill.

5.5. Paleogeography

The brachiopod *Halorella* is typically considered an indicator of the Late Triassic (Late Carnian-Norian) (e.g., Manceñido et al., 2002) and exhibits a broad paleogeographic distribution during this time-interval with species of the genus distributed around the Tethys and Panthalassa Oceans (Fig. 18). Notable mass-occurrences of *Halorella* have been reported from:

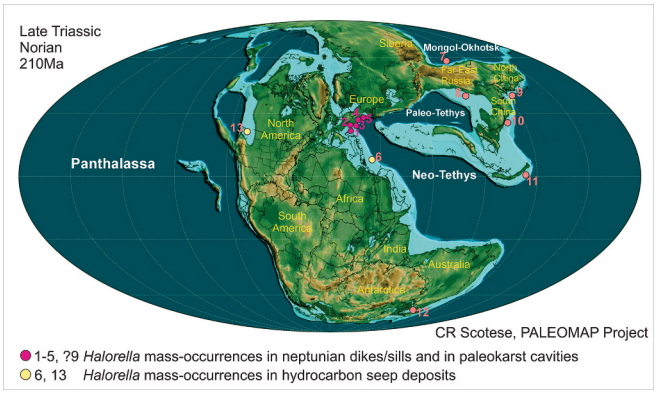

Fig. 18. Paleogeographic distribution of the genus *Halorella* during the Late Triassic, based on Scotese (2014) Paleogeographic Map for Norian: 1–5 Tethys occurrences; 6–11 Panthalassa occurrences; 12 – Arctic occurrence; 1. Slovenia (Julian Alps, neptunian dikes and sills) 2. Austria (Northern Calcareous Alps, neptunian dikes and sills); 3. Hungary (Main Dolomite Formation,?neptunian dikes and sills and Bakony Mountains from supratidal karstic cavities); 4. Slovakia (Silická Brezová, from *Halorella*-bearing fissure-filling); 5. Romania (this study, North Apuseni Mountains, neptunian sill); 6. Turkey (Southern Turkey, Taurus Mountains, hydrocarbon seep); 7. Russia (Pegtymel River, Chukotka); 8. Tajikistan (Dzhilgakochusu reef limestones); 9. China (Zadoi County); 10. China (Ninglang County); 11. Indonesia (East Timor, Aitutu Group); Indonesia (East Timor, mass-occurrence in transitional facies between basin and shallow water carbonate deposits); 12. New Zealand (from argillite-calcareous greywacke and siltstone); 13. Oregon (USA, hydrocarbon seep). Coordinates of *Halorella* occurrences were taken from: Benincasa (2015), Channell et al. (2003), Kiel et al. (2017), Kiel et al. (2021), Jurkovšek and Kolar-Jurkovšek (2021), McClennen et al. (2024), Müller et al. (2026) and the present study. The locations 7, 8, 10, 11, 12 are occurrences of *Halorella*, without detailed information concerning the paleoenvironmental context.

(a) Neptunian dikes and sills from the Northern Calcareous Alps (Austria, Walther, 1885; Fischer, 1964; Kiel et al., 2021), the Julian Alps (Slovenia, Jurkovšek and Kolar-Jurkovšek, 2021), Slovakia (Silická Brezová, Silica Nappe, *Halorella*-bearing fissure-filling Channell et al., 2003), Hungary (Újlaki Hill, Main Dolomite Formation, Végh-Neubrandt, 1982), the Apuseni Mountains (Romania, Lazăr et al., 2020 and the present study) and from a supratidal palaeokarst cavity flooded by marine ingressions (Bakony Mountains, Hungary, Müller et al., 2026).
(b) hydrocarbon seep deposits from Oregon, U.S.A. (Peckmann et al., 2011) and Southern Turkey (Kasımlar Basin in the Taurus Mountains, Kiel et al., 2017);
(c) transitional facies between basin and shallow water carbonate deposits in East Timor Indonesia, Aitutu Group (Benincasa, 2015) and reef limestones in Tadjikistan, Pamir Mountains (Ager, 1968; McClennen et al., 2024).

However, from all *Halorella* occurrences mentioned in the Paleobiology Database (McClennen et al., 2024) and in the literature, only five occurrences are thoroughly documented (through integrated analyses of paleontology, geochemistry and mineralogy). These include mass-occurences of *Halorella* related to hydrocarbon seeps (Oregon and SW Turkey), mass-occurences of *Halorella* from palaeokarst cavites flooded by marine ingressions (Bakony Mountains) and neptunian dikes and sills with no association with hydrocarbon-rich fluids or hydrothermal fluids influence (Northern Calcareous Alps and Apuseni Mountains).

6. Conclusions

This study documents a unique record of an Upper Triassic assemblage comprising brachiopod (*Halorella*) – arthropod (*Halorina* microcoprolites) – microbial (*Frutexites*) elements, found in iron-rich carbonates that fill a neptunian sill developed in Wetterstein-type limestones in the Apuseni Mountains, Romania.

The conodont assemblage extracted from the host limestone indicates an early Carnian age.

Given the generally short stratigraphic range of *Halorella* species and the presence of the benthic foraminifera *Trochosiphonia josephi* identified within the neptunian sill, alongside the *Halorella* assemblage, we infer a late Norian to early Rhaetian age for both the network of neptunian dike and sill and their associated iron-rich carbonate infilling.

A substantial population of the brachiopod *Halorella* inhabited the walls of open fractures such as the neptunian sill. These brachiopods were likely washed into the sill during successive flows of warm marine waters that facilitated the precipitation of iron-rich carbonates.

Considering the broad paleogeographic distribution of the brachiopod *Halorella* during the Late Triassic, coupled with the scarcity of marine paleoenvironments from which this genus has been reported, we suggest that the development of a large population of *Halorella,* along with arthropods and microbial consortia, was likely confined to submarine cryptic paleoenvironments. These cryptic paleoenvironments exhibited peculiar conditions, including warm waters, dark habitats, temporary nutrient richness.

Frutexites microstructures and their possible microbial origin are documented for the first time in Upper Triassic (upper Norian-lower Rhaetian) cryptic cavities.

REE + Y signatures, trace-element distributions, and C-O isotopes indicate predominantly seawater-derived carbonates with minor terrigenous input, modified by Fe-Mn oxide formation, organic matter cycling, and diagenesis.

Variable Y/Ho plus fluctuating Fe–Mn(+V) and Zn contents indicate apparent cyclic shifts over a relatively small-time frame, between oxic and suboxic conditions in a semi-restricted neptunian dike/sill system, possibly driven by episodic biotic blooms and changing water exchange.

At a larger time scale, cyclic isotopic shifts and associated paleotemperature changes are interpreted as tectonically controlled episodes of relative sea-level change and fracturing of only partly lithified carbonates, which created pathways for red carbonate infill and episodic environmental reorganization within the carbonate platform system.

CRediT authorship contribution statement

Iuliana Lazăr: Writing – review & editing, Writing – original draft, Visualization, Validation, Supervision, Resources, Project administration, Methodology, Investigation, Funding acquisition, Formal analysis, Data curation, Conceptualization. **Constantin Balica:** Writing – review & editing, Writing – original draft, Software, Methodology, Investigation, Data curation. **Mihaela Grădinaru:** Writing – review & editing, Writing – original draft, Methodology, Investigation, Formal analysis. **Michael R. Sandy:** Writing – review & editing, Writing – original draft, Methodology, Investigation. **Tea Kolar-Jurkovšek:** Writing – original draft, Methodology, Investigation, Formal analysis. **Eugen Grădinaru:** Methodology, Investigation. **Mihai N. Ducea:** Methodology, Investigation. **Marie-Béatrice Forel:** Methodology, Investigation.

Declaration of competing interest

The manuscript is an original work and has not been submitted for consideration to any other publication. All authors have read the submitted version of the manuscript and approve its submission. All necessary acknowledgments have been made and the work conforms to legal requirements of the country in which it was carried out.

Acknowledgements

This article is dedicated to Professor Eugen Grădinaru (1942-2025), who possessed an intimate and profound knowledge of the geology of the Northern Apuseni Mountains. Several years ago, he encouraged us to explore the Triassic *Halorella* mass-occurrences from this area. Sadly, he could not see these results come to fruition.

We would like to acknowledge the reviewer Marco Balini, the anonymous reviewers and the editor Lucia Angiolini for their corrections, comments and suggestions that greatly improved the original manuscript. Sylvain Rigaud is acknowledged for identification of foraminifera. Hans-Jürgen Gawlick and George Pleş are acknowledged for discussions and for providing literature related to the lithostratigraphy of Wetterstein carbonate platforms. Steffen Kiel and Jörn Peckmann are greatly acknowledged for sharing their REE(Y) data for the *Halorella*-bearing neptunian dikes in the Northern Calcareous Alps by Kiel et al. (2021).

IL acknowledges ICUB (Research Institute of the University of Bucharest) for their partial support of this work within the frame of the projects CPI 835/2024-2025 and 7422/2023. This work also received partial support from the Slovenian Research and Innovation Agency (program P1-0011) for the conodont study conducted by **TKJ**. We thank Marija Petrović and Savo Vuksanović for technical support and Miloš Miler for his assistance in SEM imaging. Communications on conodonts with John Repetski and Yanlong Chen are gratefully acknowledged. **MRS** acknowledges partial support from the Donors of the American Chemical Society Petroleum Research Fund during this project. **MND** acknowledges funding of project #64 by the program PNNR-III-C9-2023-I8 of the Romanian MCID.

Appendix A. Supplementary data

Supplementary data to this article can be found online at https://doi.org/10.1016/j.palaeo.2026.113829.

Data availability

The authors confirm that all data necessary for supporting the scientific findings of this paper have been provided.

References

Aberhan, M., Kiessling, W., Fürsich, F.T., 2006. Testing the role of biological interactions for the evolution in mid-Mesozoic marine benthic ecosystems. Paleobiology 32, 259–277.

Ager, D.V., 1960. Nomenclatural problems in the Mesozoic Rhynchonelloidea. Geol. Mag. 97 (2), 157–162.

Ager, D.V., 1965. The adaptation of Mesozoic brachiopods to different environments. Palaeogeogr. Palaeoclimatol. Palaeoecol. 1, 143–172.

Ager, D.V., 1968. The supposedly ubiquitous Tethyan brachiopod *Halorella* and its relations. J. Palaeontol. Soc. India 5-9, 54–70.

Ager, D.V., Childs, A., Pearson, D.A.B., 1972. The evolution of the Mesozoic Rhynchonellida. Geobios 5, 157–233.

Baltres, A., 1998. Rhaetian carbonate cycles in the Northern Apuseni Mountains (the Vaşcău Plateau). Rev. Roum. Géol. 42, 125–130.

Bathurst, R.G.C., 1991. Pressure-dissolution and limestone bedding: the influence of stratified cementation. In: Einsele, W., Ricken, W., Seilacher, A. (Eds.), Cycles and Events in Stratigraphy. Springer-Verlag, Berlin, pp. 450–463.

Bau, M., 1996. Controls on the fractionation of isovalent trace elements in magmatic and aqueous systems: evidence from Y/Ho, Zr/Hf, and lanthanide tetrad effect. Contrib. Mineral. Petrol. 123, 323–333.

Bau, M., Dulski, P., 1996. Distribution of yttrium and rare-earth elements in the Penge and Kuruman iron-formations, Transvaal Supergroup, South Africa. Precambrian Res. 79, 37–55.

Bau, M., Koschinsky, A., Dulski, P., Hein, J.R., 1996. Comparison of the partitioning behaviours of yttrium, rare earth elements, and titanium between hydrogenetic marine ferromanganese crusts and seawater. Geochim. Cosmochim. Acta 60, 1709–1725.

Bau, M., Moller, P., Dulski, P., 1997. Yttrium and lanthanides in eastern Mediterranean seawater and their fractionation during redox-cycling. Mar. Chem. 56, 123–131.

Baud, A., Richoz, S., 2015. An Early Triassic (Smithian) Sponge – microbial build-up in the Oman Mountains. In: Presentation at the 12th International Symposium on Fossil Cnidaria and Porifera, 5–15.2.2015, Mascat, Oman.

Benincasa, A., 2015. The 'Fatus' of East Timor: Stratigraphy and Structure. PhD thesis. University of Western Australia, pp. 120–122.

Benz, M., Brune, A., Schink, B., 1998. Anaerobic and aerobic oxidation of ferrous iron at neutral pH by chemoheterotrophic nitrate reducing bacteria. Arch. Microbiol. 169, 159–165.

Bitner, M.A., Gerovasileiou, V., 2021. Taxonomic composition and assemblage structure of brachiopods from two submarine caves in the Aegean Sea, Eastern Mediterranean. Eur. Zool. J. 88 (1), 316–327. https://doi.org/10.1080/24750263.2021.1887947.

Bittner, A., 1884. Aus den Salzburger Kalkhochgebirgen. Zur Stellung der Hallstätter Kalke. Verh. K. K. Geol. Reichsanst 6, 99–113.

Bleahu, M., 1976a. Structural position of the Apuseni Mountains in the Alpine system. Rev. Roum. Géol. Géoph. Géog. Géol. 20 (1), 7–19.

Bleahu, M., 1976b. Structure geologique des Apuseni septentrionaux. Rev. Roum. Géol. Géoph. Géog. Géol. 20, 27–39.

Bleahu, M., Patrulius, D., Tomescu, C., Bordea, J., Panin, Şt, Rădan, S., 1970. Date noi asupra depozitelor triasice din Munţii Apuseni. D. S. Inst. Geol. 56 (4), 29–41.

Bleahu, M., Panin, Şt, Tomescu, C., 1972. Contribuţii la biostratigrafia depozitelor triasice din Platoul Vaşcău (Munţii Apuseni). D. S. Inst. Geol. 58 (3), 5–25.

Bleahu, M., Panin, Şt., Tomescu, C., Ştefan, A., Istrate, Gh., Ştefănescu, M., 1979. Geological map of Romania, 1:50000, Vaşcău Sheet, 55d. Inst. Geol. Geof, Bucharest.

Bleahu, M., Lupu, M., Patrulius, D., Bordea, S., Ştefan, A., Panin, Ş., 1981. The structure of the Apuseni Mountains. In: Carpatho-Balkan Geological Association, 12th Congress, Bucharest, Romania. Guidebook Series 23. Published by Inst. Geol. Geophys. Bucharest. Guide to Excursion B3, 106 pp.

Bleahu, M., Mantea, Gh., Bordea, S., Panin, Şt, Ştefănescu, M., Sikic, K., Haas, J., Kovács, S., Péró, Cs, Bérczi-Makk, A., Konrád, Gy, Nagy, E., Rálisch-Felgenhauer, E., Török, Á., 1994. Triassic facies types, evolution and paleogeographic relations of the Tisza Megaunit. Acta Geol. Hung. 37 (3–4), 187–234.

Böhm, F., Brachert, T.C., 1993. Deep-water stromatolites and *Frutexites* Maslov from the Early and Middle Jurassic of S. Germany and Austria. Facies 28, 145–168.

Boulvain, F., De Ridder, C., Mamet, B., Preat, A., Gillan, D., 2001. Iron microbial communities in Belgian Frasnian carbonate mounds. Facies 44, 47–59. https://doi.org/10.1007/BF02668166.

Brand, U., Veizer, J., 1980. Chemical diagenesis of a multicomponent carbonate system. 1. Trace element. J. Sediment. Res. 50, 1219–1236.

Brodie, P.B., 1853. Remarks on the Lias at Fretherne near Newnham, and Purton near Sharpness, with an account of some new foraminifera discovered there; and on certain Pleistocene deposits in the vale of Gloucester. An. Mag. Nat. Hist., London 2 (12), 272–276.

Bronn, H.G., 1832. Die Versteinerungen des Salza-Thales, in Beziehung auf Lill von Lilienbach's Beschreibung dortiger Gebirgs-Formationen. Jb. Miner. Geogn. Geol. Petref. 3, 150–182.

Bucur, I.I., Săsăran, E., 2001. Triassic loferites of Colești Nappe (Vaşcău). In: Bucur, I.I., Filipescu, S., Săsăran, E. (Eds.), Algae and Carbonate Platform in Western Part of Romania. Field Trip Guidebook, 4th Regional Meeting of IFAA, Cluj-Napoca, Romania. Cluj-Napoca University Press, pp. 129–135.

Budurov, K., 1975. Paragonolella foliata sp. n. (Conodonta) von der Trias des Ost-Balkans. Rev. Bull. Geol. Soc. 36, 79–81.

Budurov, K., Stefanov, S.A., 1965. Gattung *Gondolella* aus der Trias Bulgariens. Travaux Sur La Géol. Bulg. Sér. Paléontol. 7, 115–127.

Bush, A.M., Bambach, R.K., Daley, G.M., 2007. Changes in theoretical ecospace utilization in marine fossil assemblages between the mid-Paleozoic and late Cenozoic. Paleobiology 33, 76–97.

Canfield, D.E., Thamdrup, B., Hansen, J.W., 1993. The anaerobic degradation of organic matter in Danish coastal sediments–iron reduction, manganese reduction, and sulfate reduction. Geochim. Cosmochim. Acta 57, 3867–3883.

Cavalazzi, B., Barbieri, R., Ori, G., 2007. Chemosynthetic microbialites in the Devonian carbonate mounds of Hamar Laghdad (Anti-Atlas, Morocco). Sediment. Geol. 200 (1–2), 73–88.

Champenois, F., George, A.D., McNamara, K.J., Shaw, J., Cherdantseva, M., 2024. Contrasting morphology and growth habits of *Frutexites* in Late Devonian reef complexes of the Canning Basin, northwestern Australia. Geobiology 22, e12579. https://doi.org/10.1111/gbi.12579.

Channell, J.E.T., Kozur, H.W., Sievers, T., Mock, R., Aubrecht, R., Sykora, M., 2003. Carnian-Norian biomagnetostratigraphy at Silická Brezová (Slovakia): correlation to other Tethyan sections and to the Newark Basin. Palaeogeogr. Palaeoclimatol. Palaeoecol. 191, 65–109.

Chen, Y.L., Krystyn, L., Orchard, M.J., Lai, X.L., Richoz, S., 2015. A review of the evolution, biostratigraphy, provincialism and diversity of Middle and early Late Triassic conodonts. Pap. Palaeontol. 2, 235–263. https://doi.org/10.1002/spp2.1038.

Cooper, G.A., Muir-Wood, H.M., 1951. Brachiopod homonyms. J. Wash. Acad. Sci. 41 (b), 195–196.

Dagys, A.S., 1963. Verkhnetriasovye Brakhiopody Yuga SSSR [Upper Triassic Brachiopods of the Southern USSR]. Akademiia Nauk SSSR, Sibirskoe Otdelenie, 284 pp.

De Baar, H.J.W., Schijf, J., Byrne, R.H., 1991. Solution chemistry of the rare earth elements in seawater. Eur. J. Solid State Inorg. Chem. 28, 357–373.

Diebel, K., 1956. Conodonten in der Oberkreide von Kamerun. Geologie 4 (5), 424–450.

Dunham, R.J., 1962. Classification of carbonate rocks according to depositional texture. In: Ham, W.E. (Ed.), Classification of Carbonate Rocks, vol. 1. Am. Assoc. Pet. Geol. Memoir, pp. 108–121.

Embry, A.F., Klovan, J.E., 1971. A late Devonian reef tract on northeastern Banks Island, NWT. Can. Petrol. Geol. Bull. 19, 730–781.

Epstein, S., Buchsbaum, R., Lowenstam, H.A., Urey, H.C., 1953. Revised carbonate water isotopic temperature scale. Geol. Soc. Am. Bull. 64, 1315–1326.

Fischer, A.G., 1964. The Lofer Cyclothems of the Alpine Triassic. In: Merriam, D.F. (Ed.), Symposium on Cyclic Sedimentation, vol. 169. Kansas Geol. Surv. Bull, pp. 107–149.

Fisher, J.K., Price, G.D., Hart, M.B., Leng, M.J., 2005. Stable isotope analysis of the Cenomanian-Turonian (Late Cretaceous) oceanic anoxic event in the Crimea. Cretac. Res. 26, 853–863.

Flügel, E., 2010. Microfacies of Carbonate Rocks. Analysis, Interpretation and Application, Second edition. Springer, Berlin-Heidelberg, p. 984.

Flügel, E., Senowbari-Daryan, B., 1996. Evolution of Triassic Reef Biota: state of the art. In: Reitner, J., Neuweiler, F., Gunkel, F. (Eds.), Global and Regional Controls on Biogenic Sedimentation. I. Reef Evolution. Research Reports, vol. 2. Göttinger Arb. Geol. Paläont, pp. 285–294.

Flügel, E., Kiessling, W., Golonka, J., 1996. Phanerozoic Reef patterns: Data Survey, distribution maps and interpretation. In: Reitner, J., Neuweiler, F., Gunkel, F. (Eds.), Global and Regional Controls on Biogenic Sedimentation. I. Reef Evolution. Research Reports, vol. 2. Göttinger Arb. Geol. Paläont, pp. 391–396.

Frank, T.D., Arthur, M.A., Dean, W.E., 1999. Diagenesis of Lower Cretaceous pelagic carbonates, North Atlantic: paleoceanographic signals obscured. J. Foramin. Res. 29, 340–351.

Fürsich, F.T., Oschmann, W., 1993. Shell beds as tools in basin analysis: the Jurassic of Kachchh, western India. J. Geol. Soc. Lond. 150, 169–185.

Gale, A., Dalton, C.A., Langmuir, C.H., Su, Y., Schilling, J.G., 2013. The mean composition of ocean ridge basalts. Geochem. Geophys. Geosyst. 14, 489–518. https://doi.org/10.1029/2012GC004334.

Gawlick, H.-J., 2000. Paleogeographie der Ober-Trias Karbonatplattform in den Nördlichen Kalkalpen. Mitt. Ges. Geol. Bergbaustud. Österr 44, 45–95.

Gawlick, H.-J., Missoni, S., 2021. Demise and aftermath of Triassic shallow-water ramps/platforms in the Western Tethys Realm. In: 35th IAS Meeting of Sedimentology, Guidebook Conference Field Trip FT3. Palacky University Olomouc, Prague.

Gischler, E., 1996. Late Devonian-Early Carboniferous deep-water coral assemblages and sedimentation on a Devonian seamount: Iberg Reef, Harz Mts., Germany. Palaeogeogr. Palaeoclimatol. Palaeoecol. 123, 297–322.

Gischler, E., Sandy, M.R., Peckmann, J., 2003. Ibergirhynchia contraria (F.A. Roemer, 1850), an Early Carboniferous seep-related rhynchonellide brachiopod from the Harz Mountains, Germany-a possible successor to Dzieduszyckia? J. Paleontol. 77, 293–303.

Gonzalez-Donoso, J.M., Linares, D., Martin-Algarra, A., Rebollo, M., Serrano, F., Vera, J. A., 1983. Discontinuidades estratigraficas durante el Cretacico en el Penibetico (Cordillera Betica). Estud. Geol. 39, 71–116.

Grădinaru, M., Lazăr, I., Ducea, M.N., Petrescu, L., 2020. Microaerophilic Fe-oxidizing micro-organisms in Middle Jurassic ferruginous stromatolites and the paleoenvironmental context of their formation (Southern Carpathians, Romania). Geobiology 18, 365–393. https://doi.org/10.1111/gbi.12376.

Guido, A., Rossob, A., Sanfilippo, R., Russoa, F., Mastandrea, A., 2016. Frutexites from microbial/metazoan bioconstructions of recent and Pleistocene marine caves (Sicily, Italy). Palaeogeogr. Palaeoclimatol. Palaeoecol. 453 (1–4), 127–138.

Guido, A., Jimenez, C., Achilleos, K., Rosso, A., Sanfilippo, R., Hadjioannou, L., Petrou, A., Russo, F., Mastandrea, A., 2017. Cryptic serpulid-microbialite bioconstructions in the Kakoskali submarine cave (Cyprus, Eastern Mediterranean). Facies 63, 21. https://doi.org/10.1007/s10347-017-0502-3.

Haas, J., Kovács, S., Krystyn, L., Lein, R., 1995. Significance of Late Permian-Triassic facies zones in terrane reconstructions in the Alpine-North Pannonian domain. Tectonophysics 242, 19–40.

Harper, E.M., Peck, L.S., 2024. The demise of large tropical brachiopods and the Mesozoic marine revolution. R. Soc. Open Sci. 11, 231630. https://doi.org/10.1098/rsos.231630.

Harper, E.M., Wharton, D.S., 2000. Boring predation and Mesozoic articulate brachiopods. Palaeogeogr. Palaeoclimatol. Palaeoecol. 158, 15–24.

Harris, A.G., Lane, H.R., Tailleur, I.L., Ellersieck, I., 1987. Conodont thermal maturation patterns in Paleozoic and Triassic rocks, northern Alaska – Geologic and exploration implications. In: Alaskan North Slope Geology 1. Pacific Sect. Soc. Econ. Paleont. Mineral. Alsko Geol. Soc, pp. 181–191.

Hemming, N.G., Meyers, W.J., Grams, J.C., 1989. Cathodoluminescence in diagenetic calcites: the roles of Fe and Mn as deduced from electron probe and spectrophotometric measurements. J. Sediment. Petrol. 59, 404–411.

Hornung, T., 2005. Palaeoclimate background and stratigraphic evidence of Late Norian Early Rhaetian polyphase synsedimentary tectonics in the Hallstatt Limestones of Berchtesgaden (Rappoltstein, Southern Germany). Austrian J. Earth Sci. 98, 106–119.

Hudson, J.D., 1977. Stable isotopes and limestone lithification. J. Geol. Soc. Lond. 133, 637–660.

Ianovici, V., Borcoş, M., Bleahu, M., Patrulius, D., Lupu, M., Dimitrescu, Savu, H., 1976. Geologia Munţilor Apuseni. Acad, Rom. Bucureşti, pp. 116–146.

Jakubowicz, M., Belka, Z., Berkowski, B., 2014. Frutexites encrustations on rugose corals (Middle Devonian, southern Morocco): complex growth of microbial microstromatolites. Facies 60, 631–650.

Jurkovšek, B., Kolar-Jurkovšek, T., 2021. Fosili Slovenije: Pogled V Preteklost Za Razmislek O Prihodnosti / Fossils of Slovenia: Looking into the Past to Reflect on the Future. Geološki zavod Slovenije, Ljubljana, 264 p., ilustr. (bilingual: Slovene – English).

Kamber, B.S., Webb, G.E., 2001. The geochemistry of late Archaean microbial carbonate: implications for ocean chemistry and continental erosion history. Geochim. Cosmochim. Acta 65 (15), 2509–2525. https://doi.org/10.1016/S0016-7037(01)00613-5.

Kawabe, I., Kitara, Y., Naito, K., 1991. Non-chondritic yttrium/holmium ratio and lanthanide tetrad effect observed in pre-Cenozoic limestones. Geochem. J. 25, 31–44. https://doi.org/10.2343/geochemj.25.31.

Kendall, A.C., 1985. Radiaxial fibrous calcite: a reappraisal. In: Schneidermann, N., Harris, P.M. (Eds.), Carbonate Cements, vol. 36. SEPM Spec. Publ, pp. 59–77.

Kiel, S., Krystyn, L., Demirtaş, F., Koşun, E., Peckmann, J., 2017. Late Triassic mollusk-dominated hydrocarbon-seep deposits from Turkey. Geology 45 (8), 751–754. https://doi.org/10.1130/G39259.1.

Kiel, S., Huemer, J., Gussone, N., Berndt, J., Krystyn, L., Zuschin, M., Peckmann, J., 2021. Brachiopods in early Mesozoic cryptic habitats: Continuous colonization, rapid adaptation, and wide geographic distribution. Palaeogeogr. Palaeoclimatol. Palaeoecol. 583, 110886. https://doi.org/10.1016/j.palaeo.2021.110668.

Kolar-Jurkovšek, T., 1991. Mikrofavna srednjega in zgornjega triasa Slovenije in njen biostratigrafski pomen (Microfauna of Middle and Upper Triassic in Slovenia and its biostratigraphic significance). Geologija 33, 21–170.

Kolar-Jurkovšek, T., Jurkovšek, B., 2019. Konodonti Slovenije / Conodonts of Slovenia. Geološki zavod Slovenije / Geological Survey of Slovenia, Ljubljana, 270 pp.

Kovács, S., 1983. On the evolution of *excelsa*-stock in the Upper Ladinian-Carnian (Conodonta, genus *Gondolella*, Triassic). Österr. Akad. Wiss. Schrift. Erdwiss. Komm. 5, 107–120.

Kovács, S., Arkai, P., 1987. Conodont alteration in metamorphosed limestones from northern Hungary, and its relationship to carbonate texture, illite—crystallinity and vitrinite reflectance. In: Austin, R.L. (Ed.), Conodonts: Investigative Techniques and Applications. Br. Micropalaeontol. Soc. Set, pp. 209–230.

Kovács, S., Arkai, P., 1989. Significance of conodont and limestone-texture alterations in recognition of the boundary between diagenesis and regional dinamothermal metamorphism, based on examples from the Aggtelek-Rudabanya Mts. (NE Hungary). In: M. Al. Foldtani Intezet Evi Jelentese as 1987, pp. 215–235.

Kovács, S., Kozur, H., 1980. Stratigraphische Reichweite der wichtingsten Conodonten (ohne Zahnriehenconodonten) der Mittel-und Obertrias. Geol. Paläont. Mitt. Innsbruck 10 (2), 47–78.

Kovács, S., Sudar, M., Grădinaru, E., Gawlick, H.-J., Karamata, S., Haas, J., Péró, C., Gaetani, M., Mello, J., Polák, M., Aljinović, D., Ogorelec, B., Kolar-Jurkovšek, T., Jurkovšek, B., Buser, S., 2011. Triassic evolution of the tectonostratigraphic units of the circum-pannonian region. Jahrb. Geol. Bundesanst. 151 (3–4), 199–280.

Kozur, H., 1980. Revision der Conodontenzonierung der Mittel- und Obertrias des Tethyalen Faunenreichs. Geol. Paläont. Mitt. Innsbruck 10 (3–4), 79–172.

Kozur, H., 2003. Integrated ammonoid, conodont and radiolarian zonation of the Triassic. Hallesches Jb. Geowiss. B 25, 49–79.

Kozur, H., Mock, R., 1972. Neue conodonten aus der Trias der Slowakei und ihre stratigraphische Bedeutung. Geol. Paläontol. Mitt. Innsbruck 2, 1–20.

Krystyn, L., 1980. Stratigraphy of the Hallstatt region. In: Schoenlaub, H.P. (Ed.), Second European Conodont Symposium ECOS II, vol. 35. Abh. B.-A, pp. 231–258.

Krystyn, L., Mandl, G.W., Schauer, M., 2009. Growth and termination of the Upper Triassic platform margin of the Dachstein area (Northern Calcareous Alps, Austria). Austrian J. Earth Sci. 102, 23–33.

Kutassy, A., 1928. Die Ausbildung der Trias im Momagebirge. Zbl. F. Min. Abt. B Viena 320–325.

Kutassy, A., 1937. Triadische Faunen aus dem Bihar-Gebirge. I. Teil: Gastropoden. Geol. Hun. Ser. Palaeontol. 13, 1–80.

Lazăr, I., Grădinaru, M., Petrescu, L., 2013. Ferruginous microstromatolites related to Middle Jurassic condensed sequences and hardgrounds (Bucegi Mountains, Southern Carpathians, Romania). Facies 59, 359–390.

Lazăr, I., Sandy, M.R., Forel, M.-B., Grădinaru, E., Peckmann, J., Grădinaru, M., 2017. Late Triassic Brachiopod *Halorella* Assemblages from Paleokarst Cavities near Vaşcău, Apuseni Mountains, Romania. In: Eleventh Romanian Symposium on Palaeontology Abstracts Book. Bucharest, pp. 71–72.

Lazăr, I., Schlagintweit, F., Grădinaru, E., 2020. *Halorina cryptica* nov. ichnogen., nov. ichnosp., mass-occurrence of Upper Triassic crustacean microcoprolites from neptunian dikes and sills cutting the Dachstein-type carbonate platform and their paleoenvironmental significance (Northern Apuseni Mountains, Romania). Geobios 61, 31–39. https://doi.org/10.1016/j.geobios.2020.06.003, 0016-6995/c 2020.

Lein, R., 1987. Evolution of the Northern Calcareous Alps during Triassic times. In: Flügel, H.W., Faupl, P. (Eds.), Geodynamics of the Eastern Alps. Franz Deuticke, Vienna, pp. 85–102.

Lein, R., Krystyn, L., Richoz, S., Lieberman, H., 2012. Middle Triassic platform/basin transition along the Alpine passive continental margin facing the Tethys Ocean – the Gamsstein: the rise and fall of a Wetterstein Limestone Platform (Styria, Austria). Field Trip Guide, 29th IAS Meeting of Sedimentology, Schladming, Austria. J. Alpine Geol. 54, 471–498.

Li, M., Wignall, P.B., Dai, X., Hu, M., Song, H., 2021. Phanerozoic variation in dolomite abundance linked to oceanic anoxia. Geology 49, 698–702. https://doi.org/10.1130/G48502.1.

Lohmann, K.C., 1988. Geochemical patterns of meteoric diagenetic systems and their application to studies of paleokarst. In: James, N.P., Choquette, P.W. (Eds.), Paleokarst. Springer-Verlag, Berlin, pp. 50–80.

Lohmann, K.C., Meyers, W.J., 1977. Microdolomite inclusions in cloudy prismatic calcites: a proposed criterion for former high-magnesium calcites. J. Sediment. Petrol. 47, 1078–1088.

Mamet, B., Préat, A., 2006. Iron-bacterial mediation in Phanerozoic red limestones: State of the art. Sediment. Geol. 185 (3–4), 147–157.

Manceñido, M.O., Motchurova-Dekova, N., 2010. A review of crural types, their relationships to shell microstructure, and significance among post-Palaeozoic Rhynchonellida. Spec. Pap. Palaeontol. 84, 203–224.

Manceñido, M.O., Owen, E.F., Savage, N.M., Dagys, A.S., 2002. Dimerelloidea. In: Kaesler, R.L. (Ed.), Treatise on Invertebrate Paleontology, Part H, Brachiopoda Revised, Vol. 4: Rhynchonelliformea (Part). Geol. Soc. Am., Boulder, CO, pp. 1236–1245.

Maslov, V.P., 1960. Stromatolites. Trudy Inst. Geol. Nauk Akad. Nauk SSR 41, 188.

McCammon, H.M., 1969. The food of Articulate Brachiopods. J. Paleontol. 43 (4), 976–985.

McClennen, M., Jenkins, J., Uhen, M., 2024. Paleobiology Database. Version 1.3. Paleobiology Database. Occurrence dataset, 10.15468/jfqhiu. accessed via GBIF.org on 2025-04-04. https://www.gbif.org/occurrence/1698683324.

McLennan, S.M., 1989. Rare Earth elements in sedimentary rocks: influence of provenance and sedimentary processes. In: Lipin, B.R., McKay, G.A. (Eds.), Geochem. Mineral. Rare Earth Elem. De Gruyter, Berlin, pp. 169–200. https://doi.org/10.1515/9781501509032-010.

Mirăuţă, E., Gheorghian, D., 1975. Norian conodonts and foraminifers from North Dobrogea. Dări Seamă Inst. Geol. Geof. 61 (3), 47–76.

Monty, C., 1984. Cavity or fissure dwelling stromatolites (endostromatolites) from Belgian Devonian mud mounds (Extended abstract). Ann. Soc. Geol. Belg. 105, 343–344.

Moore, C.H., 2001. Carbonate Reservoirs: Porosity Evolution and Diagenesis in a Sequence Stratigraphic Framework: Developments in Sedimentology. Elsevier, Amsterdam, p. 460.

Mrdak, M., Wegerer, E., Sudar, M., Djerić, N., Đaković, M., Gawlick, H.-J., 2023. Demise of the Wetterstein Carbonate Platform and onset of the Dachstein Carbonate Platform recorded in deep-water successions of the East Bosnian-Durmitor meaga-unit (Pliješevina, northern Montenegro, Dinarides). Geol. Carpath. 74 (6), 443–458. https://doi.org/10.31577/GeolCarp.2023.26.

Müller, T., Vörös, A., Haas, J., Budai, T., Ullmann, C.V., Price, G.D., Pálfy, J., 2026. Monospecific mass occurrence of the dimerelloid brachiopod *Halorella amphitoma* in a shallow marine environment of the late Triassic Dachstein platform (Bakony Mountains, Hungary). Palaeogeogr. Palaeoclimatol. Palaeoecol. 692, 113793. ISSN 0031-0182. https://doi.org/10.1016/j.palaeo.2026.113793.

Nelson, C.H., Smith, A.M., 1996. Stable oxygen and carbon isotope compositional fields for skeletal and diagenetic components in New Zealand cenozoic nontropical carbonate sediments and limestones: a synthesis and review. N. Z. J. Geol. Geophys. 39, 93–107.

Noble, J.P.A., Logan, A., Webb, G.R., 1976. The recent *Terebratulina* community in the rocky subtidal zone of the Bay of Fundy, Canada. Lethaia 9, 1–17.

Nothdruft, L.D., Webb, G.E., Kamber, B.S., 2004. Rare earth element geochemistry of Late Devonian reefal carbonates, Canning Basin, Western Australia: Confirmation of a seawater REE proxy in ancient limestones. Geochim. Cosmochim. Acta 68 (2), 263–283.

Novack-Gottshall, P.M., 2007. Using a theoretical ecospace to quantify the ecological diversity of Paleozoic and modern marine biotas. Paleobiology 33, 273–294.
Nozaki, Y., Zhang, J., Amakawa, H., 1997. The fractionation between Y and Ho in the marine environment. Earth Planet. Sci. Lett. 148, 329–340.
Orchard, M.J., 2007. New conodonts and zonation, Ladinian-Carnian boundary beds, British Columbia, Canada. In: Lucas, S.G., Spielman, J.A. (Eds.), The Global Triassic, vol. 41. New Mexico Mus. Nat. Hist. Sci. Bull, pp. 321–330.
Orchard, M.J., 2013. Five new genera of conodonts from the Carnian-Norian Boundary beds of Black Bear Ridge, Northeast British Columbia, Canada. In: Lucas, S.G., Spielman, J.A. (Eds.), The Global Triassic, vol. 61. New Mexico Mus. Nat. Hist. Sci. Bull, pp. 445–457.
Otamendi, J.E., Ducea, M.N., Bergantz, G.W., 2012. Geological, petrological and geochemical evidence for progressive construction of an Arc Crustal Section, Sierra de Valle Fertil, Famatinian Arc, Argentina. J. Petrol. 53, 761–800.
Pálfy, J., Kovács, Z., Price, G.D., Vörös, A., Johannson, G.G., 2017. A new occurrence of the early Jurassic brachiopod *Anarhynchia* from the Canadian Cordillera confirms its membership in chemosynthesis-based ecosystems. Can. J. Earth Sci. 54, 1179–1193.
Panin, Șt, Tomescu, C., 1974. Noi contribuţii la biostratigrafia depozitelor triasice din platoul Vaşcău. Dări Seamă Inst. Geol. Geofiz. 60 (4), 51–57.
Panin, Șt, Patrulius, D., Tomescu, C., 1974. Asupra prezenței unor roci jurasice în Platoul Vaşcău (Munții Apuseni). Dări Seamă Inst. Geol. Geof. 60 (5), 55–59.
Panin, Șt, Bleahu, M., Tomescu, C., Mirăuță, El, Ștefănescu, M., 1980. Structure of the Vaşcău Plateau. Dări Seamă Inst. Geol. Geofiz. 67 (5), 109–124.
Paton, C., Hellstrom, J., Paul, B., Woodhead, J., Hergt, J., 2011. Iolite: Freeware for the visualization and processing of mass spectrometric data. J. Anal. At. Spectrom. 26, 2508–2518. https://doi.org/10.1039/c1ja10172b.
Patrulius, D., 1976a. Les formations mésozoïques des Monts Apuseni septentrionaux: corrélation chronostratigraphique et faciale. Rev. Roum. Géol. Géoph. Géog. 20 (1), 49–57.
Patrulius, D., 1976b. Formaţiuni triasice. In: Ianovici, V., Borcoş, M., Bleahu, M., Patrulius, D., Lupu, M., Dimitrescu, R., Savu, H. (Eds.), Geologia Munţilor Apuseni. Acad. Rom., București, pp. 116–146.
Patrulius, D., Bleahu, M., 1967. Le Trias des Monts Apuseni. Geol. Carpath. 18 (2), 233–255.
Patrulius, D., Bleahu, M., Popescu, Il, Bordea, S., 1971. Introduction to the Triassic Geology of Romania. In: Guidebook to Excursions of the 2nd Triassic Colloquium Carpatho-Balkan Association. The Triassic Formations of the Apuseni Mountains and of the East Carpathian Bend. Geol. Inst, Bucharest, pp. 5–54.
Patrulius, D., Bleahu, M., Antonescu, E., Baltreș, A., Bordea, S., Bordea, J., Gheorghian, D., Iordan, M., Mirăuță, El, Panin, Șt, Popa, El, Tomescu, C., 1979. The Triassic Formations of the Bihor Autochthon and Codru nappes system (Apuseni Mountains). In: Third Triassic Colloquium of the Carpatho-Balkan Geological Association, 2-7 October 1979. Inst. Geol. Geoph, Bucharest, 21p.
Pearson, D.A.B., 1967. Rhaetian Articulate Brachiopods of Europe. PhD Thesis. Geology Department, Imperial College of Science and Technology, 368 p.
Peckmann, J., Campbell, K.A., Walliser, O.H., Reitner, J., 2007. A Late Devonian hydrocarbon-seep deposit dominated by dimerelloid brachiopods, Morocco. Palaios 22, 114–122.
Peckmann, J., Kiel, S., Sandy, M.R., Taylor, D., Goedert, J., 2011. Mass occurrences of the brachiopod *Halorella* in Late Triassic methane-seep deposits, eastern Oregon. J. Geol. 119, 207–220.
Peckmann, J., Sandy, M.R., Taylor, D.G., Gier, S., Bach, W., 2013. An Early Jurassic brachiopod-dominated seep deposit enclosed by serpentinite, eastern Oregon, USA. Palaeogeogr. Palaeoclimatol. Palaeoecol. 390, 4–16.
Playford, P.E., Kerans, C., Hurley, N.F., 1984. Neptunian dikes and sills in Devonian reef complexes of the Canning Basin, Western Australia. Am. Assoc. Petrol. Geol. Bull. 68, 517.
Pruss, S., Fraiser, M., Bottjer, D.J., 2004. Proliferation of Early Triassic wrinkle structures: Implications for environmental stress following the end-Permian mass extinction. Geology 32, 461–464. https://doi.org/10.1130/G20354.1.
Pryor, W.A., 1978. Biogenic sedimentation and alteration of argillaceous sediments in shallow water environments. Geol. Soc. Am. Bull. 86, 1244–1254.
Rejebian, V.A., Harris, A.G., Huebner, J.S., 1987. Conodont color and textural alteration: an index to regional metamorphism, contact metamorphism, and hydrothermal alteration. Geol. Soc. Am. Bull. 99, 471–479.
Reolid, M., Molina, J.M., 2010. Serpulid-*Frutexites* assemblage from shadow-cryptic environments in Jurassic marine caves, Betic Cordillera, southern Spain. Palaios 25 (7), 468–474.
Richoz, S., Krystyn, L., 2015. The Upper Triassic events recorded in platform and basin of the Austrian Alps, the Triassic/Jurassic GSSP and Norian/Rhaetian GSSP candidate. In: Richoz, S. (Ed.), Field Trip in the Eastern and Southern Alps (Austria, Italy), STRATI 2015, Graz, Austria, vol. 111. Berichte Geol. Bund, pp. 75–136.
Riding, R., 1991. Classification of microbial carbonates. In: Riding, R. (Ed.), Calcareous Algae and Stromatolites. Springer-Verlag, Berlin, pp. 21–51.
Rigaud, S., Martini, R., Vachard, D., 2015. Early evolution and new classification of the order Robertinida (foraminifera). J. Foraminifer. Res. 45 (1), 3–28.
Rigo, M., Mazza, M., Káradi, V., Nicora, A., 2018. New Upper Triassic Conodont Biozonation of the Tethyan Realm. Chapter 6. In: Tanner, L.H. (Ed.), The Late Triassic World, Topics in Geobiology, vol. 46, pp. 189–235.
Rindsberg, A.K., Kopaska-Merkel, D.C., 2013. Paleoecology and diagenesis of *Parafavreina ziczac* isp. Nov., a crustacean microcoprolite from the Upper Jurassic (Oxfordian) Smackover formation of Alabama. In: Ebersole, J., Ikejiri, T. (Eds.), Contributions to Alabama Paleontology: Tuscaloosa, vol. 31. Alabama Museum of Natural History Bulletin, pp. 74–93.
Rodríguez-Martínez, M., Heim, C., Simon, K., Zilla, T., Reitner, J., 2011. *Tolypammina gregaria* Wendt 1969 — *Frutexites* assemblage and ferromanganese crusts: A coupled nutrient-metal interplay in the Carnian sedimentary condensed record of Hallstatt facies (Austria). In: Reitner, J., Queric, N.V., Arp, G. (Eds.), Advances in Stromatolite Geobiology, Lect. Notes in Earth Sci, vol. 131, pp. 409–434.
Rosenberg, R., Nilsson, H.C., Diaz, R.J., 2001. Response of benthic fauna and changing sediment redox profiles over a hypoxic gradient. Estuar. Coast. Shelf Sci. 53, 343–350. https://doi.org/10.1006/ecss.2001.0810.
Rossel, P., Oliveros, V., Ducea, M.N., Charrier, R., Scaillet, S., Retamala, L., Figueroa, O., 2013. The Early Andean subduction system as an analogue to island arcs: evidence from across-arc geochemical variations in northern Chile. Lithos 179, 211–230.
Săndulescu, M., 1984. Geotectonica României. Ed. Tehnică, București, 336 p.
Sandy, M.R., 1989. Preparation of serial sections. Paleontol. Soc. Spec. Publ. 4, 146–156. https://doi.org/10.1017/s2475262200005086.
Sandy, M.R., 2010. Brachiopods from ancient hydrocarbon seeps and hydrothermal vents. In: Kiel, S. (Ed.), The Vent and Seep Biota, Topics in Geobiology. Springer, Heidelberg, pp. 279–314.
Sars, G.O., 1866. Oversigt af Norges marine ostracoder. Forh. Vidensk. Selsk. Christiania 1865 (1), 1–130.
Scotese, C.R., 2014. Atlas of Permo–Triassic Paleogeographic Maps (Mollweide Projection), Maps 43–52, Volumes 3 & 4 of the PALEOMAP Atlas for ArcGIS. PALEOMAP Project, Evanston, IL. https://doi.org/10.13140/2.1.2609.9209.
Searl, A., 1989. Saddle dolomite: a new view of its nature and origin. Mineral. Mag. 53 (373), 547–555. https://doi.org/10.1180/minmag.1989.053.373.05.
Sharp, Z., 2017. Principles of Stable Isotope Geochemistry, 2nd edition. https://doi.org/10.25844/h9q1-0p82.
Sholkovitz, E.R., Shaw, T.J., Schneider, D.L., 1992. The geochemistry of rare earth elements in the seasonally anoxic water column and porewaters of Chesapeake Bay. Geochim. Cosmochim. Acta 56, 3389–3402.
Sholkovitz, E.R., Landing, W.M., Lewis, B.L., 1994. Ocean particle chemistry: the fractionation of rare earth elements between suspended particles and seawater. Geochim. Cosmochim. Acta 58, 1567–1579.
Siblík, M., 1988. Brachiopoda triadica. Catalogus Fossilium Aust. 2 (a), 1–131.
Siblík, S., Bryda, G., 2005. Brachiopods from the Upper Triassic reef habitats of the Northern Calcareous Alps (Dachstein Limestone, Hochschwab, Austria). Riv. Ital. Paleontol. Stratigr. 11, 413–437.
Siemiradzki, J., 1909. Zbiory l. Zejsznera z kieleckiego dewonu. Sprawozdania Komisji Fizyograficznej 43, 62–94.
Smrzska, D., Zwicker, J., Bach, W., Feng, D., Himmler, T., Chen, D., Peckmann, J., 2019. The behaviour of trace elements in seawater, sedimentary pore water, and their incorporation into carbonate minerals: a review. Facies 65, 41. https://doi.org/10.1007/s10347-019-0581-4.
Steuber, T., Veizer, J., 2002. Phanerozoic record of plate tectonic control of seawater chemistry and carbonate sedimentation. Geology 30, 1123–1126.
Straub, K.L., Benz, M., Schink, B., Widdel, F., 1996. Anaerobic, nitrate dependent microbial oxidation of ferrous iron. Appl. Environ. Microbiol. 62, 1458–1460.
Sudar, M., Kovács, S., 2006. Metamorphosed and ductilely deformed conodonts from Triassic limestones situated beneath ophiolite complexes: Kopaonik Mountain (Serbia) and Bukk Mountains (NE Hungary) – a preliminary comparison. Geol. Carpath. 57 (3), 157–176.
Sulser, H., Furrer, H., 2008. Dimerelloid rhynchonellide brachiopods in the lower Jurassic of the Engadine (Canton Graubünden, National Park, Switzerland). Swiss J. Geosci. 101, 1661–8726.
Taylor, S.R., McLennan, S.M., 1985. The Continental Crust: Its Composition and Evolution. Blackwell Scientific Publication, Oxford, pp. 312–pp.
Tomašových, A., 2008. Substrate exploitation and resistance to biotic disturbance in the brachiopod *Terebratalia transversa* and the bivalve *Pododesmus macrochisma*. Mar. Ecol. Prog. Ser. 363, 157–170. https://doi.org/10.3354/meps07472.
Tomašových, A., García-Ramos, D.A., Nawrot, R., Nebelsick, J.H., Zuschin, M., 2022. How long does a brachiopod shell last on a seafloor? Modern mid-bathyal environments as taphonomic analogues of continental shelves prior to the Mesozoic Marine Revolution. Palaeontology 65, e12631. https://doi.org/10.1111/pala.12631.
Tostevin, R., Shields, G.A., Tarbuck, G.M., He, T., Clarkson, M.O., Wood, R.A., 2016. Effective use of cerium anomalies as a redox proxy in carbonate-dominated marine settings. Chem. Geol. 438, 146–162.
Végh-Neubrandt, E., 1982. Triassische Megalodontaceae. Entwicklung, Stratigraphie und Paläontologie. Akadémiai Kiadó, Budapest. ISBN 963-05-2659-X.
Veizer, J., 1983. Trace elements and isotopes in sedimentary carbonates. In: Reeder, R.J. (Ed.), Carbonates: Mineralogy and Chemistry, Rev. Mineral, vol. 11, pp. 265–299.
Veizer, J., Ala, D., Azmy, K., Bruckschen, P., Buhl, D., Bruhn, F., Carden, G.A.F., Diener, A., Ebneth, S., Godderis, Y., Jasper, T., Korte, C., Pawellek, F., Podlaha, O.G., Strauss, H., 1999. 87Sr/86Sr, δ13C and δ18O evolution of Phanerozoic seawater. Chem. Geol. 161, 59–88.
Walther, J., 1885. Die gesteinsbildenden Kalkalgen des Golfes von Neapel und die Entstehung strukturloser Kalke. Z. Dtsch. Geol. Ges. 37, 329–357.
Wanless, H.R., 1979. Limestone response to stress: pressure solution and dolomitization. J. Sediment. Petrol. 49, 437–462.
Webb, G.E., Kamber, B.S., 2000. Rare earth elements in Holocene reefal microbialites: A new shallow seawater proxy. Geochim. Cosmochim. Acta 64, 1557–1565. https://doi.org/10.1016/j.jembe.2009.01.005.
Weissberger, E.J., Coiro, L.L., Davey, E.W., 2009. Effects of hypoxia on animal burrow construction and consequent effects on sediment redox profiles. J. Exp. Mar. Biol. Ecol. 371, 60–67. https://doi.org/10.1016/j.jembe.2009.01.005.
Wendt, J., 2017. A unique fossil record from neptunian sills: the world's most extreme example of stratigraphic condensation (Jurassic, western Sicily). Acta Geol. Pol. 67, 163–199. https://doi.org/10.1515/agp-2017-0015.

Wiedenmayer, F., 1963. Obere Trias bis mittlerer Lias zwischen Saltrio und Tremona (Lombardische Alpen). Die Wechselbeziehungen zwischen Stratigraphie, Sedimentologie und syngenetischer Tektonik. Eclogae Geol. Helv. 56 (2), 529–640.
Wignall, P.B., Twitchett, R.J., 2002. Extent, duration, and nature of the Permian-Triassic superanoxic event. In: Koeberl, C., MacLeod, K.G. (Eds.), Catastrophic Events and Mass Extinctions: Impacts and Beyond, vol. 356. Geol. Soc. Am. Spec. Pap, pp. 395–413. https://doi.org/10.1130/0-8137-2356-6.395.
Witman, J.D., Cooper, R.A., 1983. Disturbance and contrasting patterns of population structure in the brachiopod *Terebratulina septentrionalis* (Couthouy) from two subtidal habi-tats. J. Exp. Mar. Biol. Ecol. 73, 57–79.
Woods, A.D., Baud, A., 2008. Anachronistic facies from a drowned Lower Triassic carbonate platform: lower member of the Alwa Formation (Ba'id Exotic), Oman Mountains. Sediment. Geol. 209 (1–4), 1–14. https://doi.org/10.1016/j.sedgeo.2008.06.002.
Zawidzka, K., 1972. Stratigraphic position of the Furkaska limestones (Choc nappe, the Tatra Mts). Acta Geol. Pol. 22 (3), 459–466.
Zezina, O.N., 2008. Biogeography of the recent brachiopods. Paleontol. J. 42, 830–858.